Delft University of Technology

MASTER THESIS

Phase Control in 2- and 3-site Kitaev Chains in Quantum Dots

Committee

Dr. Ir. S. Goswami (Supervisor)
Prof. Dr. Ir. L.P. Kouwenhoven
Dr. Ir. M. Veldhorst
S.L.D. ten Haaf (Daily Supervisor)
Ir. I. Kulesh (Daily Supervisor)

A thesis submitted in fulfillment of the requirements for the degree of

Master of Science in Applied Physics

by

V.P.M. Sietses

April 29, 2024

TU Delft Delft University of Technology

Phase Control in 2- and 3-Site Kitaev Chains in Quantum Dots

DELFT UNIVERSITY OF TECHNOLOGY

Vincent P.M. Sietses

Abstract

Kitaev chains have recently been realized in semiconductor quantum dots (QD) coupled to each other through Andreev bound states (ABS) emerging from the superconducting proximity effect. These chains are a promising platform for the detection and manipulation of Majorana bound states, which are predicted to have interesting properties for quantum information experiments such as non-Abelian statistics and robustness to charge noise. In this thesis, we show strong coupling in a relatively long 2-site Kitaev chain in a QD-ABS-QD setup and demonstrate that control over the superconducting phase of the ABS allows tuning of the Kitaev chain regime. We also investigate the Majorana wavefunction overlap in the ABS in the strong coupling regime. We then discuss a 3-site Kitaev chain in the QD-ABS-QD-ABS-QD system, where we demonstrate the importance of superconducting phase control for stable Majorana bound states in this system and directly probe the excitation gap in the bulk of the chain, showing the delocalization of the Majorana bound states. Lastly, we study the Majorana protection against chemical potential fluctuations in the 3-site chain.

Contents

Chapter 1

Introduction

MAJORANA quasiparticles have been a subject of study in condensed matter physics for the past two decades.

These quasiparticles are excitations in condensed matter systems which are defined by being their own anti-particle. The protection that such a particle theoretically enjoys has made it a candidate for quantum information applications, in the form of both gate-based qubits [1, 2] or in a different paradigm altogether, that of topological quantum computation [3, 4]. This approach harnesses the Majorana's intrinsic non-Abelian statistics to perform computations through the interchanging of anyons, known as *braiding* [5], to achieve results different from what would occur using fermions or bosons. Braiding has been predicted to be protected from decoherence [6]. Majorana research has therefore been spurred by the promise of hardware-level quantum error correction.

Beyond the direct applications, the non-Abelian character of Majoranas has also attracted fundamental scientific interest since experimental evidence for non-Abelian anyons is still limited and their statistics remain a mostly theoretical prediction [7, 8]. A direct manipulation of non-Abelian anyons would open up a rich setting to explore more quantum phenomena.

Despite the number of theoretical predictions for the detection of Majorana quasiparticles, direct manipulation of them is still lacking [8]. One of the most impactful theoretical predictions of Majorana modes was from Kitaev in 2000 [9] where he suggested they would emerge in a linear chain with p-wave superconducting pairing. Over the past decade, significant effort was dispensed on building such a system in long proximitized nanowires [10–13]. This approach initially seemed highly successful [14, 15], but is limited by material disorder and the appearance of trivial states that mimic Majorana signatures [16–19]. Kitaev chains defined in quantum dots were proposed as a promising alternative candidate as a platform for Majorana applications [20, 21]. In particular, the degree of control over the chemical potential and inter-quantum dot coupling in the system makes the proposal more robust in the presence of disorder [22].

Very recently at QuTech the required mechanisms for coupling neighboring quantum dots in semiconductor-superconductor hybrids were demonstrated in 1D nanowires [23, 24] and 2D electron gases (2DEGs) [25]. Two years ago, the first minimal Kitaev chain was realized in two quantum dots in a nanowire, which hosted bound states that are predicted to show Majorana properties called Poor Man's Majorana (PMM) excitations [26] in a specific point in parameter space. This was achieved in 2DEGs soon after [27]. Increasing the number of quantum dots has

been predicted to increase the robustness of the Majorana modes [21]. However excitingly even with two quantum dots qubits and non-Abelian statistics are within reach [1].

In this thesis, we will describe the work I was able to contribute to during my time as an MSc student in the Goswami lab. It focused on the impact of the superconducting phase difference in 2-site and 3-site Kitaev chains in quantum dots. The report is structured as follows :

- **chapter 2** describes the necessary theory at the MSc student level.
- **chapter 3** describes the methods for experiments conducted in this thesis.
- **chapter 4** describes how phase control in the 2-site Kitaev chain allows for an additional degree of freedom in the tuning to the Poor Man's Majorana regime. We also explore the overlap of the Majorana wavefunctions between the two quantum dots.
- **chapter 5** describes the first experiments on a phase-controlled 3-site Kitaev chain and shows how phase control allows full control over the Majorana states in the system. We examine how the Majoranas show no overlap in the middle of the chain, and study the Majorana protection.
- **chapter 6** summarizes the main results.
- **chapter 7** briefly demonstrates how machine learning can be used to tune Kitaev chains, providing some outlook for how future experiments could be scaled.

Chapter 2

Theory

THIS chapter presents the necessary theoretical concepts to understand the work presented in the ensuing chapters.

2.1 Majorana Bound states in the Kitaev Chain

Majorana particles, initially predicted by Ettore Majorana almost a century ago as a solution to the Dirac equation [28], are defined by their characteristic of being their own antiparticle. Although Majorana's original consideration was particle physics, where the search for fundamental Majorana particles continues, Majorana quasiparticle excitations have emerged as a fascinating field of study in modern condensed-matter physics [29]. In these systems, Majorana quasiparticles have been predicted to be robust to environmental fluctuations and possess special exchange statistics which make them attractive to study quantum information, especially topological quantum computation [3, 6].

In condensed-matter systems, an electron and a hole are each other's antiparticles. An electron is added to a system by the creation operator $c^\dagger$ and is removed by its Hermitian conjugate, the annihilation operator c. A hole is created by c, and annihilated by $c^\dagger$. We can rewrite these operators in another basis by defining two operators $\gamma_{1,2}$:

$$\gamma_1 = c^\dagger + c, \qquad \gamma_2 = i(c^\dagger - c) \tag{2.1}$$

As it turns out, thus splitting the creation operator into its real and imaginary parts produces two operators which are their own Hermitian conjugates, $\gamma_{1,2} = \gamma_{1,2}^\dagger$. These operators are called the Majorana operators, and since they satisfy fermionic anticommutation rules and are built out of superpositions of an electron and its respective hole, they correspond to a special kind of fermion which has zero energy, zero spin, and zero charge [30]. For this reason, Marorana excitations are often referred to as Majorana Zero Modes (MZMs). There has been considerable theoretical and experimental effort to design systems whose excitations are described by these operators.

In 2000, Kitaev predicted that a chain of N spinless fermions with on-site chemical potentials μ_i, single-fermion hopping with amplitude t_i and p-wave pairing with amplitude Δ_i can be tuned

to a regime with unpaired Majorana modes [9]. The Hamiltonian for such a chain is :

$$H = -\sum_{i=1}^{N} \mu_i c_i^\dagger c_i - \sum_{i=1}^{N-1} t_i c_i^\dagger c_{i+1} + t_i c_{i+1}^\dagger c_i + \sum_{j=1}^{N-1} \Delta_i c_i c_{i+1} + \Delta_i^* c_i^\dagger c_{i+1}^\dagger \tag{2.2}$$

The system described by this Hamiltonian was dubbed the Kitaev chain. Kitaev showed that the Majorana fermions arising in this system were topologically protected in the infinite limit. In this work we are interested in the opposite limit where we work with a small number of sites - specifically two and three. Despite the lack of truly topological protection, this system is still able to host unpaired Majorana fermions. Figure 2.1 illustrates the Hamiltonian for a chain of three fermionic sites. An important distinction is that in the infinite limit Kitaev considered the t and Δ coefficients to be material properties shared between all fermionic sites, i.e. $t_i = t, \Delta_i = \Delta$ for all i. For a small number of sites where we tune the interaction between the sites explicitly in the experimental setup, these coefficients are site-dependent.

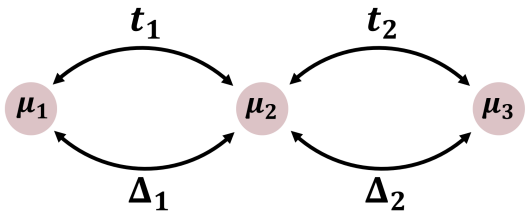

Figure 2.1: Diagram showing three fermionic sites with t and Δ hopping and chemical potentials μ. The circles represent the fermionic sites.

Rewriting the Hamiltonian in terms of the Majorana operators (i.e. performing a basis change according to Equation 2.1) reads [21] :

$$H = \frac{i}{2}\left[-\sum_{i=1}^{N} \mu_i \gamma_{1,i}\gamma_{2,i} + \sum_{i=1}^{N-1} (t_i + \Delta_i)\gamma_{2,i}\gamma_{1,i+1} + (-t_i + \Delta_i)\sum_{i=1}^{N-1} \gamma_{1,i}\gamma_{2,i+1}\right] \tag{2.3}$$

As shown in Kitaev's original work as well as in other derivations [30] [31] [32], this basis change to the Majorana operators highlights two distinct cases: a trivial and a non-trivial regime.

The trivial regime is achieved when $\mu_i < 0$ and $t = \Delta = 0$, shown in Figure 2.2 after the basis change into the Majorana basis. Each Majorana operator is coupled to another on the same fermionic site. Whenever two Majoranas couple together - often called Majorana fusion - they lose the zero-energy property. The fermionic excitations of this system are simply an addition of a fermion to one of the sites, which will have finite energy.

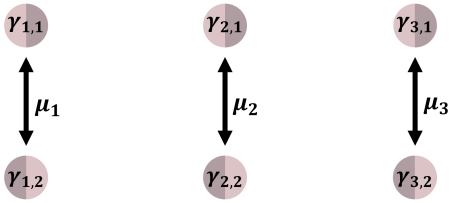

Figure 2.2: Diagram showing the fermionic chain in the Majorana basis in the trivial regime. Each circle represents a Majorana operator.

The Kitaev chain's non-trivial regime is found at $\mu_i = 0$ and $|t_i| = |\Delta_i|$, with $t_i, \Delta_i \in \mathbb{R}$ and $\text{sign}(t_i\Delta_i) = \text{sign}(t_{i+1}\Delta_{i+1})$. In this case Majorana operators couple to those on neighboring sites to fuse into nonlocal fermions as in Figure 2.3.

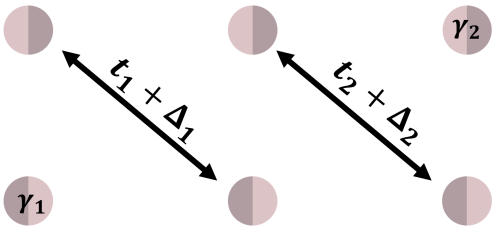

Figure 2.3: Two unpaired Majorana bound states γ_1 and γ_2 in the non-trivial regime.

The chain has two degenerate ground states in this regime, one with even fermionic parity $|g_e\rangle$ and one with odd fermionic parity $|g_o\rangle$. Single-particle excitations between these ground states are given by the Majorana operators :

$$|g_e\rangle = \gamma_i|g_o\rangle, \qquad |g_o\rangle = \gamma_i|g_e\rangle, \qquad i \in \{1, 2\} \tag{2.4}$$

Therefore in this regime, zero energy Majorana excitations are possible. All other excitations have an energy of at least $2t$ - this difference between the zero energy and the first excited state is called the *excitation gap*.

The presence of these MZMs is not some artifact of a highly tuned Hamiltonian. Due to their chargeless nature, they enjoy robustness against fluctuations in μ. In the thermodynamic limit with the number of fermionic sites very large, Majorana excitations are present while $\mu < 2t$ - and indeed regardless of any small local deviations in the inter-site couplings [30]. This limit is often also called the topological limit. However, even outside of this limit, the Majorana excitations present in the non-trivial regime of the Kitaev chain enjoy protection from fluctuations which is even measurable with just two sites [20]. Furthermore, the Majorana overlap is exponentially suppressed, meaning that as few as five or even three sites can host very robust Majorana bound states [21]. In the following sections, we will detail the ingredients necessary to observe Kitaev chain physics.

2.2 Quantum Dots

Quantum dots (QDs) are the building blocks of the physics we explore in this report, where we use them as the fermionic sites in the Kitaev chain. We will give a brief overview of the relevant fundamentals of these structures.

QDs are semiconductor[1] nanostructures which trap electrons inside a potential such that the density of states in the structure is discretized. The name dot comes from the effective 0D nature of this structure, i.e. the quantization of the electron wavefunction in all three spatial dimensions [33]. Quantum dots have also been called artificial atoms, as their discrete energy structure is reminiscent of natural atoms - albeit at a different energy scale and dimensionality [34]. They allow for the observation of uniquely quantum effects of single particles, such as the spin of an electron [35]. They are therefore a promising platform to study electron spins and interactions, in particular when coupled to other nanostructures such as superconductors [30].

The quantum dots studied in this thesis are defined in 2-dimensional electron gases (2DEGs). These are materials formed in semiconductor heterostructures from materials with different Fermi energies and band gaps, allowing for 2D confinement of electrons at their interface [33]. Unlike in nanowires or other quasi-1D materials, this platform does require extra confinement and tuning to form 1D channels. This difficulty is compensated for by the flexibility offered by two dimensions. For example, it allows the possibility of tunneling into a quantum dot from different directions - the use of this will become clear in the results chapters.

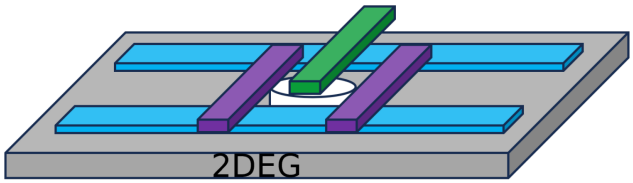

Figure 2.4: An illustration of a quantum dot defined in a 2DEG. The depletion gates (*blue*), tunnel gates (*purple*), and plunger gate (*green*) are colored. Image taken from [36].

The quantum dots we worked with are defined in a 2DEG through voltage gates. These gates surround a region and deplete the 2DEG underneath them, causing a potential minimum in the center of the region that defines the QD. In our systems specifically, we use large depletion gates to form 1D channels and then define the quantum dots by narrower gates that cross this channel. These smaller gates are often called *tunnel gates*, as they not only define the quantum dot but also control the tunneling rates of charged particles trying to enter or exit the confined region.

The fundamentals of QDs have been known for some time [37] and in particular quantum dots in the context of Kitaev chains have been discussed extensively with detailed descriptions at the MSc student level [30–32, 36, 38, 39]. We therefore only summarize the key ingredients here.

[1] Voltage-confined quantum dots cannot exist in metals or superconductors since they expel electric fields.

A quantum dot has two defining energy scales: the level spacing δ_N and the charging energy U.

The charging energy is defined as $U = \frac{e^2}{C}$ where C is the QD's capacitance, which is defined by its exact size and geometry, and e is the elementary charge.[2] U corresponds to the energy required to overcome Coulomb repulsion and add one more electron to the confined region.

The level spacing comes from the discrete nature of the QD's density of states. According to the Pauli exclusion principle, a quantum state can only be occupied by one fermion at a time. Hence when adding an electron an additional energy cost $\delta_N = \xi_N - \xi_{N-1}$ must be paid, where $\{\xi_N\}_N$ are the energies of the quantum dot levels. These energies are determined by the microscopics of the confinement in the quantum dot as well as for example angular momentum or Zeeman splitting [34].

The chemical potential $\mu(N)$ of the N-th QD orbital is the energy cost of adding one more electron when there are already $N-1$ electrons confined in the quantum dot. To control the occupation of the quantum dot we would like the freedom to manipulate $\mu(N)$, which is done by using a plunger gate (shown in green in Figure 2.4) whose only function is to regulate the energy of the electrons in the QD. It turns out that under the constant interaction model where U is independent of N the chemical potential is then [37]:

$$\mu(N) = \left(N - \frac{1}{2}\right) U - e\alpha V_g + \delta_N \tag{2.5}$$

where V_g is the plunger gate voltage and α is the *lever arm*, a number between 0 and 1 characterizing how strongly the quantum dot is coupled to the plunger gate[3]. Increasing the gate voltage means decreasing $\mu(N)$, and when $\mu(N) = 0$ the state with N electrons and with $N-1$ electrons have the same energy. This is called the charge degeneracy point [30], and increasing the gate voltage further causes a change in charge ground state to an occupation of N electrons.

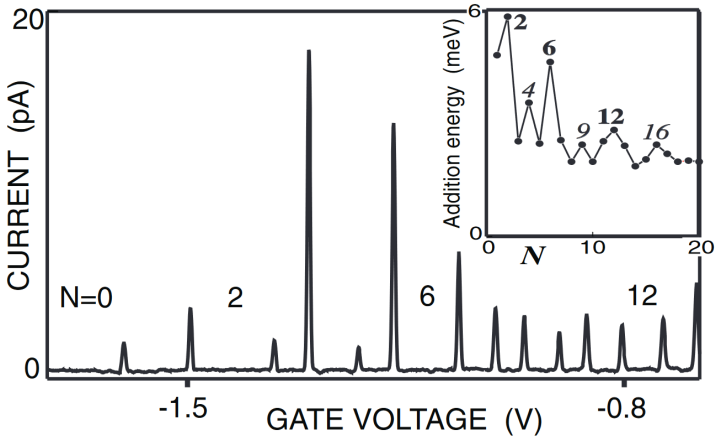

Figure 2.5: Current through a QD as a response to the gate voltage. The inset shows the addition energy $E_{add}(N) = \mu(N) - \mu(N-1) = U + \delta_N$. Figure taken from [34].

[2] In some parts of the literature $U = \frac{e^2}{2C}$ is the preferred convention. The charging energy is also often labeled as E_C.

[3] The exact expression to get the lever arm for a quantum dot is $\alpha = C_G/(C_G + C_D + C_S)$, where C_D and C_S are the capacitances of the source and drain to the QD and C_G is the capacitance of the gate to the QD [37].

Figure 2.5 illustrates how the gate voltage allows control over the chemical potential in a quantum dot. The peaks in current, colloquially often named Coulomb peaks, correspond to transitions in electron occupation. For current to be measured, two metallic leads (a source lead that provides electrons and a drain lead that accepts them) need to be coupled to the quantum dot. Electron transport then occurs through a QD level only if the chemical potential difference between the leads, called the bias window $V_{bias} = (\mu_S - \mu_D)/e$, is larger than the chemical potential of that level as shown in Figure 2.6.

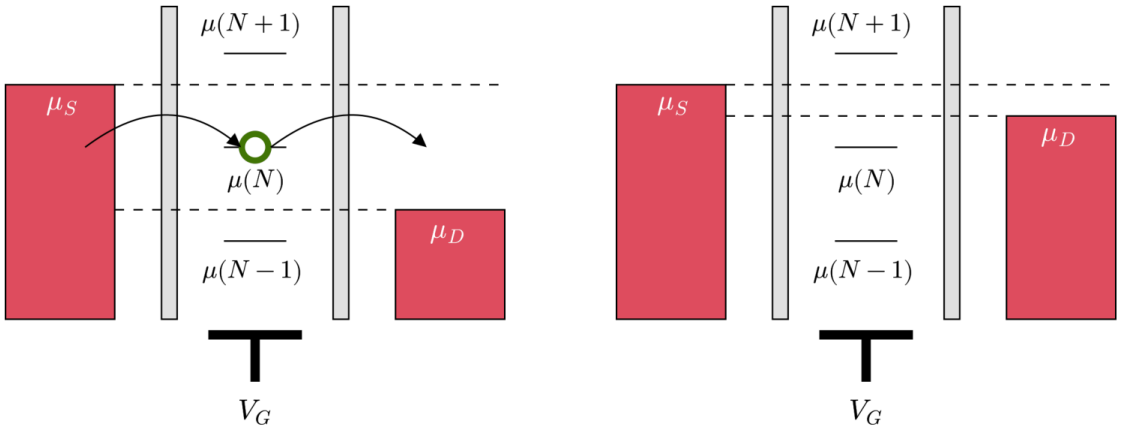

Figure 2.6: Left. Resonant transport occuring when $|eV_{bias}| > \mu(N)$. **Right.** Coulomb blockade, when $|eV_{bias}| < \mu(N)$. Figure adapted from [31].

If there is no QD level in the bias window resonant transport cannot occur and the QD is in *Coulomb Blockade*, where - disregarding higher-order processes - the resistance in the dot is effectively infinite. We use this often throughout the experiments detailed in this report, to effectively remove one or several QDs from the system and study a smaller part of the system.

In this thesis, after a quantum dot is defined and tuned we continue to work with only a single quantum dot level.[4] Furthermore, since $U + \delta_N$ is much larger than any of the other energy scales in the system, we disregard the other levels giving an effective Hamiltonian of :

$$H_{QD} = \mu(\hat{n}_\uparrow + \hat{n}_\downarrow) + E_Z(\hat{n}_\uparrow - \hat{n}_\downarrow) + U\hat{n}_\uparrow\hat{n}_\downarrow \tag{2.6}$$

where $\hat{n}_\uparrow, \hat{n}_\downarrow$ are the number operators for the spin up and spin down occupation numbers and E_Z is the Zeeman energy $E_Z = \frac{1}{2}\mu_B g B$. Applying a magnetic field splits the $|\uparrow\rangle$ and $|\downarrow\rangle$ levels in energy, and in the high field limit $E_Z \to \infty$ the effective Hamiltonian becomes spinless :

$$H_{QD} = \mu\hat{n} \tag{2.7}$$

Therefore a spin-polarized quantum dot level may be used as a fermionic site to engineer more complicated Hamiltonians. In this thesis in particular they will be combined with the rich physics of superconductors to form Kitaev chains.

[4] Quantum dot levels are sometimes also referred to as quantum dot orbitals, due to the description of QDs as artificial atoms.

2.3 Superconductivity and Andreev Bound States

Superconductivity was discovered in 1911 and since then has not stopped being an active field of research. In a superconductor that is well described by the Bardeen-Cooper-Schrieffer theory, electron-phonon interactions cause an effective attraction between electrons [40]. This leads to a quantum phase transition where electrons close to the Fermi energy condense into Cooper pairs - two bound electrons with opposite spin and momentum. This condensate is characterized by an energy scale Δ which depends on the strength of the attractive interaction[5]. Single fermion excitations with energy less than Δ are not allowed, leading to this energy being known as the superconducting *gap*. Furthermore, the fermionic excitations of a superconductor are no longer charge eigenstates such as a hole or an electron in a metal or semiconductor, but coherent superpositions of a particle and hole: $\gamma^\dagger = uc^\dagger + vc$. Such an excitation is called a Bogoliubov quasiparticle, and its charge $|u|^2 - |v|^2$ is often called its BCS charge [41].

Whenever a superconductor is brought into contact with a normal metal or a semiconductor, the normal system acquires some superconducting properties - this has been coined the *proximity effect* [42] [43]. Microscopically, the BCS wavefunction leaks into the normal section through the process of *Andreev reflection* (AR) and induces superconducting correlations close to the interface with the superconductor [41].

In the devices used in this thesis, this proximity effect is so strong that the semiconductor shows a hard induced superconducting gap [44]. What this means is that the proximitized semiconductor allows no excitation with energy smaller than Δ_{ind}. This parameter is called the induced gap and depends on the coupling to the neighboring superconductor and its gap Δ. The engineering of hard superconducting gaps with large Δ_{ind} in semiconductors is of critical importance to measure the physics discussed in this report, and is one of the main challenges in the implementation of Kitaev chain physics in other materials [13].

Andreev discovered in 1964 that an electron in a normal metal can reflect on the interface of a superconductor as a hole with opposite spin and momentum, by creating a Cooper pair at the Fermi-energy in the superconductor [45].

Figure 2.7: Left. An illustration of Andreev reflection at a normal-superconductor (N-S) interface. The charge, velocity and energy of the electron and hole are labeled. **Right.** Schematic for an Andreev bound state through repeated AR in an S-N-S junction. The superconductors have a phase difference $\phi = \theta_L - \theta_R$ Drawings adapted from [41]

When AR occurs at two separate interfaces, a bound state can exist between those interfaces in the limit of infinite reflections. This process, which is sketched on the right in Figure 2.7, results in a so-called *Andreev Bound state* (ABS) and can be seen as the superconducting equivalent of a particle in a box problem from introductory quantum mechanics [46]. The bound

[5]This Δ is not to be confused with the Δ in the Kitaev chain model.

state's energy depends on the phase difference and the distance between the superconductors. Moreover, its energy and excitations can depend on the details of the disorder in the normal region, the transparencies of the interfaces, as well as other considerations [47]. The study of Andreev Bound states in S-N-S junctions (also called Josephson junctions) has led to exciting applications such as Andreev spin qubits [46].

At its simplest in the short-junction limit, an ABS can be considered as a superposition of an electron and a hole (a Bogoliubov quasiparticle!) that lives in between two interfaces where AR occurs. This state can then be excited to a spin doublet state with odd fermionic parity. If the ABS energy is much smaller than the superconducting gap it can be considered a purely two-level system (with 4 basis states due to the spin degree of freedom) [47].

Additionally, when an Andreev bound state is found in a region with confinement due to voltage barriers it can behave similarly to a quantum dot - i.e. with significant level spacing. However, unlike a quantum dot, it has negligible charging energy since it is screened by the superconductor. Furthermore, this type of ABS often has energy within the superconducting gap even for a phase difference of $\phi = 0$ [46].

In this thesis, we will therefore discuss Andreev Bound states as this two-level system, deriving from an alternative model in which we consider a quantum dot that is very strongly coupled to a superconductor. It has been shown that it is equivalent to solving a superconducting version of the Anderson impurity model within some limits[6] [30, 31]. The Hamiltonian for such an ABS in the many-particle basis $\{|0\rangle, |\uparrow\downarrow\rangle, |\uparrow\rangle, |\downarrow\rangle\}$ reads :

$$H_{ABS} = \begin{pmatrix} 0 & -\Gamma_s & 0 & 0 \\ -\Gamma_s & 2\epsilon_0 + U & 0 & 0 \\ 0 & 0 & \epsilon_0 + E_Z & 0 \\ 0 & 0 & 0 & \epsilon_0 - E_Z \end{pmatrix} \tag{2.8}$$

Here ϵ_0 represents the chemical potential (which is gate-controllable) and E_Z is the Zeeman energy. You may notice that this Hamiltonian is the same as for a single quantum dot level, except for the Γ_s term, the superconducting pairing induced by the parent superconductor. It plays the same role as Δ does in a superconductor.

Note that H_{ABS} is block diagonal. The two blocks correspond to the manifold with even parity and the manifold with odd parity. The odd states $|\uparrow\rangle$ and $|\downarrow\rangle$ do not interact, however the even states do through Γ_s and hybridize into two new states :

$$|S_-\rangle = u|0\rangle - v^*|\uparrow\downarrow\rangle, \qquad |S_+\rangle = v|0\rangle + u|\uparrow\downarrow\rangle \tag{2.9}$$

Where $|S_-\rangle$ is the ground state of the even manifold. We call these states singlet states, as they remain spinless. This state competes energetically with the doublet state $|\downarrow\rangle$, the ground state of the odd manifold, to be the system ground state. Figure 2.8 shows which is the ground state depending on the superconducting coupling Γ_s and the chemical potential ϵ_0. The quantum dot model presented in section 2.2 corresponds to the x-axis, where $\Gamma_s = 0$.

[6] These limits are known as the atomic limit and the zero-bandwidth approximation. They do not change the qualitative behavior of the system but do simplify the intuition significantly. They are described in detail in [30].

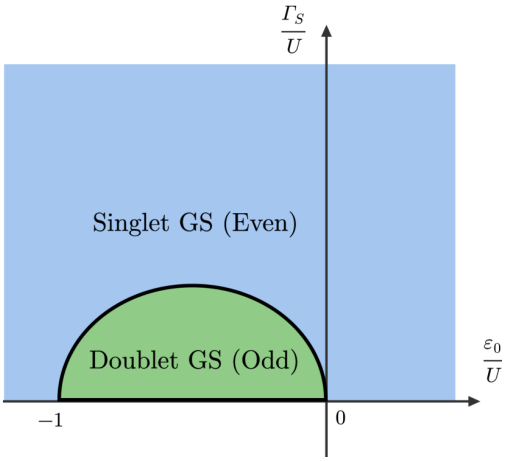

Figure 2.8: Phase diagram of a quantum dot with even state pairing. The boundary between the odd and even manifolds indicates a singlet-doublet phase transition. Figure adapted from [31].

In the limit of negligible charging energy $U \ll \Gamma_s$, which is often called the Andreev bound state limit and made possible through charge screening by the superconductor, we find that the system never experiences a phase transition and that the singlet state smoothly varies from $|S_-\rangle = |0\rangle$ at very positive ϵ_0 to $|S_-\rangle = |\uparrow\downarrow\rangle$ for very negative ϵ_0.

In this limit, the charge character of $|S_-\rangle = u|0\rangle - v|\uparrow\downarrow\rangle$ depends on the chemical potential as :

$$|v|^2 = 1 - |u|^2 = \frac{1}{2} - \frac{\epsilon_0}{2\sqrt{\epsilon_0^2 + \Gamma_2}} \tag{2.10}$$

Below we plot these u, v factors against $-\epsilon_0$ (labeled $-\mu_{ABS}$ in the plot). We choose this quantity for the x-axis instead of ϵ_0 because this quantity is proportional to gate voltage: $\delta V = -\frac{\delta\epsilon_0}{\alpha}$.

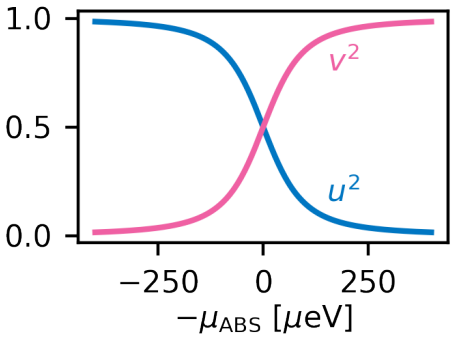

Figure 2.9: Charge of $|S_-\rangle$ as a response to chemical potential $-\mu_{ABS}$ in the $U \ll \Gamma_s$ limit. Plotted for $\Gamma_s = 100$ µeV.

The energy of the singlet state, as a function of the chemical potential, is

$$E_{S_-} = \langle S_-|H_{ABS}|S_-\rangle = \epsilon_0 - \sqrt{\epsilon_0^2 + \Gamma_s^2} \tag{2.11}$$

The energy of the doublet ground state is simpler, $E_\downarrow = \epsilon_0 - E_Z$. In the zero-field limit, we simply have $E_\downarrow = \epsilon_0$. The difference between those states gives the first excitation energy :

$$E_{ex} = E_\downarrow - E_{S-} = \sqrt{\epsilon_0^2 + \Gamma_s^2} \tag{2.12}$$

Since this is the energy that is required to excite the ABS with a hole or electron, it is this energy that we can probe directly in quantum transport measurements. When an electron with energy E_{ex} or hole with energy $-E_{ex}$ enters into the system, it can excite the ABS from the singlet to the doublet. Crucially, the ABS can then relax by again absorbing an electron or hole again with energy $\pm E_{ex}$.[7] A Cooper pair is then formed in the superconductor, and the ABS returns to the singlet ground state - this two-step process is called resonant Andreev tunneling [30]. For this reason, $E_{ex} = E_{ABS}$ is the energy that we refer to when discussing the energy of the ABS. We note that Γ_s is the minimum ABS excitation energy, although in the presence of charging energy this excitation energy can be lowered. Furthermore, at finite E_Z two excitation energies can be measured: $E_{ex} = \sqrt{\epsilon_0^2 + \Gamma_s^2} \pm E_Z$.

We have discussed how we may control the charge of the Andreev bound state by tuning the chemical potential, and what energy we expect to measure in quantum transport measurements. We conclude this chapter by noting a few key points.

In this chapter, we have described Andreev Bound states in a Josephson junction which arises from infinite AR and as a limit of a strongly proximitized quantum dot. Despite being derived from different models, they can both show the same behavior in that they exhibit singlet-doublet transitions and have a singlet ground state at all values of parameter space.

In the Josephson junction, the phase difference plays a key role in the physics. In the proximitized QD, there is no phase difference to speak of; and yet by coupling the QD to two different superconductors in this model, we can observe the same physics. This control over an ABS and its impact on Kitaev chain physics has been theoretically explored in recent work [48] and observing this experimentally is the main focus of chapter 4.

Lastly, when both the superconducting pairing Γ_s and the charging energy U are non-negligible in a quantum dot, the QD behaves as a Yu-Shiba-Rusinov (YSR) state which is also known as the strongly-coupled regime [49]. Such a state shows strong hybridization between the singlet states but still has a singlet-doublet transition when varying the chemical potential. Using these states instead of the standard QD levels without proximitization allowed for stronger, more robust Kitaev chain physics [50].

2.4 Elastic Cotunneling and Crossed Andreev Reflection

Superconductivity is a necessary ingredient to have Majorana quasiparticles in any system [9]. In the Kitaev chain model, the t-term can result from simple direct hopping, as occurs in quantum

[7] This symmetry between injecting a hole and an electron is an example of particle-hole symmetry, which is a general property of BCS superconductors [33].

dots coupled through a tunnel barrier. Superconductivity is required to get the Δ term - this is why we bothered to introduce superconductivity in the first place.

Initial propositions for coupling two quantum dots relied on using the quasiparticle continuum of a superconductor - i.e. the excitations above Δ. However, this approach lacked both tunability and sufficient coupling strength to be used in useful devices [51]. Sub-gap excitations in the form of Andreev bound states overcome these problems. The tuning of these states allowed for a new generation of highly efficient Cooper pair splitters [24] [25], and then the first QD-based Kitaev chains.

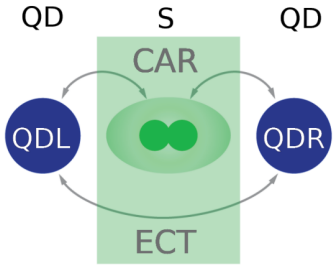

Figure 2.10: Diagram showing two quantum dots coupled through a superconductor, allowing Crossed Andreev Reflection (CAR) and Elastic Cotunneling (ECT); adapted from [27].

Two processes compete in transport in the QD-ABS-QD system when resonant Andreev tunneling is not allowed. The first is crossed Andreev reflection (CAR) [8], where an electron enters from one QD and a hole exits into the other QD, forming a Cooper pair in the superconductor - this corresponds to $c_L^\dagger c_R^\dagger + h.c.$. The second process is elastic cotunneling (ECT) where an electron enters through one QD, tunnels through the superconducting region and exits through the other QD, corresponding to $c_L^\dagger c_R + h.c.$. Both of these processes are mediated through a second-order process by the ABS, detailed in Refs. [32] and [51].

The exact rates of ECT and CAR depend on the charge character and energy of the ABS. In the simplest model, where a single ABS couples the QDs at zero-field with the QDs at $\mu_L = \mu_R = 0$, the rates are computed through Fermi's Golden Rule by taking into account the intermediate virtual states [32]. They are :

$$W_{ECT} = \frac{2\pi}{\hbar}\left|\frac{u^2 - v^2}{E_{ABS}}\right|^2, \qquad W_{CAR} = \frac{2\pi}{\hbar}\left|\frac{2uv}{E_{ABS}}\right|^2 \tag{2.13}$$

These rates correspond to, in the context of the Kitaev chain as in Equation 2.2, the values of t and Δ respectively. In the simple model as discussed in section 2.3, the excitation energy of the Andreev bound state is $E_{ABS} = \sqrt{\epsilon_0^2 + \Gamma_S^2}$. In realistic systems this may be lowered by charging or Zeeman effects. While this may increase interaction, if the ABS energy is too low resonant Andreev tunneling will start to occur, which dominates over CAR and ECT processes [30]. In other words, if the ABS comes down too low in energy it is no longer a virtual coupler but an active participant in the transport through the system, meaning that the Kitaev chain Hamiltonian is no longer a valid effective model.

[8] CAR is sometimes called nonlocal Andreev reflection, in contrast to the usual Andreev reflection which is local.

Besides the need to ensure the ABS stays at high enough energy, another difficulty arises : the Kitaev chain requires spin polarization in the quantum dots. This presents a challenge; ECT conserves spin since it is effectively the same electron hopping from one dot to the other, CAR is a spin-flipping process because to form a Cooper pair the electrons entering the superconductor need to have opposite spin. This implies that at finite field CAR and ECT cannot coexist! This is indeed a problem if we require $t = \Delta \neq 0$ to find our Majorana sweet spot.

This issue is solved by the presence of spin-orbit (SO) in our system. Spin-orbit is a relativistic effect where an electron moving in an electric field experiences it as a magnetic field in its rest frame. This field interacts with its magnetic moment, which is characterized by the following Hamiltonian [32] :

$$H = \frac{-g\mu_B}{2c^2}(\vec{v} \times \vec{E}) \cdot \vec{\sigma} \tag{2.14}$$

Where μ_B is the Bohr magneton, σ, g and v are the electron's spin, Landé g-factor and velocity respectively, and $\vec{E}$ is the experienced electric field. Asymmetries in the lattice structure can lead to additional SO effects. The semiconductor which we work with in this report shows Rashba spin-orbit coupling [30] :

$$H_R = \alpha_R \vec{\sigma} \cdot (\vec{k} \times \vec{E}) \tag{2.15}$$

Where $\vec{k}$ is the electron's momentum and α_R is the Rashba parameter characterizing the strength of this coupling. This type of SO-coupling allows spin-precessing processes, as the spin of an electron with momentum $\vec{k}$ will precess around $\vec{B}_{SO} = \vec{k} \times \vec{E}$ [31]. Hence when tunneling occurs between the ABS and a QD a component of the wavefunction flips its spin. This allows CAR between two QD orbitals with the same spin polarization, or ECT between opposite spin orbitals. By adjusting the direction of the external spin polarizing field, we can tune how much spin precession occurs. When the external field is parallel to $\vec{B}_{SO}$ no spin precession occurs and CAR and ECT do not coexist. In contrast, the amount of spin-flipping is maximum when the external field is perpendicular to $\vec{B}_{SO}$ [23]. An in-depth theoretical description may be found in Ref. [51].

It is possible to isolate these processes and measure their strengths individually. However, once we have a working Kitaev chain we want to tune to the sweet spot where both processes are present. To do this we need to be able to take two neighbouring spin-polarized QDs and read out the relative strengths of t and Δ with both QDs at zero chemical potential.

The Hamiltonian for a 2-site Kitaev chain in the many-body basis $\{|00\rangle, |11\rangle, |10\rangle, |01\rangle\}$ is [20]:

$$H = \begin{pmatrix} 0 & \Delta & 0 & 0 \\ \Delta & \mu_L + \mu_R & 0 & 0 \\ 0 & 0 & \mu_R & t \\ 0 & 0 & t & \mu_L \end{pmatrix} \tag{2.16}$$

This matrix is block diagonal, with the two blocks corresponding to manifolds of different parities. When we fulfill part of the sweet spot condition $\mu_L = \mu_R = 0$, the lowest energy state of the even manifold is :

$$|g_e\rangle = \frac{1}{\sqrt{2}}\left(|00\rangle - |11\rangle\right), \qquad E_e = -\Delta \tag{2.17}$$

And for the odd manifold:

$$|g_o\rangle = \frac{1}{\sqrt{2}}\left(|01\rangle - |01\rangle\right), \qquad E_e = -t \tag{2.18}$$

We see that whether the ground state belongs to the even or odd parity manifold depends solely on the relative magnitude of t and Δ. If $t > \Delta$ the ground state will have odd parity while if $\Delta > t$ the ground state has even parity. If the ground state is a degeneracy between the even and odd parities, then $t = \Delta$ and we have tuned to the Majorana sweet spot where PMM excitations appear.

The relative strengths of these interactions are readily accessed in slow transport measurements. Conductance at zero bias is measured when degeneracies exist between odd and even states. Sweeping the chemical potentials (which we do through plunger gates) of the left and right QDs against each other shows where those degeneracies exist. Such a measurement is called a *charge stability diagram* (CSD) - as it shows where the charges in the system are stable.

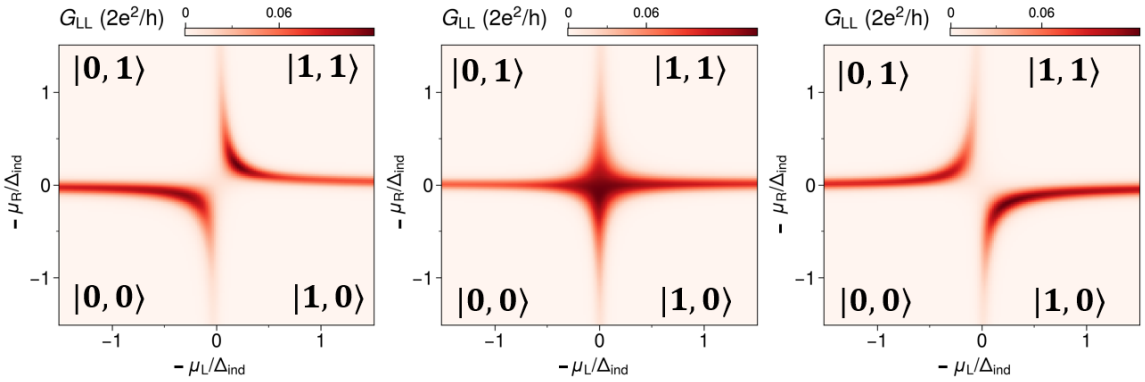

Figure 2.11: Simulated charge stability diagrams in three different regimes. The labeled states indicate what the ground states would be in their respective quadrants without any hybridization.

In Figure 2.11 we show simulated CSDs. On the left, we have the ECT-dominated regime where $t > \Delta$. The anticrossing indicates that no even-odd degeneracy is crossed as we move from the $|01\rangle$ to the $|10\rangle$ state, implying that the ground state at $\mu_L = \mu_L = 0$ has odd parity. Similarly, the right plot shows an anticrossing the other way which heralds a CAR-dominated regime where $\Delta > t$. The central plot shows the expected measurement at the Majorana sweet spot, where $t = \Delta$. This method of tuning to the Majorana sweet spot was recently demonstrated in the first 2-site Kitaev chain [26] and was also used to measure PMMs in 2DEGs [27].

This method also works for Kitaev chains based on YSR states as described in section 2.3, although the nature of the coupling processes is slightly changed due to the eigenstates in the QD no longer being charge eigenstates [50]. Throughout this report, we refer to spin-conserving tunneling as ECT and spin-flipping tunneling as CAR. Similar to how it was experimentally justified in Ref. [50] and theoretically explained in Ref. [49], although these processes are defined through charge states and the dots in this work have no well-defined charge due to being in the strong coupling regime, the large charging energy in the dots means that spin conserving

tunneling is ECT-like and the spin flipping tunneling is CAR-like. Hence the ECT and CAR description is still qualitatively accurate and the system can still be parametrized by t and Δ values.

To summarize, the previous sections have detailed the Kitaev chain model, the quantum dots used as the building blocks in this model, the Andreev bound states which control the couplings and the resulting interactions and how we can measure them. The next chapter will describe the experimental methods before we discuss the results of the two projects.

Chapter 3

Method

QUANTUM transport measurements rely on an interplay of classical electronics and the quantum chip. We cover the basics of the measuring techniques here briefly.

3.1 Device Components

Experiments in this thesis are done on a 2DEG device, placed at sub-100 mK temperatures in a dilution refrigerator. In this device quantum transport measurements are conducted; we deduce information about the physics in the device by measuring current and into and out of the device.

Three components are involved in transport: leads, tunnel barriers and discrete quantum states [30].

- Leads are large reservoirs of electrons that are connected to classical circuits and have well-defined current and voltage values. We consider them to be at equilibrium and at zero temperature. On the energy scales that we consider the density of states of a metallic lead can be approximated to be constant [30]. The states below μ_{lead} are all filled with electrons and the states with higher energy are all unoccupied. For a superconducting lead, the density of states has an energy of 2Δ and is well-described by the BCS theory [33].
- Tunnel barriers are defined by setting a voltage on an electrostatic gate. They create a potential barrier that affects the transmission rate of every charged particle going through them. We make the simplifying assumption that transmission does not depend on particle energy. They are also used to define confined regions, such as to make quantum dots.
- Discrete states exist as a function of the configuration of the gates in the system. In a transport cycle, the system starts from an initial state (often assumed to be the ground state), an electron at a specific energy is injected, the system transitions to another state depending on that state's energy and parity, the electron relaxes to another lead and the system relaxes to the initial state again. The system is then ready for another transport cycle, and a net current has been measured. These transport cycles occur at a much smaller timescale than our measurement times.

3.2 Measurement Procedures

The experiments reported in this thesis are electron transport measurements with 3 normal metallic leads and one superconducting lead. The superconducting lead is always grounded and its Fermi energy defines the reference for the other energies in our system. We set the voltage biases V_L, V_M, V_R at the normal leads, and then measure the resulting currents I_L, I_M, I_R as illustrated in Figure 3.1.

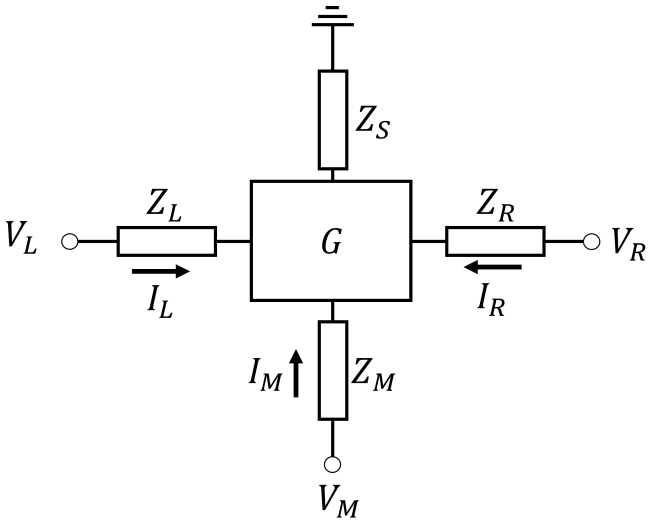

Figure 3.1: The mesoscopic device with its conductance matrix G is connected to three voltage sources V_L, V_M, V_R. The currents I_L, I_M, I_R are shown. Positive current is defined as going into the device. The impedances Z_L, Z_M, Z_R, Z_S are the line impedances that arise from the connection between the leads on the device and the classical room-temperature electronics.

When tuning the mesoscopic device the resistances caused by tunnel barriers are inevitably asymmetric, and line impedance asymmetry is also a possibility. These differences cause the voltages set by the external electronics to not exactly correspond to what voltages are applied at the device level, called a voltage divider effect [30, 52]. We did not correct for these in this report although we will point out when these effects occur.

3.2.1 DC Measurements

Besides the currents, we can also gain information through the system by measuring the differential conductance $G = \frac{dI}{dV}$. It can be shown that as both the temperature and transmissions tend to 0, the differential conductance is directly proportional to the density of states within the superconducting gap [40].

The differential conductance can be measured directly through a lock-in amplifier, which sends out an AC signal at a specific frequency ω_0 that is added to the applied DC voltage. The total voltage which is applied to the lead is $V_{DC} + V_{AC}\sin(\omega_0 t)$, and the resulting current response is :

$$I(V_{DC} + V_{AC}\sin(\omega_0 t)) \approx I(V_{DC}) + \frac{dI}{dV}\Big|_{V_{DC}} V_{AC}\sin(\omega_0 t) \tag{3.1}$$

given that V_{AC} is small enough. The current meter measures the average value of the current, while the lock-in amplifier measures the magnitude of the oscillating term $\frac{dI}{dV}\big|_{V_{DC}}$ while filtering out other frequencies. This suppresses noise compared to manually taking the derivative of current in a purely DC measurement but comes at the cost of slower measurements since the lock-in requires averaging over several periods. Due to low-pass RC filters in the fridge lines protecting the electrons in the device from thermalizing through high-frequency noise leaking into the fridge, we cannot measure at frequencies much higher than 30 Hz without measuring a background signal from the capacitors in the lines. This limits the speed of high-quality measurements to tenths of a second per measurement point.

A non-local differential conductance measurement refers to measuring the lead response when another lead's chemical potential is varied. We use the convention that

$$G_{ij} = \frac{dI_i}{dV_j} \tag{3.2}$$

For example, G_{ML} measures the response at lead M to a change in the bias at lead L. Non-local measurements with two normal leads and one grounded superconductor can be shown to be equivalent to measuring the charge of the measured excitation [53]. With three normal leads, the conservation of charge argument which is used in that derivation is not valid, so the intuitive meaning behind the non-local measurements is unclear. Despite this complication, we still observe remarkable agreement behind rate-equation simulations and measured non-local conductance in this report.

3.2.2 RF reflectometry

Another measurement technique utilized in this thesis is Radio Frequency (RF) reflectometry on the normal leads. This involves applying a high-frequency AC signal on an LC resonator which is coupled to a lead on the quantum device and measuring the power of the reflected signal. Due to the high frequency, a different transmission cable is required. When the frequency corresponds to the resonant frequency f_r of the resonator, the reflected signal is highly sensitive to small changes in the resistance in the lead. This has important applications, for example for charge sensing in quantum devices [38, 54].

In this report, especially for measuring charge stability diagrams, we use RF lead reflectometry as a proxy for differential conductance as they are expected to qualitatively correspond [55]. We show pinch-off measurements in both current and RF reflectometry in Figure 3.2, where we use a gate to go from an open to a completely closed transport channel with one lead at 400 µV and the other leads grounded. The signals qualitatively agree, although the RF reflectometry signal does not correspond to conductance one-to-one, and even is sometimes non-monotonic (such as in the middle lead).

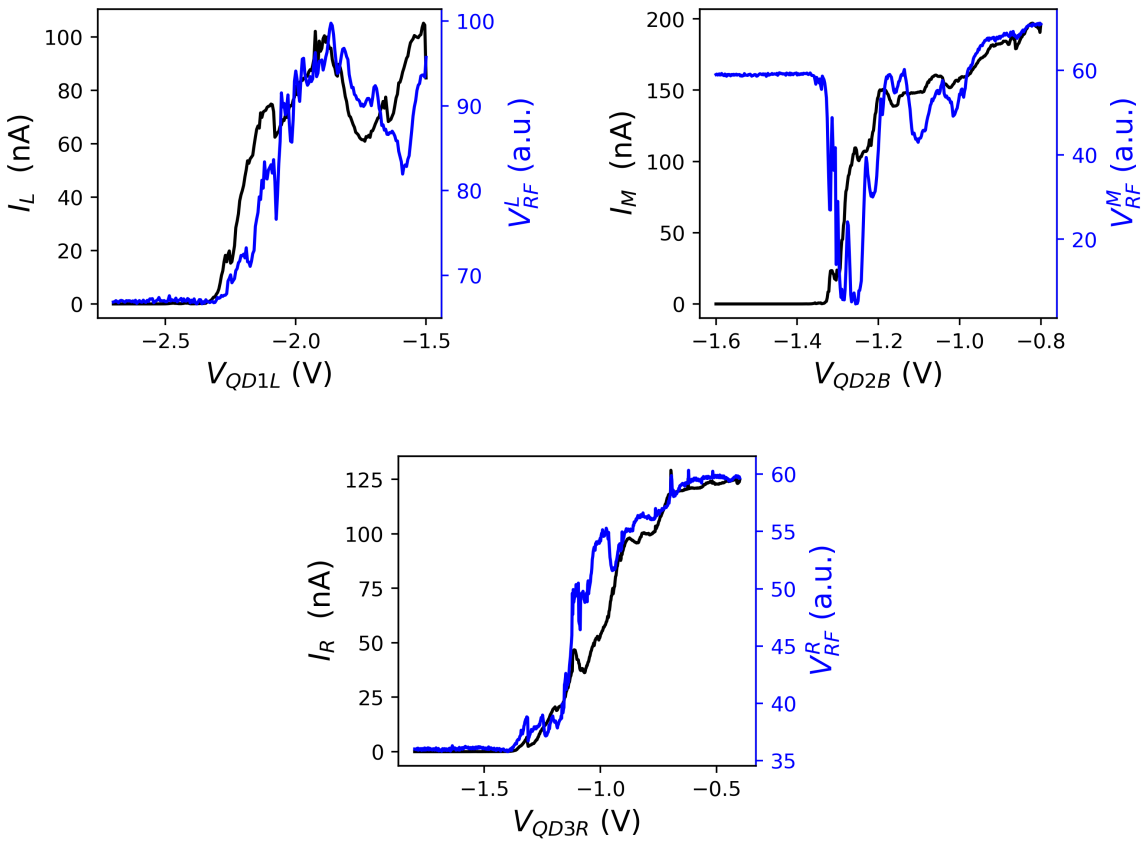

Figure 3.2: Pinch-off measurements for one gate each from the left, middle, and right leads. The current and the V_{RF} signals are measured simultaneously. Note that they are plotted on different axes.

The main advantage of doing RF measurements in our setup, where the measurements we are interested in are spectrum measurements to measure the density of states, is the speed at which those measurements can be done. For example in this report, most measurement points where RF was used were measured for about a millisecond. This time is of the same order of magnitude as the time it takes for the voltage biases or voltages applied on the gates to be changed through the control rack, which reduces the use of measuring this fast. The usage of an Arbitrary Wave Generator (AWG) solves this issue by sending out a continuous sawtooth wave onto either the lead or a gate to change the device state smoothly - allowing for continuous fast RF measurement. This technique is called rastering.

Throughout the measurements presented here, the experimental wiring went through several iterations. Figure 3.3 shows a simplified diagram of the final, most flexible measuring setup, for a single lead and a single gate.

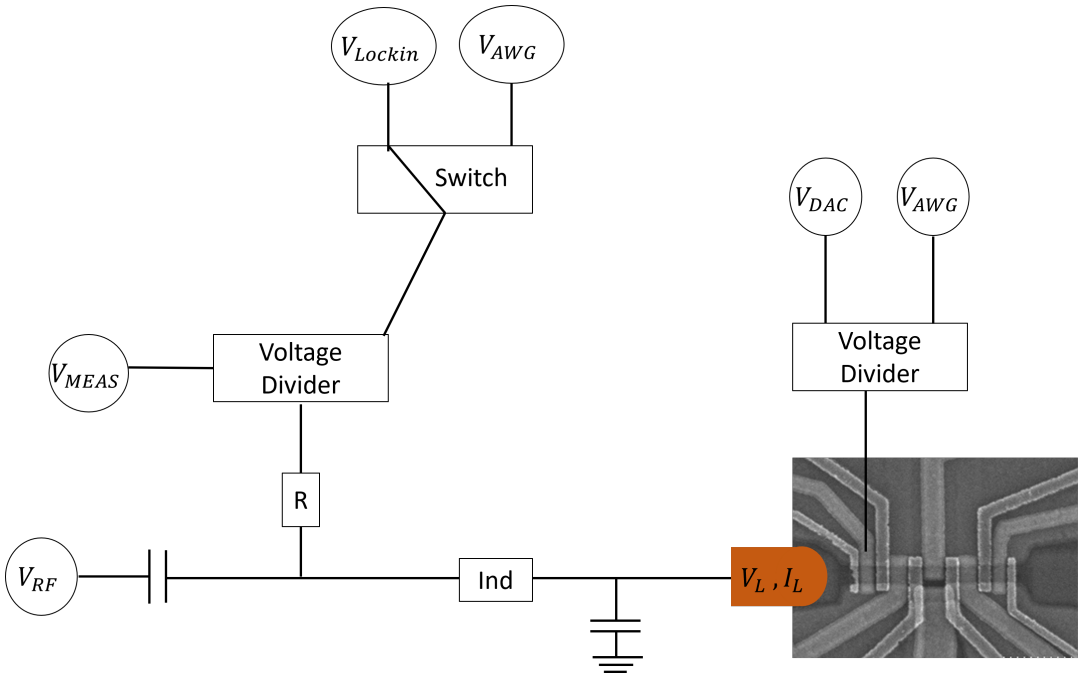

Figure 3.3: A simplified diagram for a wiring setup capable of direct differential conductance measurements as well as 1D and 2D rastering measurements, shown for the left lead and left plunger gate.

In the above circuit, V_{RF} is the high-frequency signal that is capacitively coupled to the lead, which we use to measure RF reflectometry. V_{MEAS} is the DC voltage set by the control rack, which we consider to be equal to V_L, and is capable of measuring I_L. Differential DC conductance can be measured through V_{lockin} and the lead can be pulsed with a smooth voltage wave by V_{AWG} for rastering measurements while V_{RF} is applied and measures the reflected signal. The switch flips from one to the other depending on the measurement. Separately, the voltage which is felt by the plunger gate is applied by V_{DAC}, on top of which another voltage pulse can be applied by a separate AWG.

This wiring was applied for the three normal leads and the three plunger gates in the device. Pulsing one AWG and measuring RF reflectometry is a 1D rastering measurement, but both AWGS can also be used for a 2D rastering experiment. In that case, one of the AWGs applies one pulse with a period of the length of the full measurement, while the second AWG emits very fast sawtooth pulses.

Chapter 4

Flux Tunable Minimal Kitaev Chain

4.1 Motivation

Minimal Kitaev chains implement the Kitaev chain model in the minimum number of fermionic sites to have delocalized Majorana bound states. These MZMs that appear at a specific point in parameter space are known as Poor Man's Majoranas [20], since they do enjoy Majorana non-Abelian properties but are only protected quadratically against global chemical potential fluctuations and are not protected against inter-QD coupling fluctuations. In this chapter, we will discuss a tuning mechanism to reach the PMM regime which has not yet been explored experimentally.

Minimal Kitaev Chains have since their recent realization in InAs - Al hybrid nanowires [26] been tuned into the Poor Man's Majorana regime by modulating the chemical potential of the Andreev bound state coupling the quantum dots. This is accomplished by electrostatically gating the ABS [51]. The crossover from the ECT-dominated to CAR-dominated regimes with this approach is well-understood and has been demonstrated in more systems since, such as with strongly proximitized quantum dots [50], in three dot chains [56], as well as in 2D electron gases [27].

Although the initial realization of minimal Kitaev chains only featured one superconductor, a two-dot Kitaev chain may also be engineered by coupling the ABS to two superconductors connected through a loop. By varying the flux - an out-of-plane magnetic field passing through a loop - we may control the superconducting phase difference between the two superconductors, affecting the charge and energy of the ABS between them and thus changing the transport through a system coupled to the ABS. How the flux affects the charge for the ground state of a single ABS is shown below in Figure 4.1.[1]

[1]We thank Juan Torres Luna for providing the code for this computation. [48] The code is available at https://zenodo.org/records/10579410 .

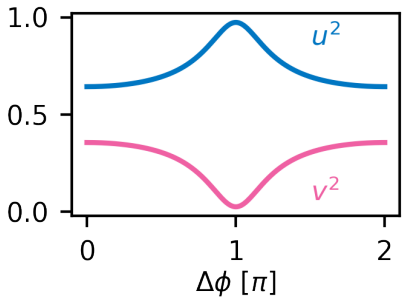

Figure 4.1: The u^2, v^2 components of the ABS ground state $|S_-\rangle = u|0\rangle - v^*|\uparrow\downarrow\rangle$ for a specific chemical potential plotted as a function of the phase difference between them.

In parallel with the work done on Kitaev physics, the Goswami lab has investigated using flux to control Andreev bound states in a Josephson Junction in InSbAs [57] as well as tunneling interference in a double quantum dot interferometer in InSbAs [58]. This research paved the way for measurements of the flux-dependence of transport mediated by ABSs in coupled quantum dots, where a clear flux dependence of elastic co-tunneling was observed [36]. Crossed Andreev Reflection also showed flux response, but the agreement with the expected theoretical results computed from a single ABS model was quite poor. Nevertheless, their experiment suggested that flux tuning the coupling between two quantum dots is possible, opening the possibility of a two-site Kitaev chain that can be tuned in and out of the PMM regime through flux alone.

Parallel theory work has shown this to be possible [48]. The charge control could allow tuning of the type of interaction between the coupled QDs, and the change in energy affects the strength of both spin flipping and spin conserving coupling. In the proposed model featuring a single ABS with asymmetric coupling to the superconducting leads flux tuning is not only possible but also results in a more protected PMM and a higher excitation gap when the phase of the ABS is π, which would not be achievable in a PMM tuned with only one superconductor.

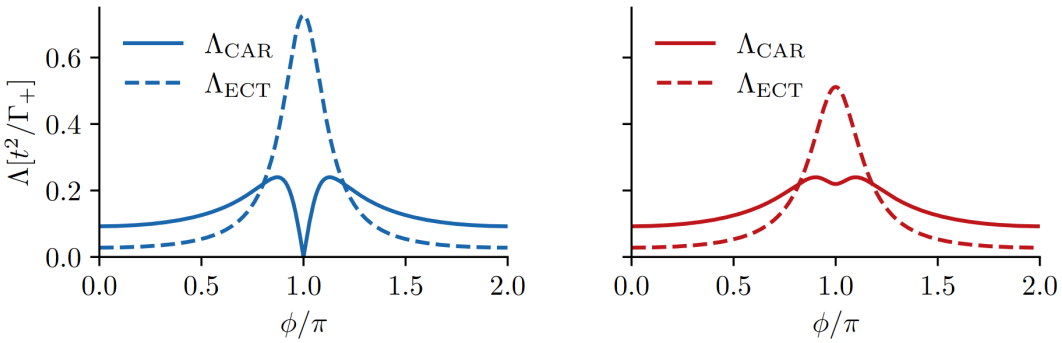

Figure 4.2: The rates for elastic cotunneling (Λ_{ECT}) and crossed Andreev reflection (Λ_{CAR}) plotted against phase difference, for the same coupling strength to both superconductors (**left**) and a slight coupling asymmetry (**right**). The units on the y-axis are normalized by using the problem's natural units, detailed in [48].

Furthermore, tuning through the ABS chemical potential only offers two sweet spots per Andreev Bound state. These sweet spots can be adjusted through a rotation of the Zeeman field [23] which offers a degree of freedom, but changing the field is slow and requires a regime where spin-flipping hopping is greater than spin-conserving hopping. The approach may be faster and offer more flexibility, by allowing a sweet spot to be found for any chemical potential value.

In this chapter, we will first present the device where the results were measured, explore some novelties in this device that have not been measured in PMM systems before such as relatively long PMM coupling and probing of the hybrid region in the PMM regime, and conclude by presenting the flux tuning results.

4.2 Device Geometry

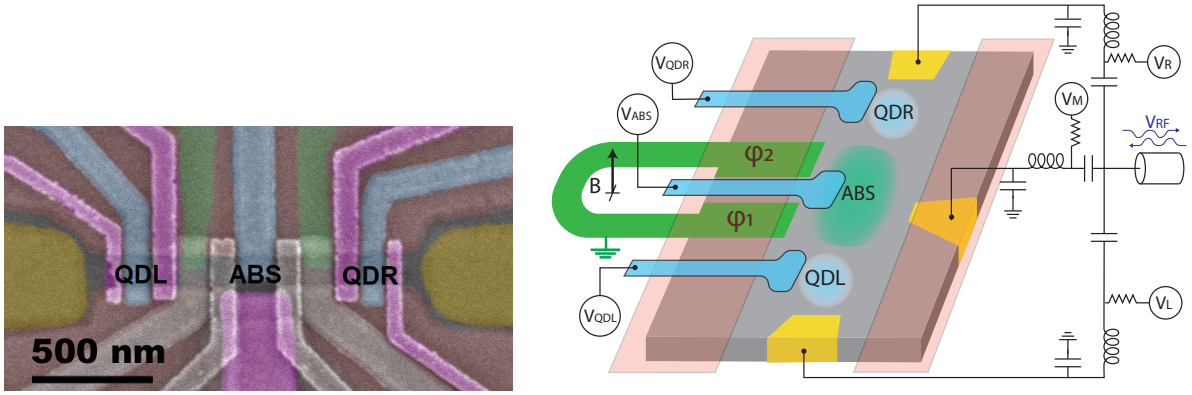

Figure 4.3: Left. A false color SEM of the device. The regions where the left and right quantum dots and the Andreev bound state coupling them are defined are labeled. **Right.** Schematic showing how the chemical potentials are controlled, the flux control through the superconducting loop, and the wiring for DC and RF measurements. Drawn by Ivan Kulesh.

The device used during the experiments[2] is shown in Figure 4.3. The gates used are highlighted in Figure 4.3. Gates that are not colored were not used in these experiments and were kept grounded. The plunger gates are colored blue, the tunnel gates are colored pink, the normal leads are colored gold and the superconducting leads are colored green.

The schematic on the right highlights the gates that control the relevant chemical potentials and shows the circuit connected to the leads which is used to measure the device. The lead voltage sources V_L, V_M and V_R were initially only DC sources. Later improvements to the measurement setup allowed connecting the leads to AC voltage sources, allowing differential conductance to be measured directly.

The three leads and the gate plungers can accommodate AWG signals which we use for rastered RF reflectometry measurements as detailed in subsection 3.2.2. This was crucial for tuning the device and exploring wide ranges of parameter space that would have been inaccessible to us at the speeds offered by DC measurements.

[2]Device fabricated by Qingzhen Wang.

The superconducting leads, which due to their galvanic connection will be at the same voltage, are kept grounded throughout these experiments. Therefore the leads can accept Bogoliubov quasiparticles, allowing processes such as ABS relaxation or local Andreev reflection, but they cannot accept single electrons or holes.

The device geometry differs from previous devices used to investigate flux-tuning PMMs in a significant way: the superconducting flux loop is in a different position, as can be seen in Figure 4.4. In previous systems, the superconducting leads did not show coupling which was asymmetric enough to show non-trivial behavior when flux-tuning in the PMM regime was attempted. More spatially separated superconducting leads are less likely to have the same coupling to the hybrid section.

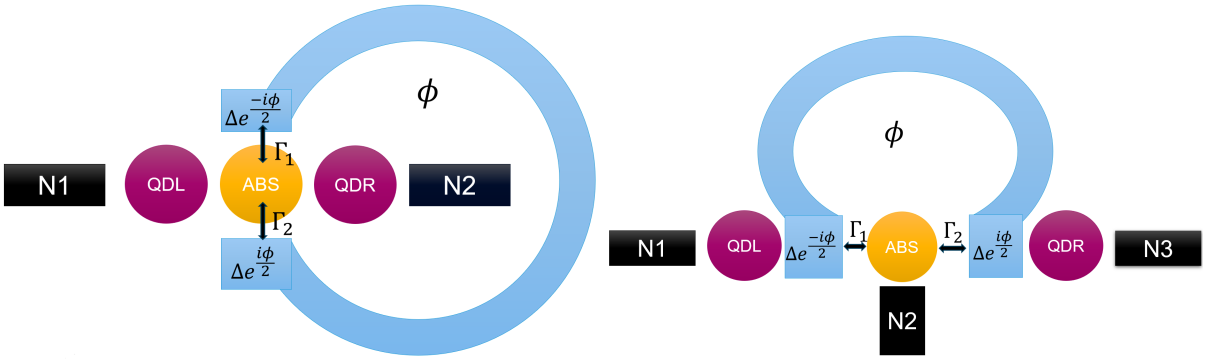

Figure 4.4: Left. A schematic for devices used in [36], featuring superconducting leads across from each other with respect to the channel. These leads couple to the ABS with coupling strength Γ_1, Γ_2. The normal leads are labeled N1 and N2. A flux ϕ can be applied through the loop. **Right.** A schematic showing the configuration for the device used in this report, highlighting the different positioning of the loop as well as the addition of a middle lead.

The configuration used here, shown on the right in the figure above, has a third normal lead bringing with it the added complexity of tuning a tunnel barrier which also plays a role in confining the ABS. However, it does open up the possibility of performing ABS spectroscopy while the quantum dots are formed and allows the spectrum of the PMM excitations to be measured from the middle, which has never before been done.

The length of the proximitized semi-conductor is also a novelty. In both nanowire and 2DEG PMM systems, the typical size of the hybrid section is roughly 200 nm [26, 27, 50, 59], while here the distance between the quantum dots' inner barriers is approximately 800 nm. This length approaches aluminium's superconducting coherence length of 1600 nm, leading to the question of whether the energy dispersion as a function of flux given by the short junction approximation holds [57] and whether we can probe the same ABS from all sides. We will start by answering these questions,then discuss the investigation of the PMM coupling in this system, and lastly summarize the findings on flux tuning of the PMM.

4.3 Probing the Andreev Bound State

As the goal of this experiment is to show we can use flux to tune a 2-site Kitaev chain to the Poor Man's Majorana regime, which requires the flux to be able to tune the ABS. We will therefore first demonstrate that we do indeed have the expected control over both the chemical potential and the phase of the ABS.

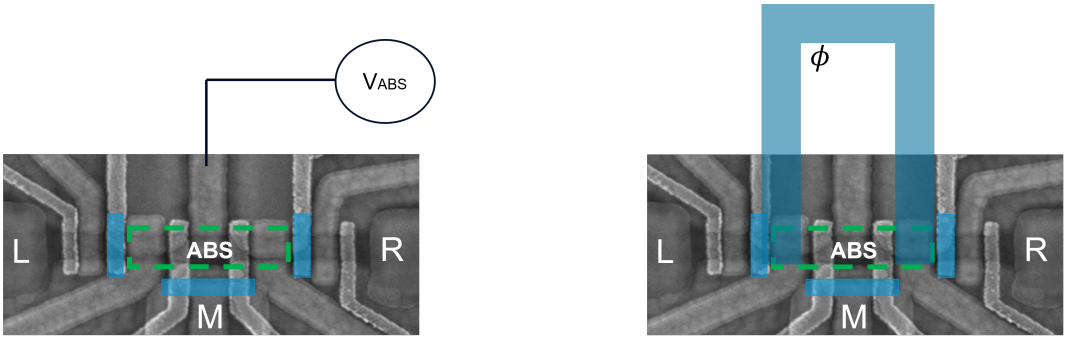

Figure 4.5: Schematics of the measurements shown in this chapter. The light blue squares indicate tunnel barriers, tuned to measure the density of states in the proximitized region. **Left.** Control over the ABS region using gate voltage to vary μ_{ABS}. **Right.** Control over the ABS region using flux through the superconducting loop to vary $\Delta\phi$.

4.3.1 ABS at 0 Field

The ABS energy spectrum is least complicated without an external magnetic field, since without a Zeeman field ABS splitting effects due to spin-orbit interaction and spin polarization are absent [60]. Figure 4.6 shows the tunneling spectroscopy from the left, middle, and right for the same range of plunger gate voltages. In this measurement local Andreev reflection is suppressed, showing the hard gap of the proximitized region. We may still resolve sub-gate bound states through resonant Andreev tunneling, which is the state we observe in the plot.

The lead voltages are directly equivalent to the energy differences between the even and odd states in the system (since injecting an electron or hole necessarily changes the parity of a state). The gate voltage is related linearly to the chemical potential of a state, which is 0 at the energy minimum - when the symmetric positive and negative energy states are closest to each other. The factor $\alpha \in [0, 1]$ relating the chemical potential and the gate voltage is the lever arm and can differ between different states depending on the microscopics.

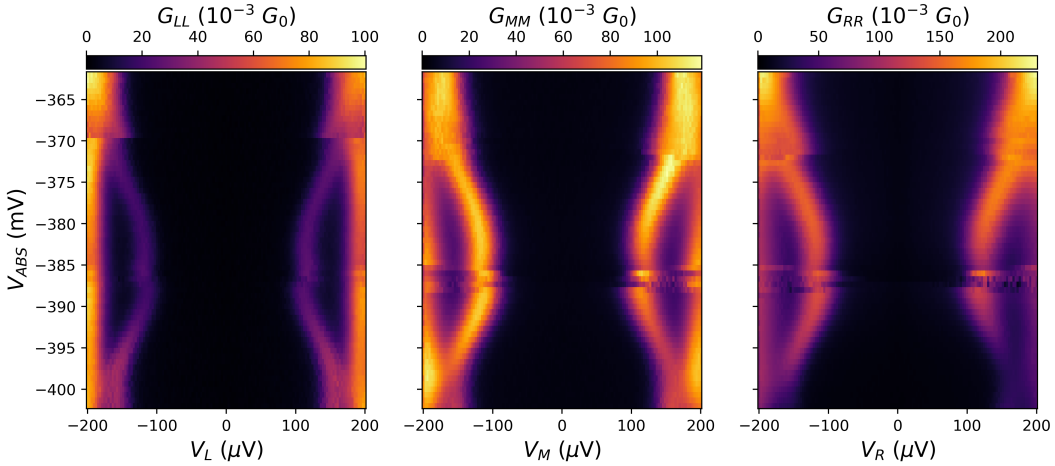

Figure 4.6: Tunneling spectroscopy of the proximitized region performed from the left, middle and right leads.

In the above case, the same isolated ABS can be seen from all leads, indicating that there is sufficient tunneling between the leads and the ABS from all leads and that these sub-gap states were delocalized across the entire hybrid section. During the measurement the flux loop is kept at 0 phase - this calibration is detailed later and is necessary due to magnet offsets.

We also observe discontinuities in the measurement - such as at -385 mV - which are due to sudden discharges in the environment, commonly labeled charge jumps. Such jumps are common in mesoscopic systems and can happen stochastically or reproducibly [19]. These jumps occurred often in this specific device setup, being typically observed every 10 or 15 mV in the ABS plunger gate which is more frequent than when we measured shorter ABSs in chapter 5. We attribute this to the higher statistical likelihood of charges being captured in the electrostatic environment due to the increased size of the region. Most of these jumps were observed to be reproducible.

We now turn to the phase control. In the model where we consider the ABS to be a quantum dot strongly coupled to two superconductors with coupling Γ_1, Γ_2 respectively, the ABS energy is still $E_{ABS} = \sqrt{\varepsilon_0^2 + \Gamma_s^2}$ as shown in Theory section 2.3. However the superconducting coupling is now a function of the phase difference [48]:

$$\Gamma_s = \Gamma_+ \sqrt{1 - \tau \sin^2(\phi/2)} \tag{4.1}$$

Where $\Gamma_\pm = (\Gamma_1 \pm \Gamma_2)/2$. The effective transparency of the $(\Gamma_+^2 - \Gamma_-^2)/\Gamma_+$. For perfectly symmetric coupling, $\tau = 1$.

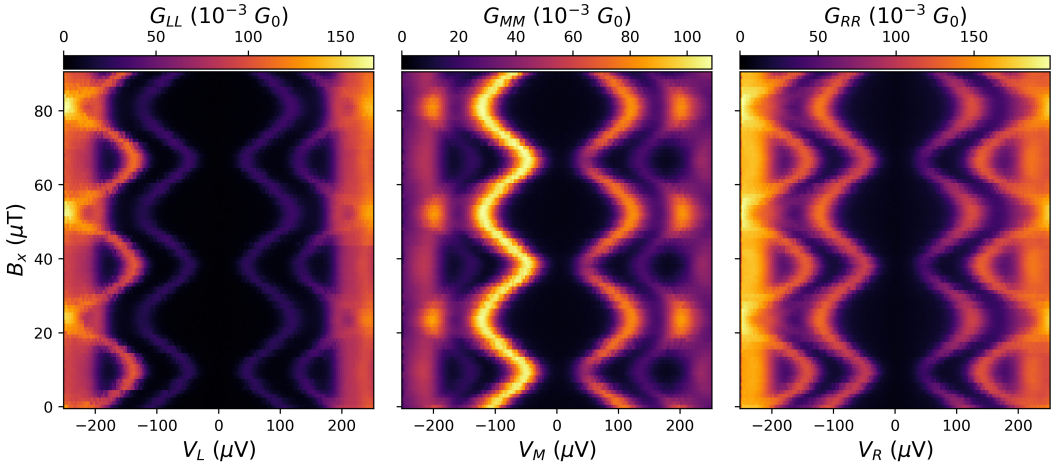

Figure 4.7: Tunneling spectroscopy of the proximitized region performed from the left, middle and right leads upon varying the flux. The ABS plunger is set to -390 mV in the same regime as Figure 4.6. Such measurements are used to confirm the periodic relationship, and to calibrate the phase - as can be seen here, a phase offset is present. We interpret the asymmetries in conductance and broadening between the positive and negative energy excitations as tunnel barrier imperfections.

In Figure 4.7 we vary the out-of-plane magnetic field, causing a variation of the superconducting phase difference across the Josephson Junction. The state responds periodically, observed again from all three leads. The energy maximum corresponds to a phase of 0 - up to a multiple of 2π - and the energy minimum corresponds to a phase of π, again modulo 2π. There is also no zero crossing, indicating an asymmetric effective transparency.

We observe a period in B_x of 27.5 $\pm$ 0.5 uT, which corresponds to a flux area of $S = \frac{\phi_0}{B} = 7.5 \times 10^{-11}$ m^2, where ϕ_0 is the flux quantum. For a perfectly circular loop, this would imply a radius of about 5 μm, which is in line with the size of our device.

We can also see a second resonance, starting in the quasiparticle continuum above the hard gap, which is pulled down in energy with the same periodicity as the ABS which is resolved at $\Delta\phi = 0$. We interpret this as another Andreev bound state, which would be unresolvable from the gap edge without any phase control.

4.3.2 ABS at Finite Field

We want to ensure we have the same control at finite field, which we need to spin-polarize the QDs. At finite field, we expect a reduced hard gap, Zeeman splitting in the ABSs, and lower ABS resonance energies. We also expect the flux dispersion to be more complicated due to spin-orbit effects [60].

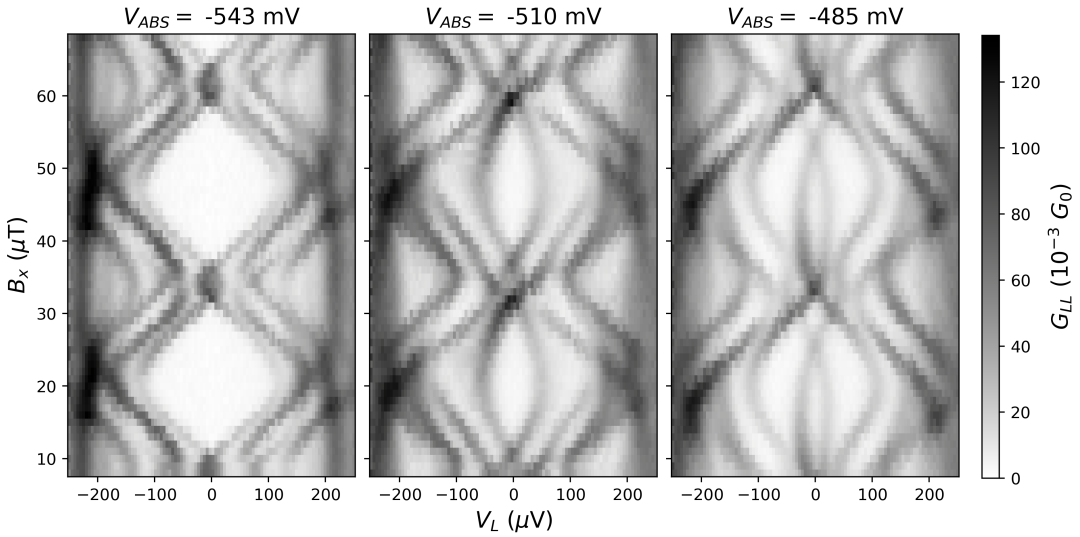

Figure 4.8: ABS flux dependence at 150 mT for three different plunger values, measured from the left lead. Horizontal shifts are caused by Zeeman splitting and vertical shifts are caused by spin orbit coupling. The colormap was chosen to show the most contrast between the different subgap states.

In Figure 4.8 we show the flux spectrum at three different plunger voltages. Zeeman splitting (splittings in energy) and spin-orbit coupling (splitting in flux response) complexify the spectrum significantly [60]. Despite these effects, the spectrum is still gapped for most flux values. Even in the best-case scenario, of which the left plot is a good example, we cannot easily compare our results to the single ABS model or have a non-zero state at π-phase. At most plunger values we investigated, the flux response looks similar to the middle plot, where approximately 3/4 of the period is gapped enough for resonant Andreev tunneling not to occur for electrons at the Fermi energy - as explained in Theory section 2.4. Furthermore, there are some plunger values - such as in the right plot above - where the gap is too small at almost all values of B_x.

4.4 Long Range PMM Coupling

4.4.1 YSR Dots

An essential ingredient in coupling two quantum dots through an ABS is of course the quantum dots themselves. In this experiment, the quantum dots were strongly coupled to the superconductor to form Yu-Shiba-Rusinov (YSR) states as detailed in Theory section 2.3. At finite field, these are spin-polarized fermionic sites that can be used to form a PMM state with a greater energy gap and improved robustness to charge fluctuation than with non-proximitized quantum dots [50]. Similarly to ABSs charge is no longer a good quantum number for YSR states as the $|0\rangle$ and $|\uparrow\downarrow\rangle$ states hybridize into two singlet states, but unlike ABSs they retain a significant charging energy compared to the superconducting gap Δ.

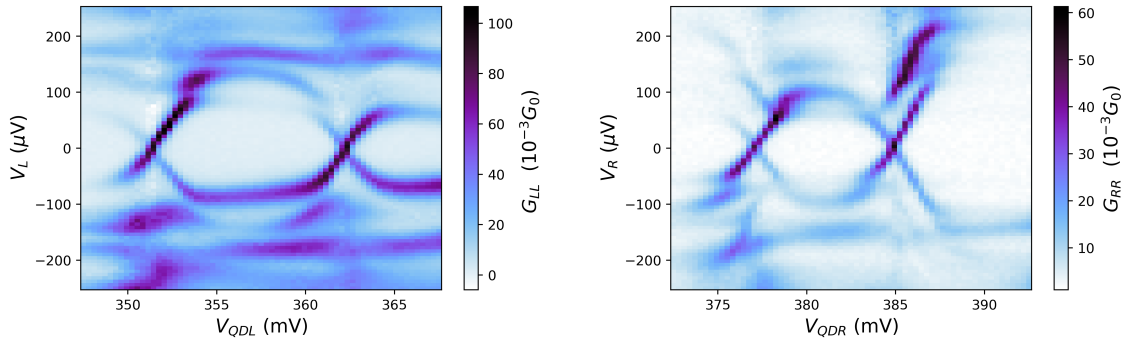

Figure 4.9: Low-energy spectrum plotted against gate voltage of the YSR states which form the fermionic sites in our 2-site Kitaev Chain, with a spin polarizing field of 150 mT.

Due to some high-bias noise present in our setup we were unable to obtain clean characterizations of our quantum dots at high energy. Similar devices fabricated in exactly the same way typically have charging energies between 1 and 2 meV and above-gap lever arms of ≈ 0.1 [25]. The sub-gap lever arms at zero energy, which we extract from the data in Figure 4.9, are $\approx$ 0.046 left and ≈ 0.042 right. This is very close to previous observations in similar devices [27].

Turning on a magnetic field increases the level spacing in the quantum dot through Zeeman splitting. For these dots, we measured that a field of 300 mT leads to an increase in level spacing of ≈ 4.2 mV left and ≈ 1.4 mV right in terms of the plunger gates. With the estimated lever arms, we extract a Landé g-factor of ≈ 22 and ≈ 7 respectively. [3]

4.4.2 ECT and CAR coupling

Coupling the dots to the Andreev bound states in the hybrid is an iterative process of increasing the coupling between QDs and the ABS, investigating different dot orbitals and ABS plunger gate ranges, and looking for relatively stable regions in parameter space.

It was quickly clear that, despite the length of the hybrid and the ABS wavefunctions not necessarily being equally coupled to all leads, both CAR and ECT coupling were present in our system - as highlighted in Figure 4.10.

[3] We may find g by rearranging the formula $E = \alpha V = \frac{\mu_B}{2} gB$. Note furthermore that due to hybridization between the dots and the ABS changing as a function of the Zeeman field, this is only an estimation. The true g-factor of a proximitized quantum dot must be obtained by measuring bias versus field at a fixed plunger gate value as in [50].

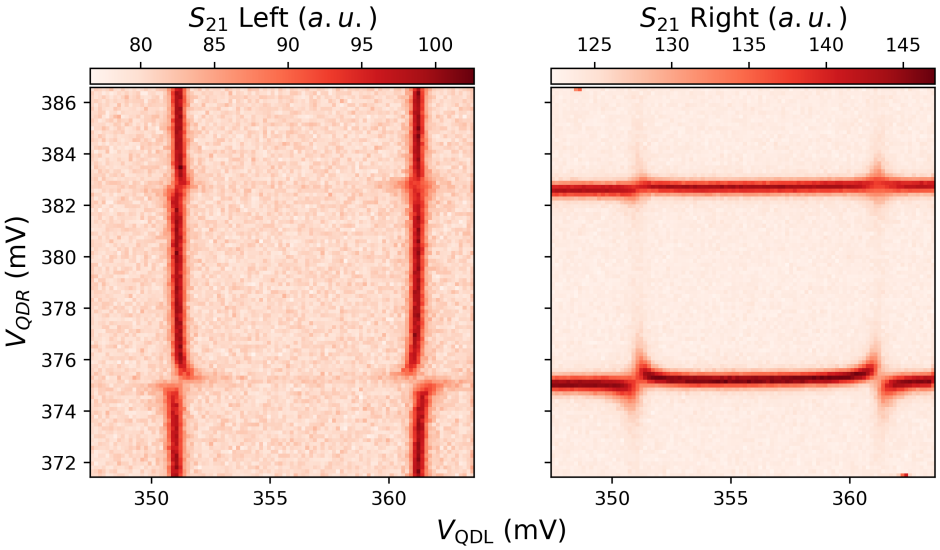

Figure 4.10: Resonator signal on the left and right leads when measuring a charge stability diagram. Obtained by averaging 15 measurements. We see different regimes: CAR-dominated interaction in the lower right avoided crossing, ECT-dominated interaction in the lower and upper left avoided crossings, and a sweet spot (equal interaction) on the upper right.

4.4.3 Demonstration of strong PMM coupling

To show that we can truly have a large gap PMM in this system, we will show that a similar excitation gap of 50 µV can be obtained in this system as was measured in a similar device at the same Zeeman field of 150 mT [27], and furthemore that the states behave as expected in response to detunings from the Majorana sweet spot.

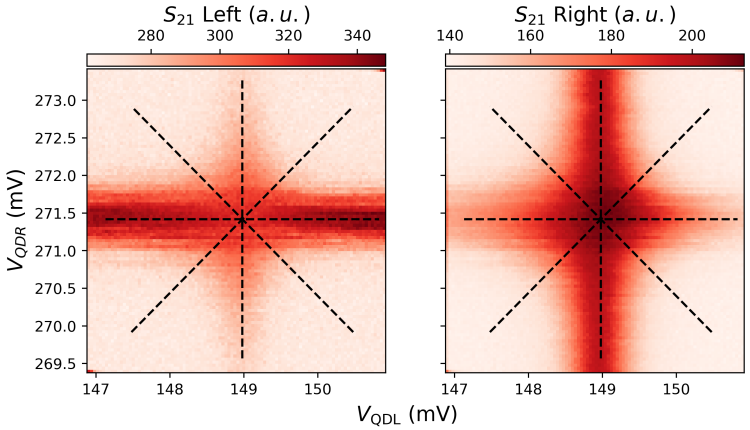

Figure 4.11: Charge stability diagram showing a resonance tuned to the sweet spot, at which the following spectra were measured. The dotted lines show all the possible detunings we will show in Figures 4.13 and 4.14.

The sweet spot we investigate is shown above, in Figure 4.11. The center of the above plot corresponds to $\mu_L = \mu_R = 0$ and $t = \Delta$, the Poor Man's Majorana sweet spot. We can take a

spectrum measurement at each lead, meaning we measure the density of states. This is plotted below in Figure 4.12.

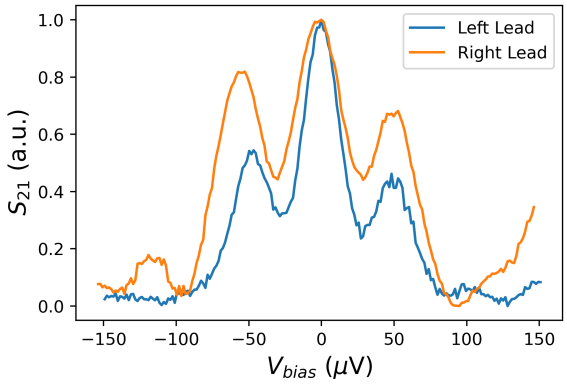

Figure 4.12: Spectrum at the PMM sweet spot. RF signal is normalized between 0 and 1 to easily compare signal from the left and right.

The spectrum shows an isolated *zero bias peak* (ZBP) and two symmetric peaks at positive and negative energy corresponding to the excited states. This is what we expect to see for a PMM [26]. A voltage divider effect is present, as the peaks are not exactly aligned. Although we cannot correct for this effect here, this correction has been described well for 3 terminal measurements in [52]. For a 4 terminal setup such as ours the correction may be more involved.

These correlated zero-bias peaks are not enough to prove we have a PMM. We should also demonstrate that they exhibit the expected protection against disturbances in the chemical potential. For weakly coupled quantum dots at the sweet spot, a detuning of a single chemical potential $\mu_1 \neq \mu_2 = 0$ will not destroy the zero energy Majorana state [32]. Rather, a gradual vanishing of the zero bias peak on the detuned dot is expected while the ZBP on the other dot remains stable. The excited states are expected to increase in energy proportionally to $\sqrt{\frac{\mu_1^2}{4} + \Delta^2}$. The detuning spectrum is quantitatively different for strongly coupled dots, but the qualitative behavior remains the same [49]. The single dot detuning results are shown in Figure 4.13.

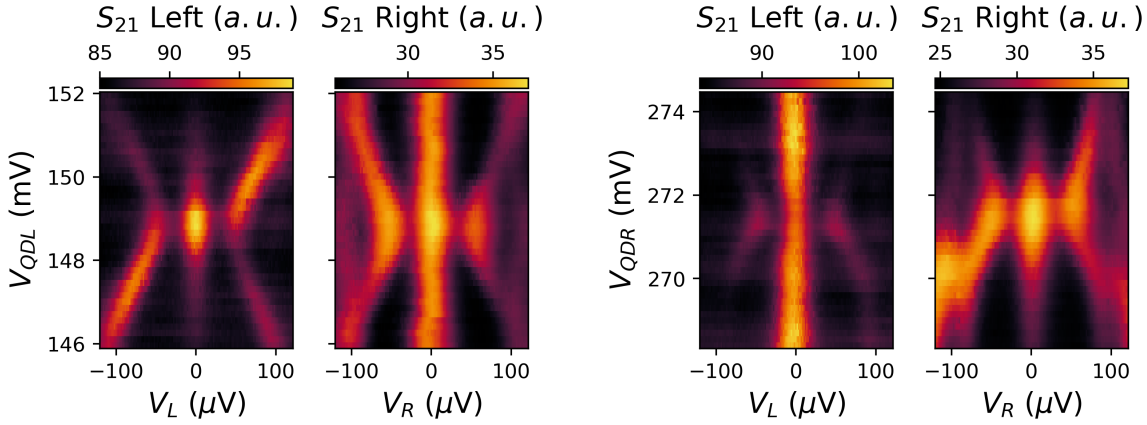

Figure 4.13: Reflectometry spectrum on the left and right leads when detuning the left and right dots from the sweet spot, respectively.

The Poor Man's Majorana is quadratically protected from global charge fluctuations, meaning that the ZBP is not stable when $\mu_L, \mu_R \neq 0$. The simultaneous dot detunings are shown in Figure 4.14.

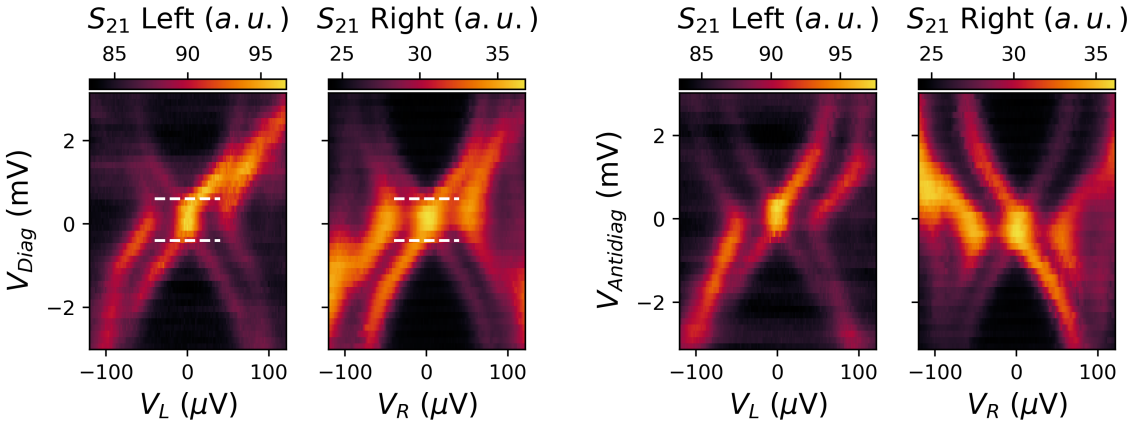

Figure 4.14: Reflectometry spectrum on the left and right leads when detuning both dots simultaneously, with the same sign and with the opposite sign. The dotted white lines left emphasize the 1 mV range where we cannot resolve the splitting due to temperature effects and level broadening.

To conclude, we have shown that a PMM is possible in this system without any decrease in interaction strength despite the spatial separation of the coupled quantum dots.

4.5 Investigation of the PMM Excitation Through the Middle Lead

We have shown how strong PMM coupling is possible over the long ABS we have in this device. To do so, we proximitized the quantum dots - which in a minimal Kitaev chain leads to a greater excitation gap at the cost of leakage of the Majorana wavefunction into the ABS [49]. Although past PMM devices have always had superconducting leads coupled to the hybrid region, such a lead does not allow measurement of sub-gap states since it cannot inject fermionic excitations within the superconducting gap due to its Cooper pair condensate. The additional normal lead in our device which can perform tunneling spectroscopy does give us access to the Majorana wavefunction in the hybrid.

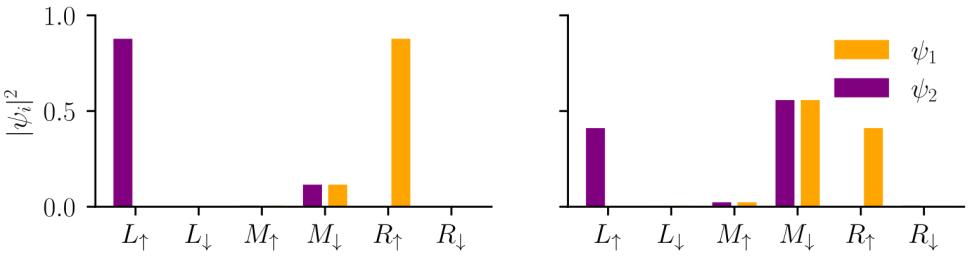

Figure 4.15: The wavefunction of the Majorana wavefunctions ψ_1 and ψ_2 in the full QD-ABS-QD model, in the weak (**left**) and strong (**right**) regimes, plotted at each site in a spinful QD-ABS-QD model. The wavefunction overlap in the ABS (site M) is clear, although this overlap is not detrimental to the Majorana beyond reducing its visibility to the external system [49]. Figure taken from [48].

The device configuration allows us to probe the PMM from the center, unlike any other devices hosting PMMs before [26] [50] [27]. We will therefore explore whether we can measure the Majorana wavefunctions overlap in the center, as suggested by the PMM wavefunction localization as graphed in Figure 4.15.

In the following figures, we show detuning spectra for a different PMM from all three leads, measured in conductance. We will compare qualitatively the behavior with simulations, generated using the rate equation method on exact diagonalization of a QD-ABS-QD spinful model, as in [49] and detailed in [61].[4] We first show the measured spectrum when detuning the left dot, in Figure 4.16.

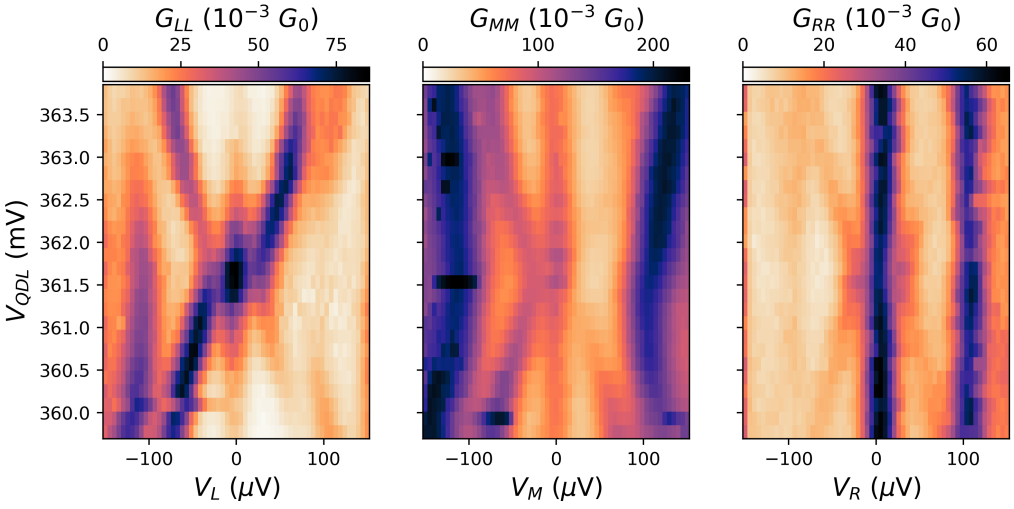

Figure 4.16: The local conductances when varying V_{QDL} around the sweet spot. Note that each spectrum is plotted at a different scale.

We can measure the ZBP from the middle lead, although the relative conductance of the ZBP compared to other features is less. In the outer QDs, the maximum conductance is at zero bias, while in the middle we observe the highest conductance at the higher energy excited states. In particular, features above $100\mu V$ are visible in the center while being barely probable from the outer leads. These are independent of the dot plungers, suggesting that they are ABSs

[4] We thank Mert Bozkurt and Bas ten Haaf for providing the code for these computations.

that do not couple to the dots. Charge carrier tunneling from the outer leads into these ABSs is suppressed by the dot inner and outer barriers, while it is only affected by one barrier in the center which explains why these features are mainly visible in G_{MM}.

While the zero bias peak and both the excited states are visible left and right, one of the excited states is not probable in the center. This is captured by the simple QD-ABS-QD model, as illustrated in Figure 4.17. The reduced conductance of the ZBP in the middle probe is also captured.

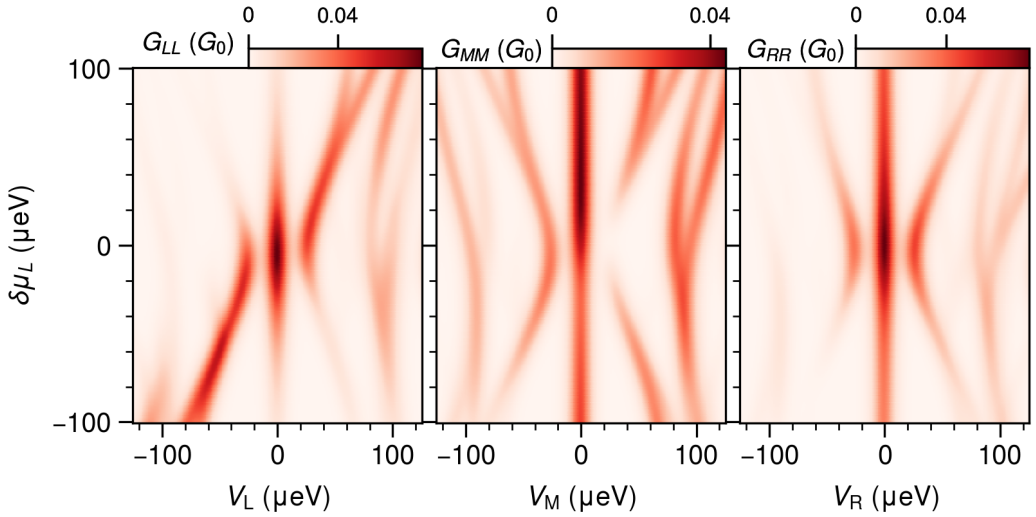

Figure 4.17: The simulated conductances when varying $\mu_L = \delta\mu$ and keeping $\mu_R = 0$. Each detuning is plotted on a different color scale. The simulated detunings for $\mu_R = \delta\mu$ while $\mu_L = 0$ look exactly the same but with G_{LL} and G_{RR} exchanged due to the symmetry of the left and right dot parameters in the numerical model.

To simulate the system in the numerical model we varied parameters at the interaction sweet spot corresponding to the spin-up orbital on both dots, to reproduce the features we observed in the experimental spectra.

The simulation parameters are held constant throughout all plots, and are all defined in terms of Δ_0 which is the induced gap in the proximitized region. The dots, each with charging energy $U = 10\Delta_0$ and g-factor $g = 12$, [5] couple to the ABS with $t = 0.8\Delta_0$ and $t_{so} = 0.4t$. The coupling to the leads is $\Gamma = 0.01\Delta_0$ from all sides. The simulation temperature is $T = 0.04\Delta_0$, corresponding to approximately 40 mK in our system. The ABS has a charging energy of $U = 0.5\Delta_0$, which reduces the energies of excitations living primarily on the ABS, as visible in the higher energy excitations in the simulation.

Comparing the exact conductance values between simulation and experimental data is inadvisable due to the difficulty of extracting the lead coupling terms Γ, realistic barriers having energy-dependent tunneling rates, and possible asymmetries between electron and hole transport across tunnel barriers.

However, we can observe that the strength of the ZBP in the middle probe depends on the

[5] Assymetric g-factors such as those measured in the experiment are difficult to implement in the simulation since it requires a much more involved optimization to find the sweet spot.

gate value. In the numerical model, this behavior of the middle ZBP conductance depends on the chemical potential of the ABS - a negative μ_{ABS} will lead to higher conductance when $\delta\mu < 0$, and a positive μ_{ABS} will lead to higher conductance when $\delta\mu > 0$.

We see a similar dependence of G_{MM} at the first excited state at the sweet spot. The positive energy state is not visible at $\mu_{ABS} > 0$, while the negative energy state is not visible at $\mu_{ABS} < 0$. In the simulated plots shown, we chose $\mu_{ABS} > 0$.

The detunings of the right dot and both dots simultaneously are seen below in Figure 4.18 and Figure 4.19 respectively. We see that the features that do not coexist in the simple QD-ABS-QD model, that is the higher energy excited state not being probeable and the ZBP conductance being higher for negative dot potential, do in the measurements.

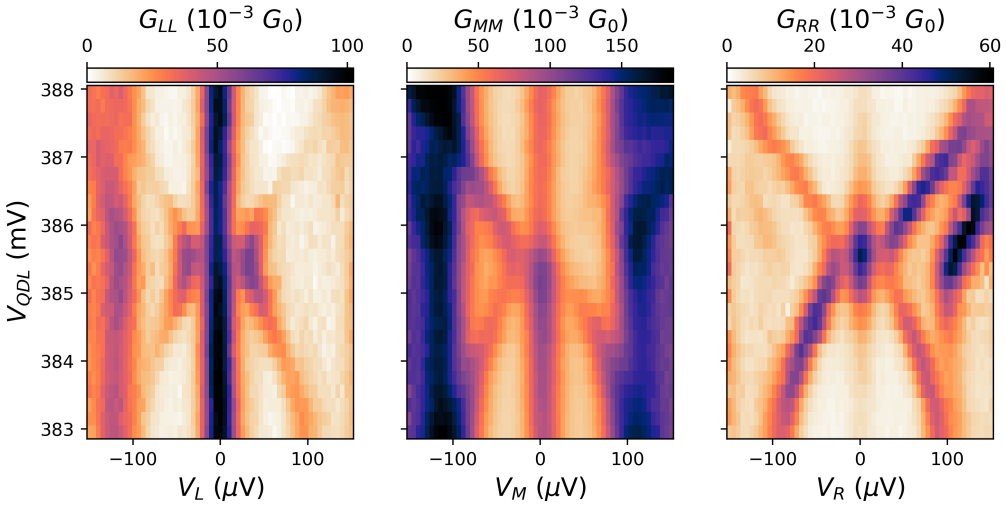

Figure 4.18: The local conductances when varying V_{QDR} around the sweet spot.

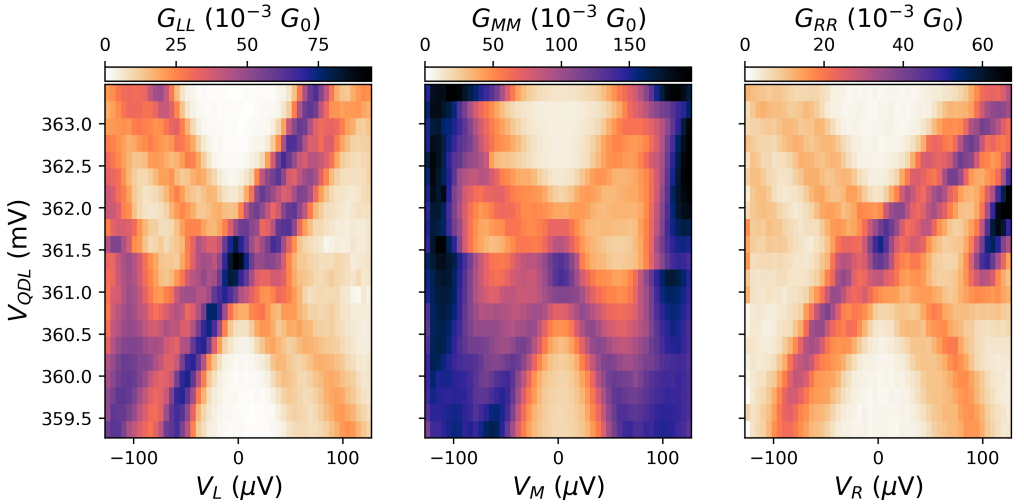

Figure 4.19: The local conductances when varying V_{QDL} and V_{QDR} around the sweet spot. Note that due to the lever arm asymmetry between the dots, $\delta V_{QDL} = \delta V_{QDR}$ does not mean that $\mu_L = \mu_R$. There seems to be a charge jump in the middle of the measurement which complicates the comparison between states at positive and negative $\delta\mu$.

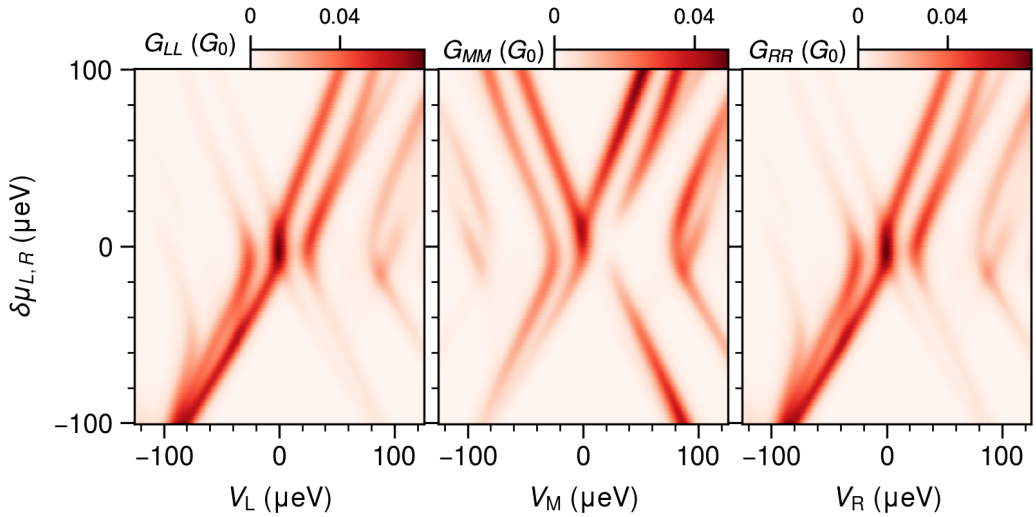

Figure 4.20: The simulated conductances when varying $\mu_L = \mu_R = \delta\mu$.

We see that the qualitative behavior of the central ZBP conductance as well as the excited states is explained by the simulations. The presence of several ABSs in the system likely complicates the behaviour of the PMM spectrum in our device.

4.6 Flux Tuning to the Majorana Sweet Spot

4.6.1 Tuning from CAR to ECT Regime through Flux

Control over the phase of the ABS should allow transitioning from CAR-dominated to ECT-dominated regimes and back by only varying the out-of-plane magnetic field [48].

The complicated flux-dependence of the ABS spectrum meant that this predicted tunability was not present at many ABS plunger gate values. We were able to find three ABS plunger regions where flux tunability was possible, and at those points we measured the dependence of ϕ_0 against V_{ABS}, where $\phi_0 \in (-\pi, \pi]$ is the phase at which CAR and ECT interaction are equal - i.e. the flux sweet spot.

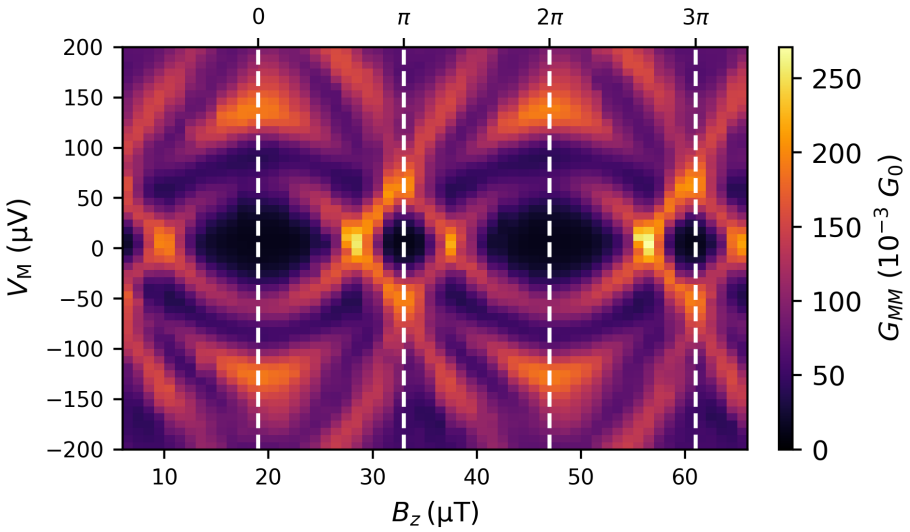

Figure 4.21: A typical example of a measurement done on the middle lead in the PMM regime, with the dots sufficiently off-resonance to ensure that they do not interact with the ABS or each other.

The middle lead in the setup allows us to conduct ABS spectroscopy without removing the dots left and right. Hence we can establish the phase of the ABS in the same gate regime as the one in which we measure the PMM excitation by doing spectroscopy through the middle with the dots in Coulomb blockade. An example is shown in Figure 4.21.

In Figure 4.22 we show charge stability diagrams measured at three different phase values. We emphasize that the only quantity changing is the phase $\Delta\phi$.

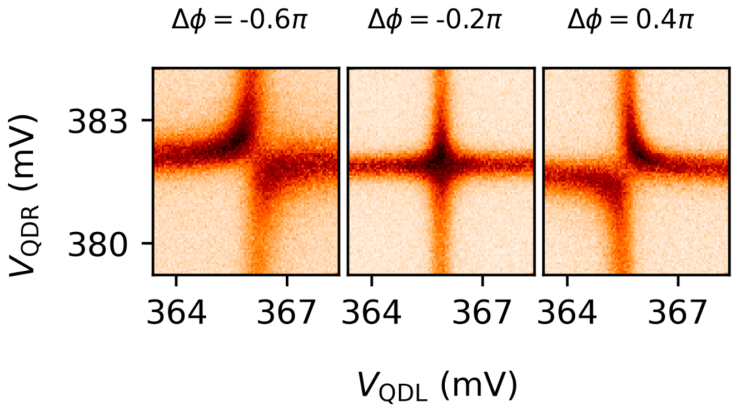

Figure 4.22: Charge stability diagrams for CAR-dominated (**left**), Majorana sweet spot (**middle**) and ECT-dominated (**right**) regimes. The plotted quantity is $\tilde{V}^L_{RF} \cdot \tilde{V}^R_{RF}$, where the tilde indicates normalization to a value between 0 and 1. This signal is essentially normalized correlated RF conductance.

In Figure 4.23 we show phase dependence at three different plunger values, illustrating how changing the phase from negative to positive π leads to a transition from CAR-dominated (diagonal anticrossing) to ECT-dominated (antidiagonal crossing). The sweet spot ϕ_0, the phase

difference at which $t = \Delta$, shifts by a quarter of a period across these three V_{ABS} values, from -0.5π to 0.1π. We also repeated these measurements for three flux periods to check that the expected periodic behavior endured.

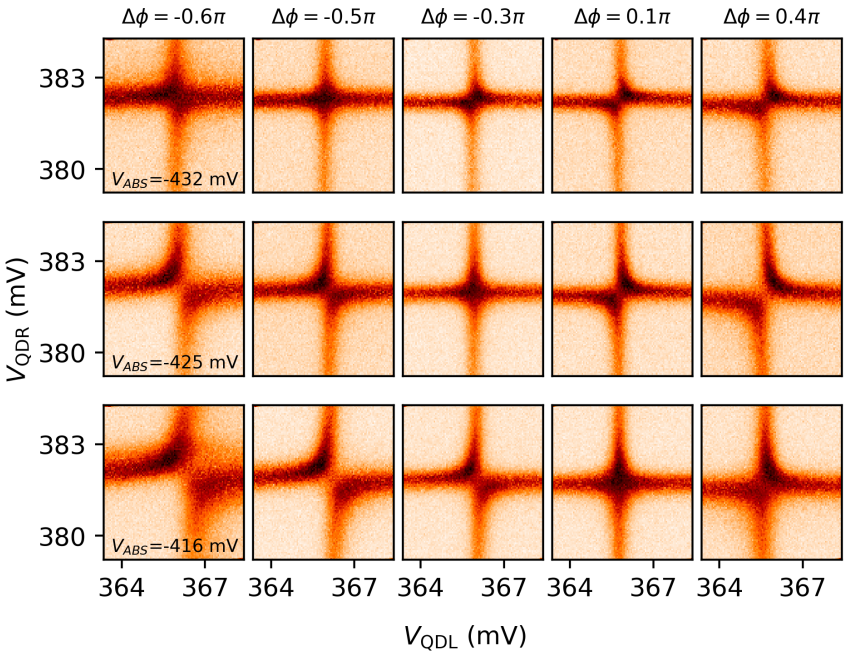

Figure 4.23: Charge stability diagram dependence on phase at three different plunger values. The plotted signal is correlated RF conductance as in Figure 4.22.

Another way to illustrate how ϕ_0 changes at different plunger gate values is by measuring the spectrum at every phase value, instead of measuring charge stability diagrams. In other words similar to how we may detune both quantum dot chemical potentials to see the splitting of the ZBP such as in subsection 4.4.3, or the ABS plunger gate such as in [50], we can also detune the flux. We expect to see a ZBP form at ϕ_0 and then split again, which we see for three different plunger values with different ϕ_0 values in Figure 4.24.

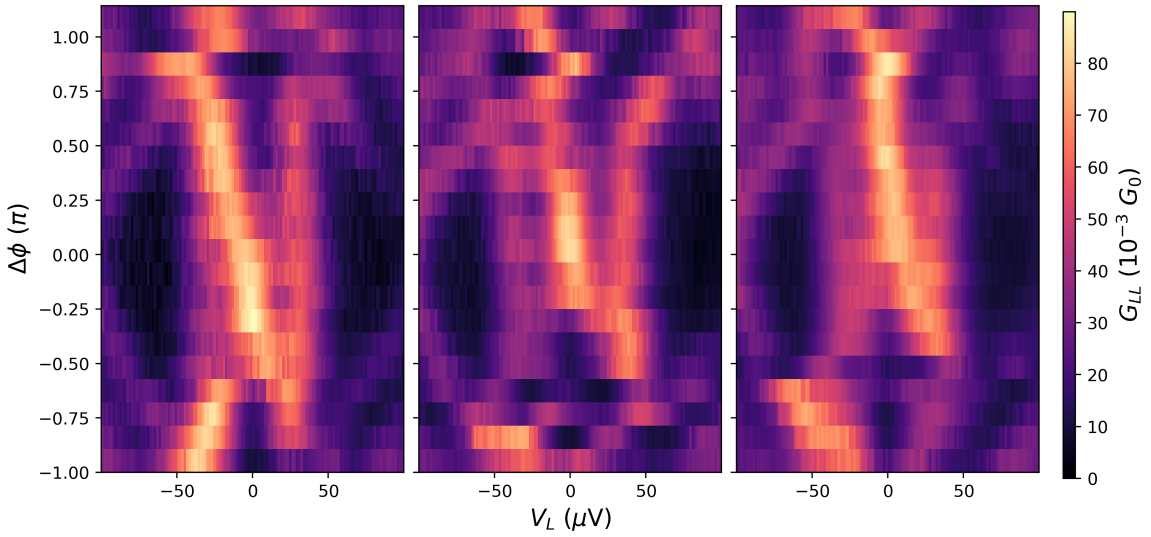

Figure 4.24: Flux Detunings. **Left.** $\phi_0 = -0.4\pi$ **Middle.** $\phi_0 = 0$ **Left.** $\phi_0 = 0.3\pi$

One complexity arises in this plot; as can be seen in Figure 4.23, the V_{QDL} and V_{QDR} values which correspond to $\mu = 0$ depend on the flux. This is because the ABS energy depends on its phase, and the proximitization of the dots depends on the ABS energy which in turn renormalizes the dot levels. In the flux detunings, we correct for this effect by auto-centering in between each measurement. While this works very well close to the sweet spot when the avoided crossing is strong or the quantum dot levels are strongly broadened by the ABS nearing $E_{ABS} = 0$ around π-phase the centering can be unreliable. This makes the flux detunings noisy and hard to read. Nevertheless, the ZBP can be seen to shift in flux space in response to the different ABS plunger values.

4.6.2 Flux sweet spot evolution over gatespace

Having seen that we can indeed tune through flux, it is interesting to observe the behavior of ϕ_0 for different plunger gate ranges.

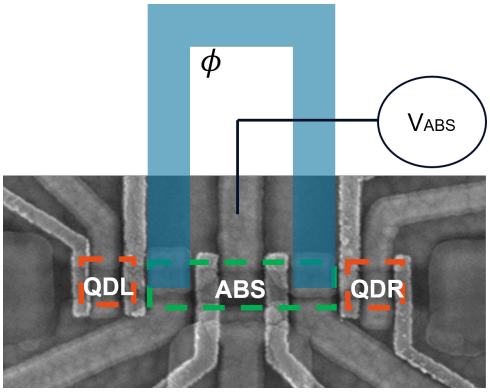

Figure 4.25: Schematic highlighting the two QDs together with the two ways we control the ABS: the flux loop and the plunger gate.

We observed that, besides when charge jumps occurred, the dependence of the flux sweet spot on the ABS plunger gate was smooth. For a single ABS without Zeeman splitting or spin-orbit coupling, one would expect two sweet spots across the entire range of $-\pi < \phi < \pi$, and that those sweet spots would be symmetric across 0 phase [48]. However, we only consistently measured one sweet spot in flux. We believe that the second sweet spot is hidden by the ABS energy decreasing so much at 0-phase that the description of the ABS as being a virtual coupler breaks down. Furthermore, the fact that we do not observe a sweet spot at $\phi = -\phi_0$ is likely due to the spin-orbit coupling.

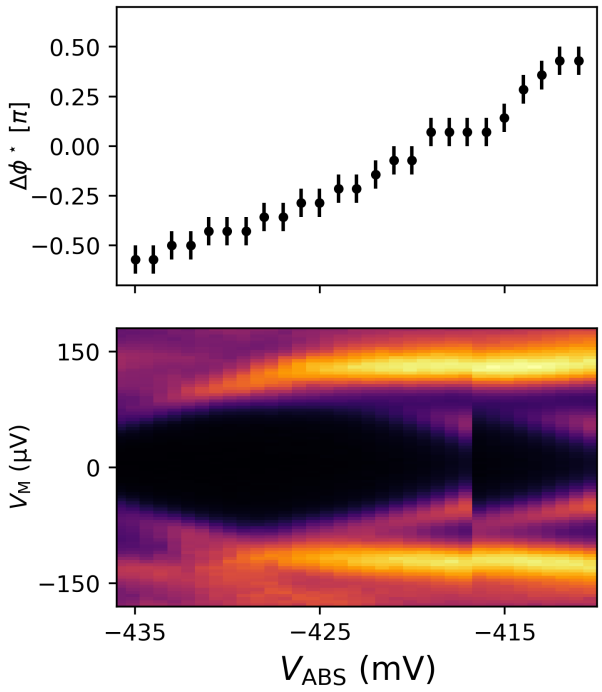

Figure 4.26: Top. ϕ_0 plotted against V_{ABS}. **Bottom.** The ABS spectrum, measured in G_{MM}. The error bars in the phase corresponding to the step size in the phase taken in between measuring CSDs.

At every sweet spot found above we measured the PMM spectrum from each of the normal leads with the gates tuned to $\mu_L = \mu_R = 0$. Figure 4.27 shows the spectra, plotted against the plunger gate value at which the PMM spectrum was measured after $t = \Delta$ was found using flux.

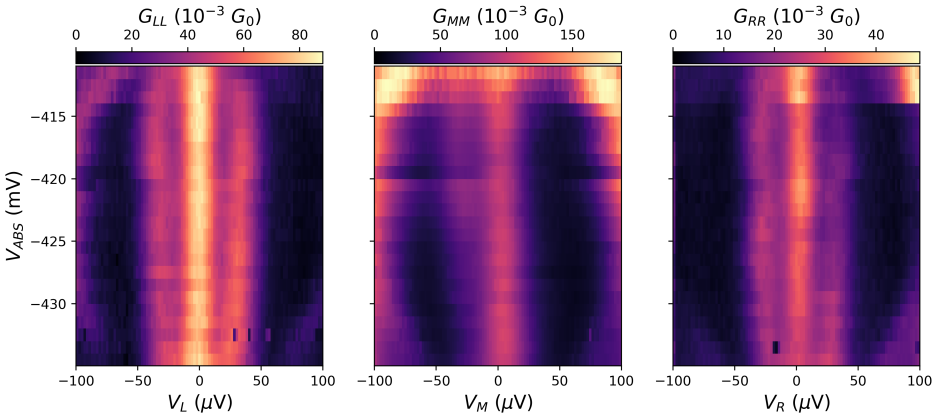

Figure 4.27: Spectra at the sweet spot from each lead. Note that this is not one single measurement, but a compilation of many measurements requiring tuning of the flux to the sweet spot at every ABS gate value. The phase value to be at the sweet spot for each V_{ABS} value can be read off from Figure 4.26.

Over the entire range, we can distinguish the PMM zero-bias peak and its excited states. The PMM gap does not vary strongly over the entire range, except when it decreases once the energy of the ABS decreases as $\phi_0(V_{ABS})$ gets to close to π-phase. In these measurements at least, it is not clear that there is any advantage in the additional control over flux in our system which is not present in a simpler minimal Kitaev chain.

We investigated ϕ_0 for two different separate ABS regions where tuning through flux was possible, where again we saw a smooth dependence of the flux sweet spot on the ABS plunger. These measurements were done during a different cooldown.

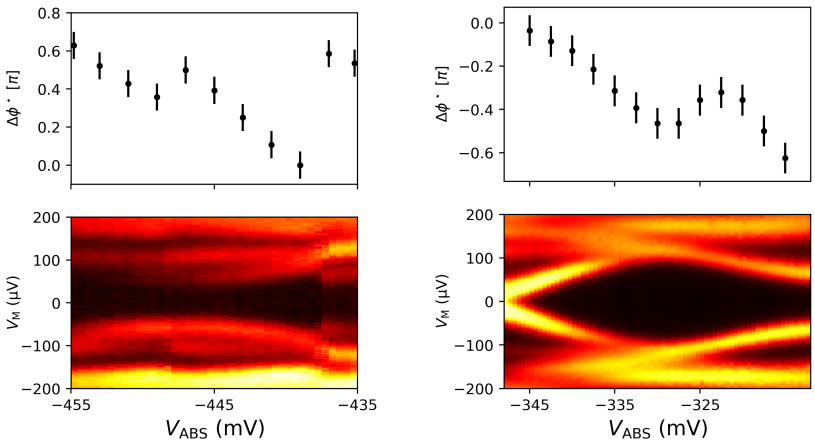

Figure 4.28: Top. ϕ_0 plotted against V_{ABS} for two different regions. **Bottom.** The ABS spectrum in the corresponding regions at phase $\phi = 0$. The quantity plotted is V_{RF}^M. The charge jumps present were reproducible.

4.7 Conclusion and Outlook

We have presented our work in demonstrating a Poor Man's Majorana system with a long ABS, probing the center of this PMM, and establishing flux control over the regime of this minimal Kitaev chain.

Simulations in the spinful QD-ABS-QD model predicted that tuning to a PMM at $\phi = \pi$ would lead to a more protected PMM with a greater excitation gap [48]. The presence of spin-orbit interaction and Zeeman splitting in the proximitized region as well as multiple separate ABSs with different transparencies and lever arms meant that systematic study of this predicted enhanced protection was impossible. Neither was a systematic relationship between the PMM gap and the phase of the ABS measured. However, we did find regimes where flux tuning was possible and the sweet spot in flux evolved smoothly as a function of ABS plunger gate.

Despite the difficulty of finding regimes where flux tuning allows for better PMM protection, the flux tunability may still prove to be interesting. For example, gate tuning suffers from its susceptibility to charge jumps in the gates and the electrostatic environment, which is not a problem when varying the out-of-plane B-field. Furthermore, provided that the dots are not too strongly coupled to the ABS, varying the flux has no impact on the quantum dot levels. This is due to the out-of-plane magnetic field being typically 4 orders of magnitude less than the Zeeman field.

Being able to probe the bulk of the PMM while the dots are still formed presents opportunities for further study in this device. The dependence of the central ZBP visibility on the coupling regime and the field, which is connected to the Majorana polarization [27], may be interesting as it is related to the spatial overlap of the Majorana wavefunctions. Moreover, simulations have suggested that probing the ABS when two quantum dots are coupled such that $t = \Delta$ at 0 field could show features that are not visible from either dot, potentially distinguishing this zero-bias peak from true spinless Majoranas. In the longer term, flux tuning may be more useful in other devices where the ABS spectrum is less crowded but which retain the superconductor-ABS coupling asymmetry.

Lastly, the long distance ($\approx$ 800 nm) over which we have demonstrated coherent Crossed Andreev reflection coupling between two QDs suggests that CAR could be used as a long-distance coupler for spin qubits based in quantum dots, as has already been theoretically explored [62]. The flux control we have demonstrated could additionally allow this coupler to be tunable allowing 2-qubit gates over a long range, although this would probably require a semiconductor where lattice symmetry is such that spin-orbit effects are not present.

Chapter 5

Phase-Control in a 3-Site Kitaev Chain

5.1 Motivation

Poor Man's Majorana zero modes have the potential to demonstrate control over non-Abelian physics and could be used to engineer a qubit by storing quantum information in the PMM parity [1]. However, a minimal Kitaev chain tuned to the PMM sweet spot is not protected from deviations in inter-QD couplings. [20]. True topological protection, i.e. an immunity to decoherence, is only achieved in the infinite site limit. In a finite system tuned to the sweet spot, any deviation of μ at all quantum dots, no matter how small, will lead to some finite wavefunction overlap of the Majoranas splitting them away from zero energy. While this sounds discouraging if we want to use this system for topological quantum computation, it turns out that this splitting is exponentially suppressed in the number of quantum dots in the chain [21]. This means that relatively few dots are required to observe highly robust non-Abelian physics. For example, it was found that 5 sites are enough to have a zero mode which is protected against significant fluctuations of all parameters t_n, Δ_n and μ_n [21].

A logical continuation after realizing a 2-site Kitaev chain is to add a third quantum dot. A chain with 3 sites has a bulk, a part of the system that is not located at the edge. As measured in section 4.5, Majorana bound states are located at the edges and can be probed from any part of the system in a 2-site chain. Hence 3 quantum dots is the minimal number of dots necessary to observe a gap in the excitation spectrum where there is no zero mode when the chain is tuned to the Majorana sweet spot [21]. The extra QD introduces a layer of complexity beyond the additional wiring and tuning required - in two dots the local phases in t and Δ may be taken out into an unobservable global phase through a gauge transformation on the orbitals [56]. In three dots there are three orbitals and four coupling terms, hence one of the phases cannot be gauged out. This leads to an effective phase ϕ, which without loss of generality we can consider to be contained in the Δ_2 coupling [56] :

$$t_1 = |t_1|, \quad t_2 = |t_2|, \quad \Delta_1 = |\Delta_1|, \quad \Delta_2 = |\Delta_2|e^{i\phi} \tag{5.1}$$

This local phase ϕ may be compensated for by applying a phase difference over the superconducting leads [21]. Doing so is crucial, because the Majorana excitation gap is expected to be

maximum at $\phi = 0$ where $E_{gap} = 2\min\{t_n\}_n$, and will vanish for $\phi = \pi$. A significant excitation gap E_{gap} is important since it determines the adiabatic time scale $\hbar/E_{gap}$ to show non-Abelian Majorana statistics in braiding experiments [4] and suppresses detrimental thermal effects which scale with $\exp(-E_{gap}/k_BT)$ [49].

Very recent work in a 3-site chain in an InAs nanowire confirmed the importance of phase control, showing how an oscillating phase with a period of 2 ns leads to measuring behavior that is well modeled by a phase averaged model, which takes into account an average over $\phi \in [0, 2\pi)$ [56]. This allowed the measurement of a zero bias peak with predicted 3-site protection. Yet although the Majorana excitations on the outer dots only overlap at exactly π-phase, the excitation gap at the sweet spot is nevertheless closed due to the phase averaging which effectively destroys the Majorana protection. This is why control over the superconducting phase difference is necessary to observe protected Majorana zero modes.

In this chapter, we will present measurements on a 3-site Kitaev chain with phase control. The phase difference between the two superconducting leads is controlled by a superconducting flux loop connecting them. We also present evidence that the bulk of the Kitaev chain is gapped when Majorana zero modes are measured on the outer dots, which is the first experimental observation of a bulk gap in Kitaev chains through tunneling spectroscopy.

5.2 Device Geometry

The device we used in these experiments is the same as the one in chapter 4 - although we now use all the gates, as highlighted in Figure 5.1.

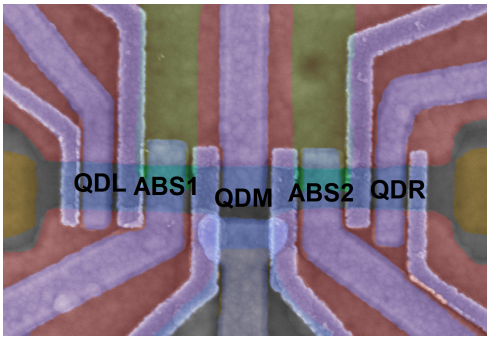

Figure 5.1: Top. SEM of the device, with the approximate regions where the QDs and ABSs are confined labeled.

An abstract diagram of the system is shown in Figure 5.2.

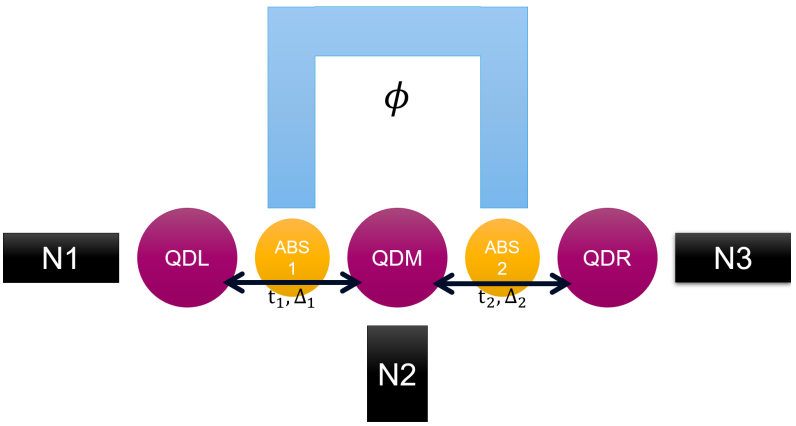

Figure 5.2: A schematic of the Kitaev-3 tuning, showing the three quantum dots, the two ABSs that mediate the coupling, the flux loop and the normal leads.

We define three quantum dots, each with tunable chemical potential through a plunger gate: V_{QDL}, V_{QDM}, and V_{QDR}. The outer dots are defined through two tunnel gates each, and the middle dot through three tunnel gates. We also have two plunger gates that allow us to tune the chemical potential of the hybrid regions: V_{ABS1} and V_{ABS2}, giving control over the inter-QD couplings.

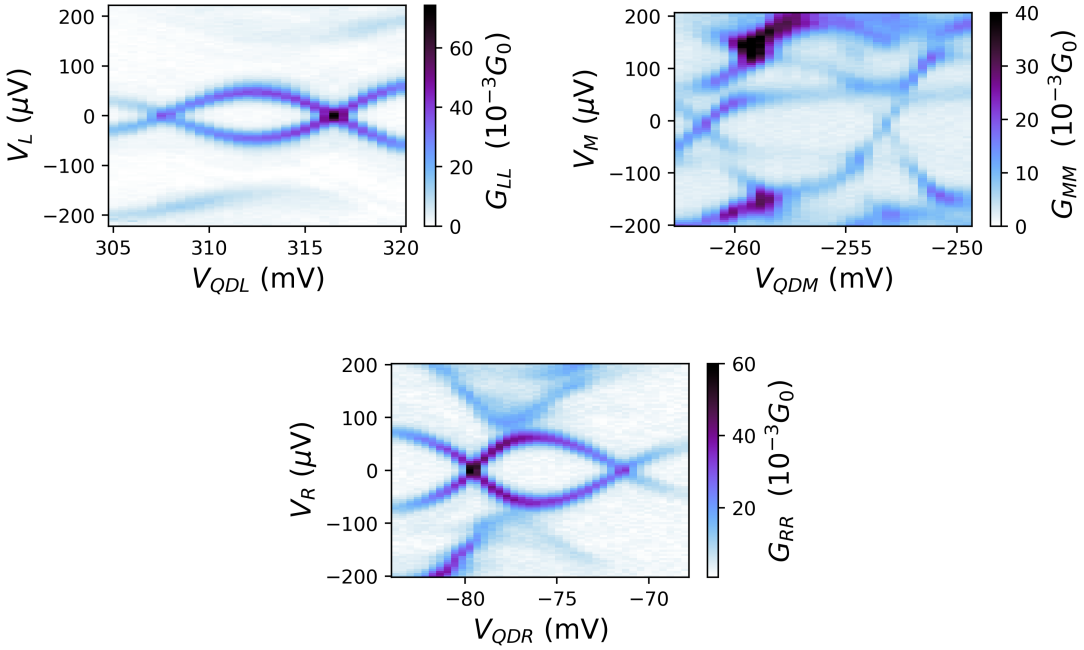

Figure 5.3: Sub-gap tunneling spectroscopy of the three quantum dots showing the evolution of the YSR state energies.

The YSR state spectra are shown in Figure 5.3. The middle quantum dot spectrum is more complicated since it is proximitized by two ABSs on both sides. The zero energy crossings are the fermionic sites that we will use to tune the 3-site Kitaev chain. Throughout this entire chapter, we spin-polarize the dots through an in-plane field of 220 mT.

5.3 Tuning and Characterizing Two 2-Site Chains

To tune a 3-site chain, two 2-site chains must be tuned first. This is done by moving one of the outer QDs off-resonance such that it no longer interacts with the others and then tuning the remaining two QDs. It is necessary to keep the gates defining the middle quantum dot at the same settings for both chains, which then allows us to bring all three dots on resonance to form a 3-site chain with the same inter-QD couplings as in the 2-site chains.

We start by showing that we can tune to the Majorana sweet spot for both 2-site chains while keeping the middle quantum dot's coupling to both its neighboring ABSs constant.

When tuning one chain, we place the QD which does not take part in Coulomb blockade through its plunger gate and characterize the PMM formed with the other two quantum dots. This is illustrated in Figure 5.4.

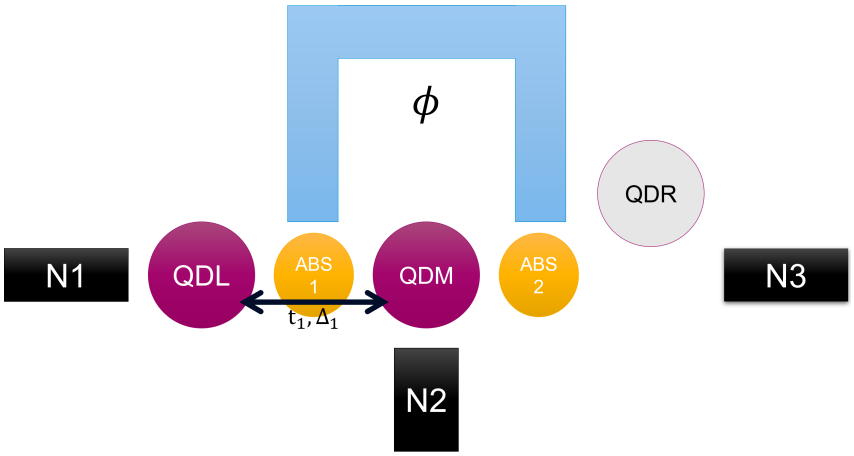

Figure 5.4: Schematic showing the system when tuning t_1 and Δ_1. When tuning t_2 and Δ_2, QDR is brought back on resonance and QDL is moved to Coulomb blockade instead.

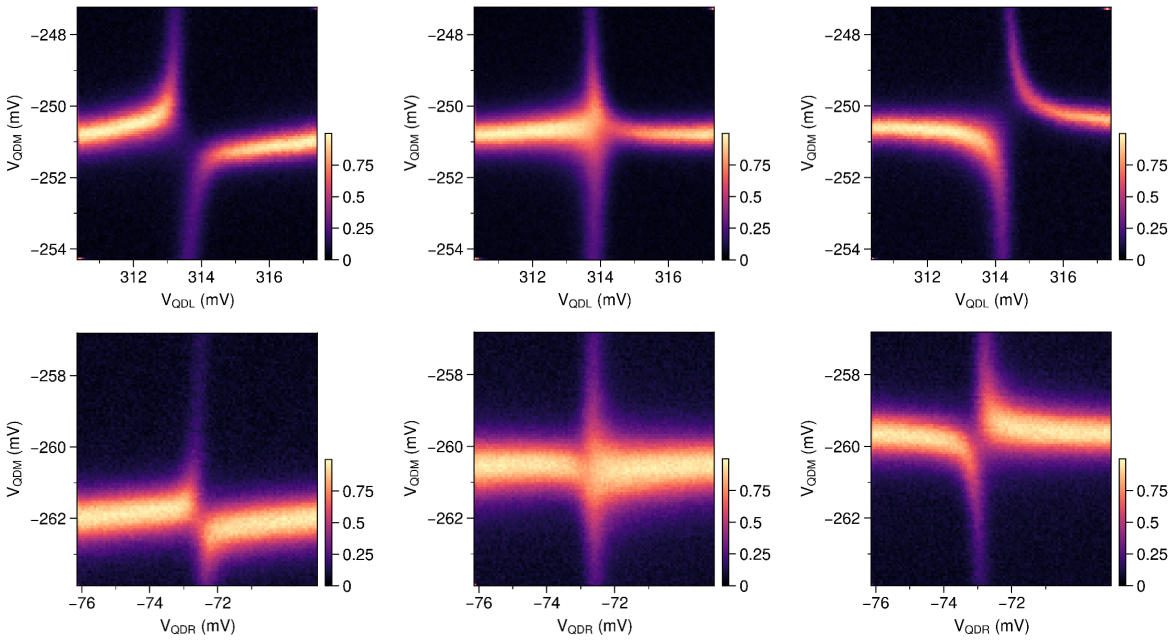

Figure 5.5: Normalized RF conductance measured at the middle lead for the QDL-QDM chain (**top**) and for the QDM-QDR chain (**bottom**). **Left.** $\Delta > t$. **Middle.** $\Delta = t$. **Right.** $\Delta < t$.

Figure 5.5 shows charge stability diagrams [1] at different values of the ABS1 (resp. ABS2) plunger gate, allowing us to infer the relative strengths of t_1 and Δ_1 (resp. t_2 and Δ_2). Measuring the spectrum at the sweet spot shows that we have PMM excitation gaps of $E^L_{gap} \approx 55\mu$eV and $E^R_{gap} \approx 50\mu$eV.

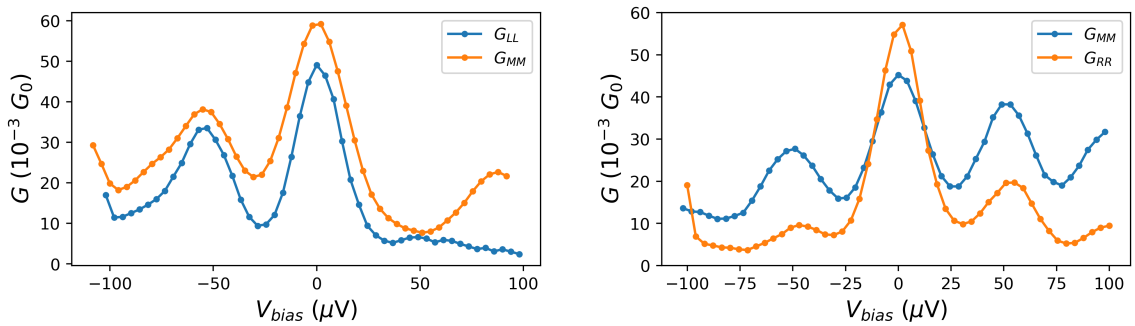

Figure 5.6: Spectra of the left and right 2-site Kitaev chains at their respective sweet spots.

We confirm that the sweet spots we see Figure 5.6 show the expected stability of the ZBP in detunings in the plots below. For each PMM, we show the spectrum while detuning each dot, and the spectrum while detuning both of them simultaneously.

[1] The V_{QDM} values do not perfectly align due to a gate jump, but the quantum dot orbital is the same - as evidenced later in Figures 5.7 and 5.8.

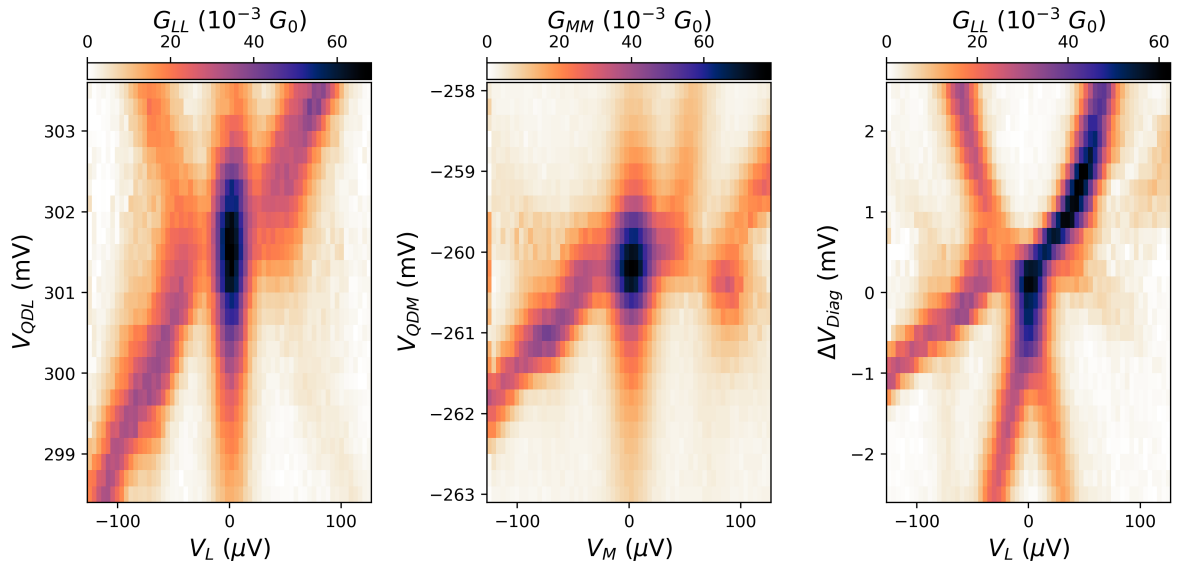

Figure 5.7: Spectrum of the left 2-site chain when detuning **(Left.)** QDL **(Middle.)** QDM and **(Right.)** QDL and QDM simultaneously.

The expected stability against single QD perturbations is visible, as well as the splitting of the ZBP once $\mu_L, \mu_M \neq 0$. The qualitative behavior of $G_L L$ when detuning the left dot - specifically the peak conductance and the smallest gap between the ZBP and the excited states not being at $\mu_L = 0$ - is typical of a PMM in the strong coupling regime [49, 50]. We see similar behavior in the detuning of QDR in Figure 5.8. The spectrum of the middle dot is likely more complicated to analyze due to its simultaneous hybridization with the left and right ABSs.

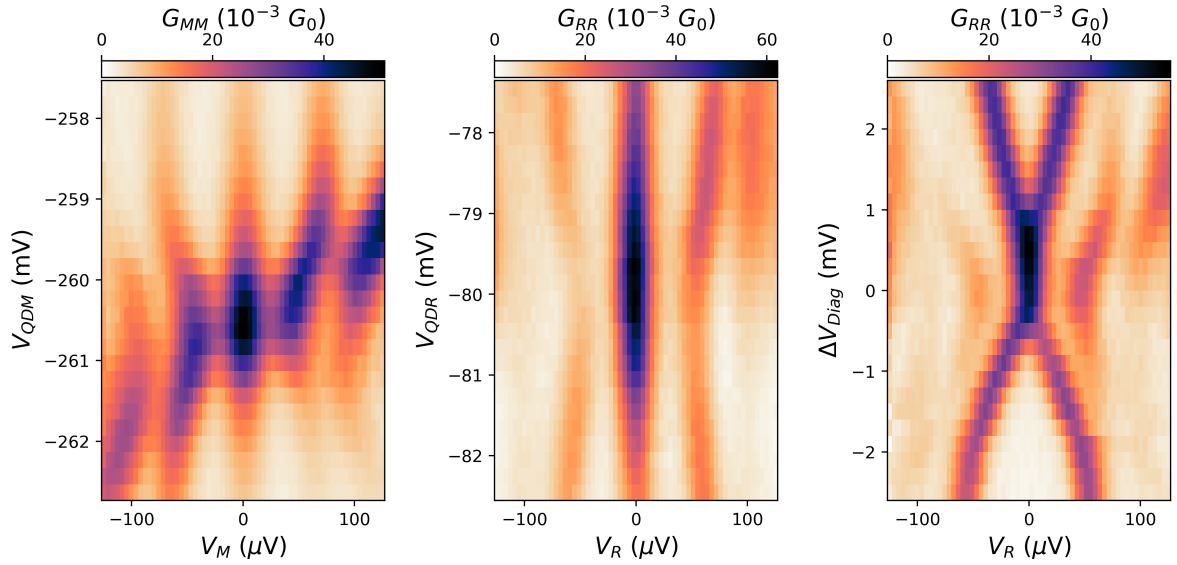

Figure 5.8: Spectrum of the right 2-site chain when detuning **(Left.)** QDM **(Middle.)** QDR and **(Right.)** QDM and QDR simultaneously.

5.4 Edge Modes and Bulk Gap

Now that we have tuned and characterized both 2-site chains, we combine them into one 3-site chain. The phase difference between the inter-QD couplings now comes into play. We will first show the phase-dependence of the Kitaev-3 spectrum and analyse its features, then discuss the value of the excitation gap before showing how the phase shift may be controlled by changing which sweet spot is chosen in the 2-site chains.

5.4.1 Phase Dependence of the 3-Site Chain

We use an effective 3-site model [2] - i.e. which doesn't explicitly consider the Andreev Bound states coupling the QDs - to simulate the conductance probed from the left, middle and outer leads. We first investigate the phase response at the Majorana sweet spot. The behavior seen in Figure 5.9 shows the stable zero bias peak appearing on the outer QDs, and only in the middle for $\phi = \pi, 3\pi$.

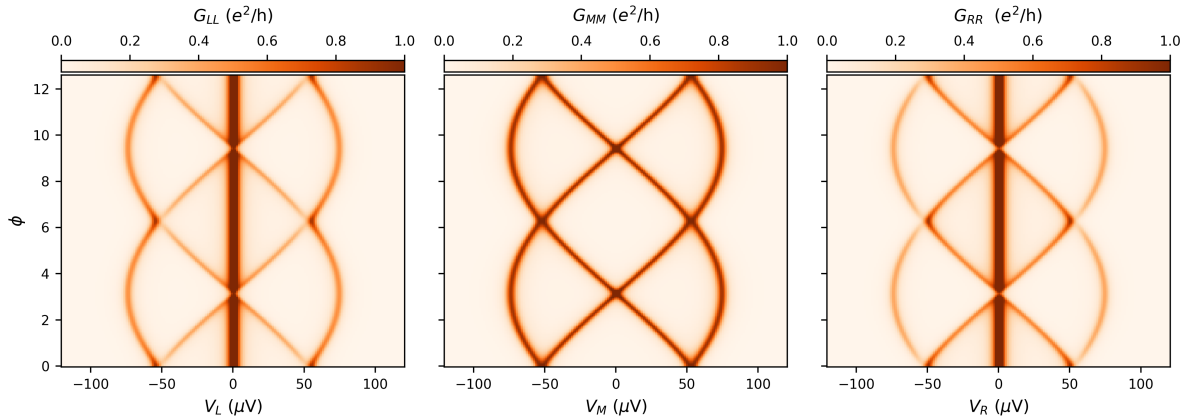

Figure 5.9: Simulated left, middle and right local conductances in response to phase for $\phi \in [0, 4\pi]$, for $t_1 + \Delta_1 = 55$ µeV and $t_2 + \Delta_2 = 50$ µeV.

This behavior is observed in the experimental data as well, plotted in Figure 5.10 below.

[2] We thank Dr. Chun-Xiao Liu for the simulation code.

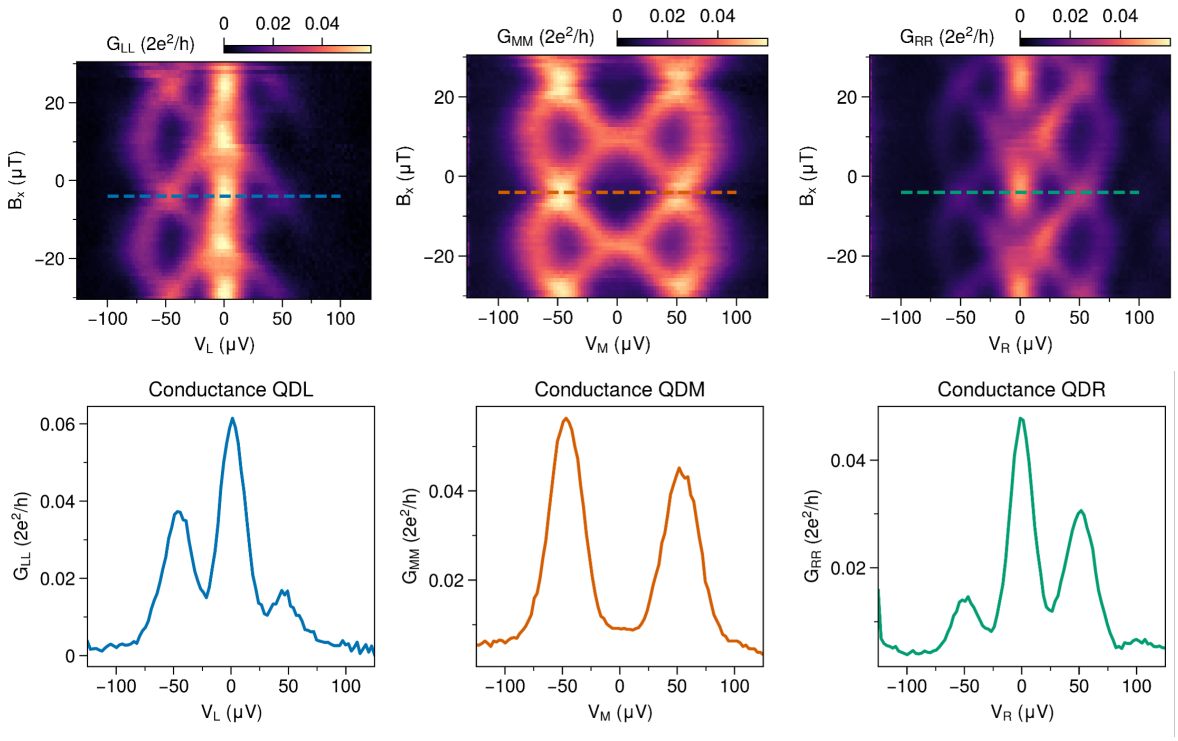

Figure 5.10: Top. Spectra in response to flux, with line cuts indicated. **Bottom.** Linecuts taken at 0 phase, where the excitation gap is maximal.

The line cuts show the spectrum where the excitation gap is largest. We measure $E_{gap} \approx 50$ μeV,which corresponds to the smallest gap of the individual PMMs. Note that $\phi = 0$ does not correspond to $B_x = 0\mu$T as a result of offsets in the out-of-plane B-field due to magnetic misalignment. Proper calibration to check whether zero phase difference between the superconducting leads translates to zero phase in the inter-QD couplings or whether some non-trivial ϕ_0 phase offset is present in the couplings themselves is needed, and is being done at the moment of writing this report.

Some other features are not captured by the idealized simulation in Figure 5.9. The peak visibility is not symmetric around zero bias. For example, on QDL the higher energy excited state has a lower conductance than the lower energy excited state, and the opposite is true for QDR. We attribute this mainly to charging energy effects from the ABS, which is not included in the simulation model but becomes relevant in the strongly coupled regime as the quantum dot wavefunction leaks into the ABS. As we saw in section 4.5, the chemical potential of the Andreev Bound state coupling two quantum dots can play a role in the visibility of excited states, and we noticed that which of the two sweet spots was selected for an ABS changed the conductance values in the three site chain as well. It is also possible that the tunnel barriers have an energy dependence or an asymmetry between electron and hole transport.

Furthermore the features generally qualitatively agree with the simulation, however around π-phase there is some splitting of the ZBP on QDR as well as a feature that resembles a poorly resolved avoided crossing in the middle. We attribute this to a flux-dependence of the coupling between QDM and QDR due to the middle QD's coupling to two ABSs simultaneously [63]. This is also observed when taking charge stability diagrams for the right 2-site chain as illustrated in Figure 5.11.

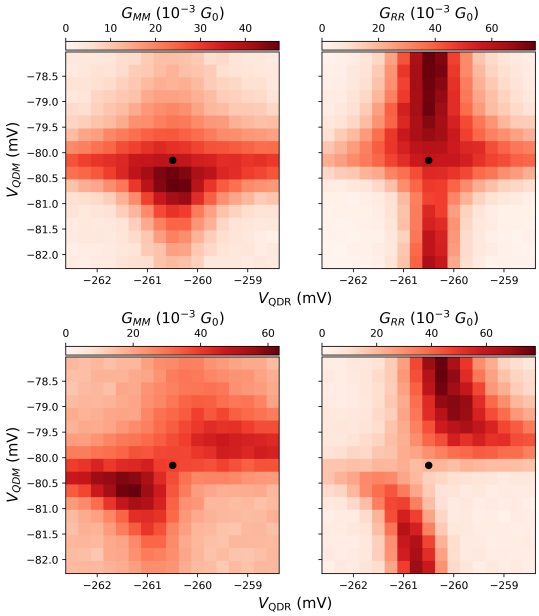

Figure 5.11: Charge stability diagram measured in differential conductance of the QDM-QDR PMM with QDL off-resonance. **Top.** $\phi = 0$. **Bottom.** $\phi = \pi$.

If we add this phase dependence to the effective 3-site simulation, the features observed in the experimental spectrum on the middle and right QD are qualitatively reproduced, which can be seen in Figure 5.12.

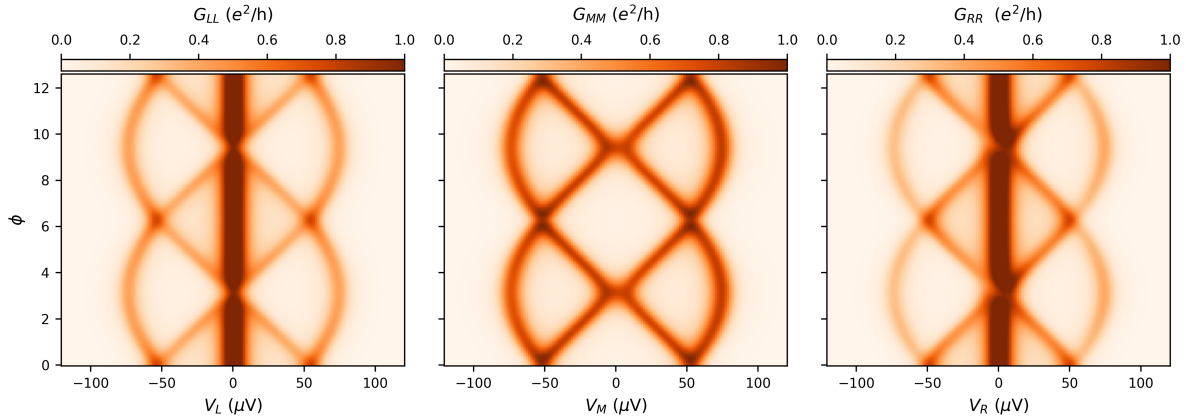

Figure 5.12: Simulated left, middle and right local conductances as in Figure 5.9, but with parameters varying smoothly from sweet spot at 0-phase to $t_2 - \Delta_2 = 10$ µeV and $\mu_2 = \mu_3 = 5$ µeV at π-phase.

5.4.2 Excitation Gap Extraction

To analyze the excitation gap we can model the level broadening in two separate ways. If the broadening is dominated by tunneling broadening we expect the level broadening to follow a Lorentzian distribution [37]:

$$f(V) = A\left[\frac{\gamma^2}{\gamma^2 - (V - V_0)}\right] \tag{5.2}$$

where A is the maximum amplitude, γ is the half-width at half-maximum , and V_0 the level energy.

If the broadening is dominated by thermal broadening, we use the thermal broadening function [37] :

$$f(V) = \frac{A}{\cosh^2\left(\frac{V-V_0}{\gamma}\right)} \tag{5.3}$$

Below we plot spectrum measurements at the 3-site Majorana sweet spot, fitted with both level broadening functions. The fits seem to suggest that the limitation on the resolution in our system is mostly due to thermal effects. In the fits, we enforce that the outer peaks are the same distance from the central peak, which is dictated by the system's particle-hole symmetry.

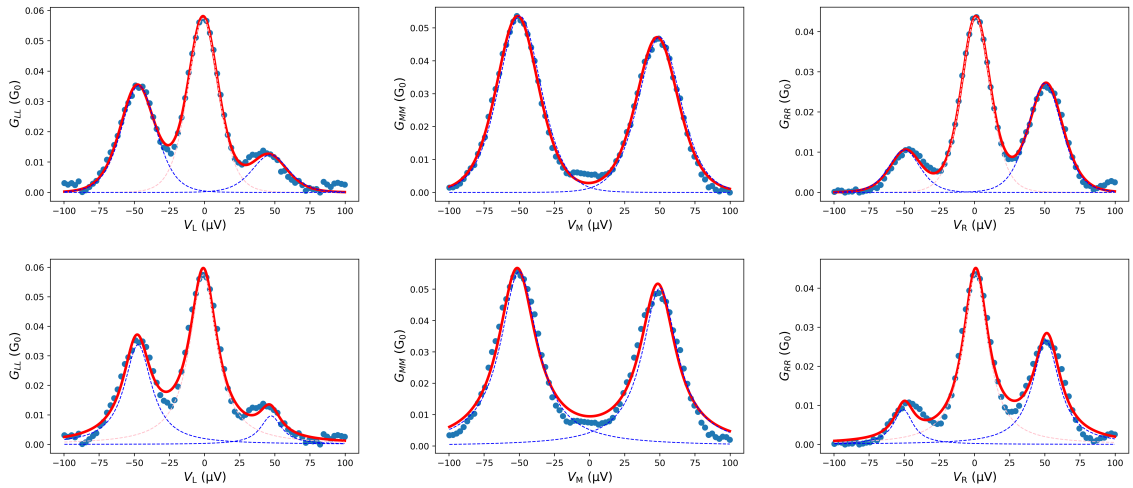

Figure 5.13: Spectrum measurements at the Majorana sweet spot fit with a thermal broadening function (**top**) and a Lorentzian distribution (**bottom**). The experimental data is plotted in blue scatter dots. Red dotted lines indicate the fitting of the central peak. Blue dotted lines indicate the fitting of the excited state peaks. The total fit is indicated by the thick red line.

Fitting only two peaks in the G_{MM} spectrum reproduces the data well. There is still some signal at zero bias in the middle spectrum. When three peaks are fit to the data like for G_{LL} and G_{RR}, we find that the conductance of the center peak has an upper bound of 3 mG_0, suggesting that we do not resolve a zero-bias peak on the central QD. This is significant, as it is a measurement of the Majorana delocalization. In the table below we compare the excitation gap for both fittings. We also show the values extracted from the PMM characterization, shown in Figure 5.6.

V_{gap} (µV)	Tunnel Broadening Fit	Temperature Broadening Fit
3-Site G_{LL}	47.3	46.8
3-Site G_{MM}	50.1	49.7
3-Site G_{RR}	50.8	50.0
Left PMM G_{MM}	57.5	57.1
Right PMM G_{MM}	51.8	51.4

We remark that the excitation gap in the 3-site chain is less than in both PMM regimes. However, the voltage values are not directly comparable, as in the PMM regime one of the leads is effectively completely removed from any transport process since its QD is put in Coulomb blockade, while in the 3-site regime, all 4 leads are active in the transport processes. For in-depth analysis, a four-terminal voltage divider correction should be carried out [52].

5.4.3 Pi Phase Shift

In the limit of a single time-reversal invariant (i.e. a negligible g-factor in the proximitized region) Andreev bound state which is weakly coupled to the outer dots, the rate of elastic cotunneling is proportional to $u^2 - v^2$ where u, v are the BCS coefficients of the ABS singlet ground state [30, 51]. When μ_{ABS} changes sign the ground state switches its charge character, and hence the sign of the ECT rate changes as well. In a 2-site chain, this sign flip is not observable as it is gauged away regardless. Once phase comes into play with more quantum dots added to the chain it should become observable.

Scaling up a Kitaev chain to even more dots would be very complicated if each pair of neighboring QDs required its own flux loop, with a corresponding flux bias line, to tune away from π-phase. If we could demonstrate that a π shift could be controlled through the choice of sweet spot, this opens the possibility for a phase-controlled long chain with only one global out-of-plane field.

Keeping all other settings the same, we tuned the left 2-site chain to the other sweet spot by varying V_{ABS1} which should flip the sign of $t_1\Delta_1$. The resulting PMM had an excitation gap of ≈40 µV. Despite this, the Kitaev-3 gap was 29.1 µV (extracted using thermal broadening fit). The phase dependence of this three-site chain is shown below and contrasted to the previous measurement.

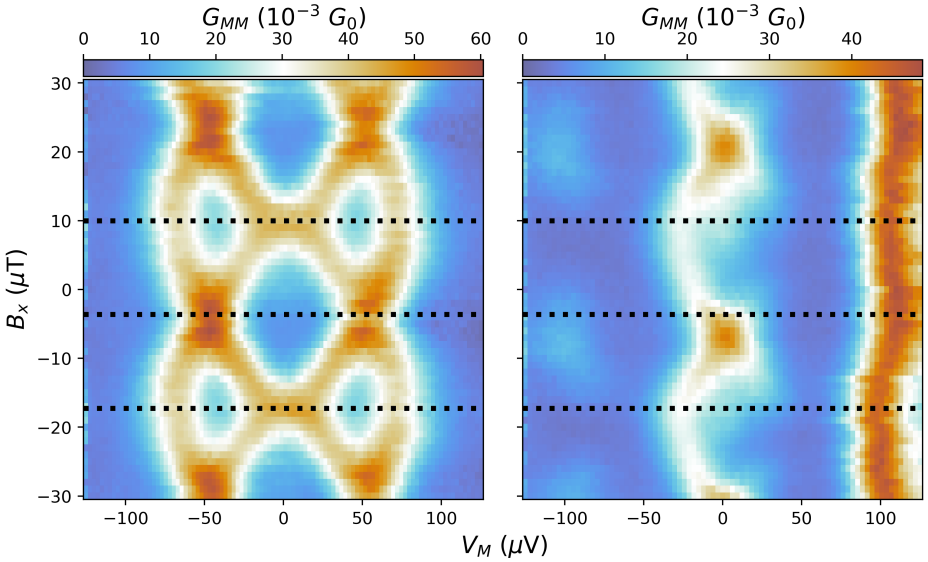

Figure 5.14: Phase dependence of the Kitaev-3 spectrum in the middle QD. Colormap chosen for strong contrast. The dotted lines are separated by $\pi/2$. **Left.** Data collected at sweet spot shown previously in Figure 5.10 **Right.** Data collected at the new sweet spot with different sign($t_1\Delta_1$).

The reduced excitation gap and decreased state visibility in the new sweet spot makes the comparison somewhat more complicated. However, π-phase can still be distinguished by the appearance of the zero bias peak. It seems that 0-phase in the right plot does not exactly correspond to π-phase in the left plot, and vice versa. The shift is approximately 0.8π.

An approximately 0.9π shift was measured in a regime that had less strong ABS-dot coupling and at a lower Zeeman field, as shown below in figure Figure 5.15.

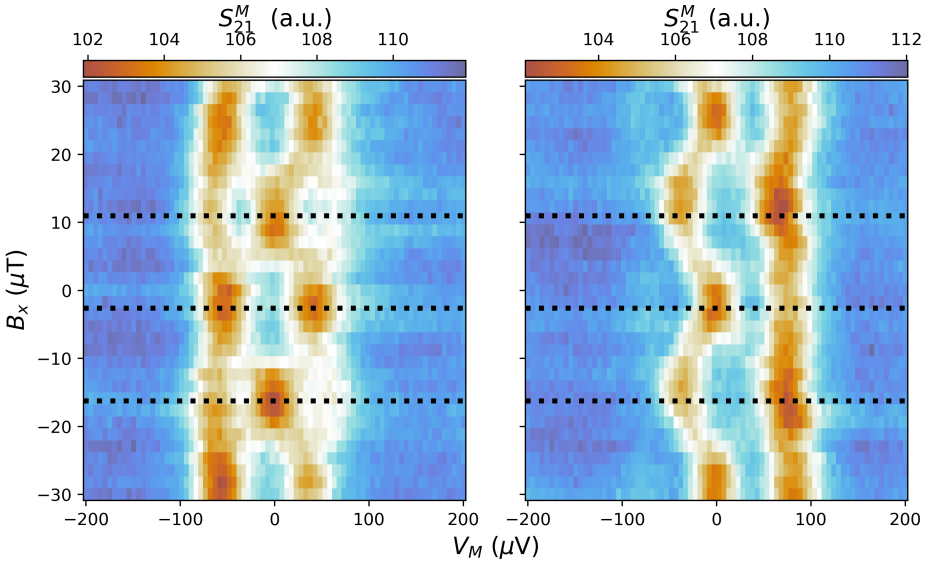

Figure 5.15: Phase dependence of the Kitaev-3 spectrum in the middle QD, measured in RF conductance. The data differs in the sign of $t_1\Delta_1$.

The hysteresis in this system - the difference between sweeping the magnetic field positively and negatively - is 2 μT. This is on the order of the variation from π-phase which we are seeing. Hence it is difficult to say we are certainly not measuring a π-shift. Different configurations with a smaller loop and hence larger period in phase would allow for more precise measurements of the phase shift - nanowire devices, in particular, are well suited for this.

There are several reasons why the phase shift could be not perfectly π. They include the spin-polarizing field not being perfectly perpendicular to the spin-orbit field, or orbital effects being non-negligible in the quantum dots or ABSs leading to some orbital interaction with the magnetic field. The presence of multiple channels is also a possibility. None of these parameters are easy to correct for. However, if the goal is to scale up to longer chains a near π-shift is also acceptable. It is only once the shift is $\pi/2$ or less that long chains are no longer expected to be tunable through only these gate-induced phase shifts and a global flux.

To conclusively claim we do not measure an exact π shift we should take more measurements with better quality sweet spots - i.e. more symmetric conductance values in the spectra and greater excitation gaps - for a wider range of parameters, and different signs in both $t_1\Delta_1$ and $t_2\Delta_2$. Furthermore, here we changed this sign only by tuning to a different sweet spot in the ABS chemical potential. It is also possible to change this sign by choosing a quantum dot level with a different spin [51].

5.5 Majorana Protection

The key motivation behind scaling up Kitaev chain lengths is to reach greater degrees of protection against environmental fluctuations. In this section, we confirm the theoretical protection that the Majorana zero modes should have against perturbations in μ in the quantum dots. When detuning the quantum dots the zero bias peaks should remain probable on the outer QDs, except if all are detuned from $\mu = 0$. Signatures of this 3-site protection to fluctuations in μ and $|t - \Delta|$ have already been measured [56], and in particular, the ZBP protection on the outer quantum dots has been studied. The novelty in the work presented here lies in the observation of the response of the excitation gap, and further in the measurement of the Majorana leakage into the central quantum dot.

The next measurements are all done at the large gap sweet spot shown on the left in Figure 5.14.

5.5.1 Detuning a Single Quantum Dot

We start by showing the behavior of the Majorana wavefunction as a response to $\mu_L \neq 0$. The response to $\mu_R \neq 0$ is qualitatively similar. Figure 5.16 shows the resulting spectra and gives an intuitive explanation through a diagram of the Hamiltonian in the Majorana basis.

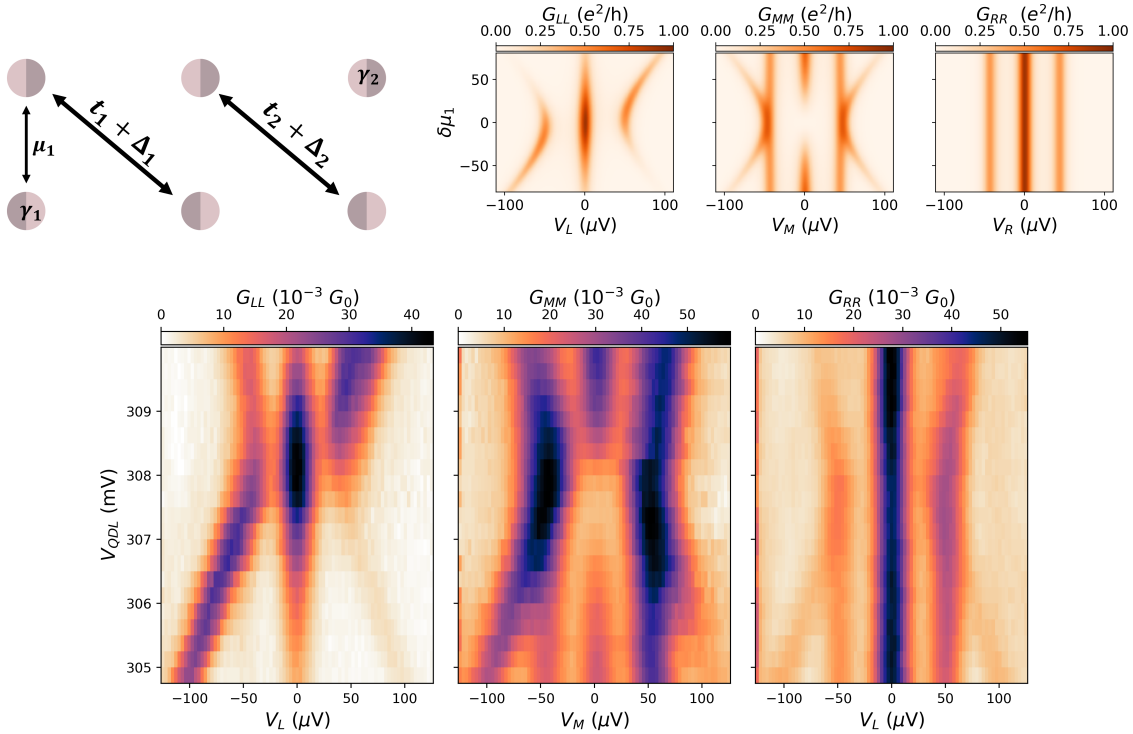

Figure 5.16: Top left. Diagram of the Kitaev-3 Hamiltonian detuned from the sweet spot by the left QD. **Top right.** Simulated conductance as a response to detuning the left dot. **Bottom.** Spectra measured from all leads while detuning V_{QDL}.

When detuning the left QD, the left Majorana leaks into the middle QD and we see a zero energy mode appear in the middle. The diagram illustrates this by showing the three coupled modes on the left, as well as the uncoupled mode on the right which remains at zero energy and entirely localized on the right QD throughout.

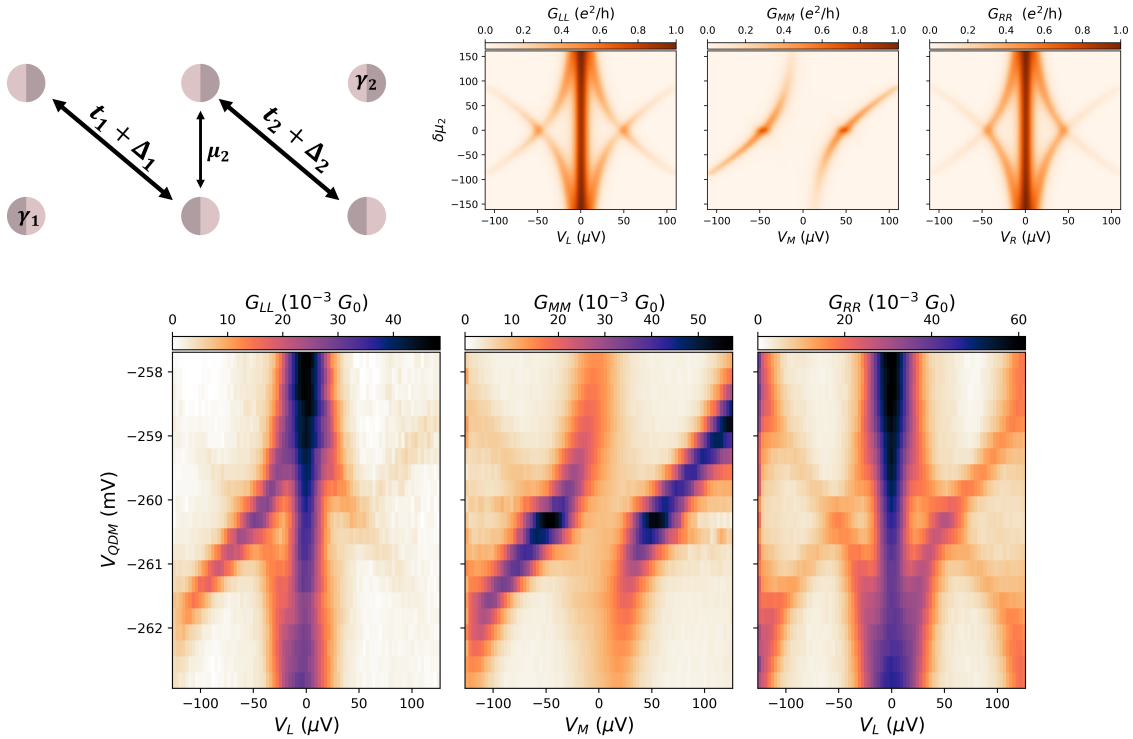

Figure 5.17: Top left. Diagram showing the detuning of the middle QD. **Top right.** Simulated conductance when varying the μ_2 arounnd the sweet spot. **Bottom** Spectra measured from all leads while detuning V_{QDM}.

In contrast, when detuning the central chemical potential the zero energy modes remain uncoupled to any other modes. We therefore expect to see different excitations in the middle quantum dot, but no zero energy mode. Figure 5.17 shows this behavior - we do not see any leakage of the zero energy mode in the middle probe.

5.5.2 Splitting the Majorana Zero Modes

It is only possible to split the zero energy modes by connecting them through either three chemical potential detunings or one detuning of a QD and one detuning of the correct inter-QD coupling. In this subsection, we show how the Majorana zero mode is split when doing the former.

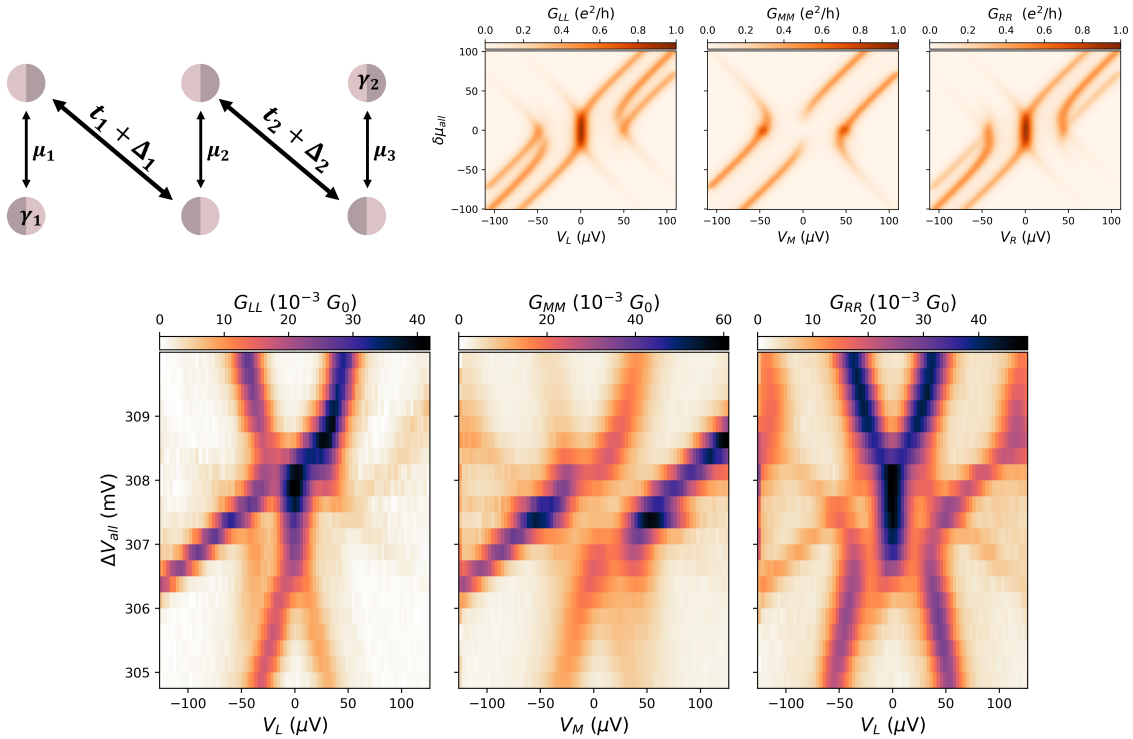

Figure 5.18: Top left. Diagram showing the interaction of the Majorana edge modes by activating all on-site coupling. **Top right.** Simulated conductance when all chemical potentials. **Bottom** Spectra measured from all leads during detuning.

The measurement shows the splitting of the MZMs. We can see them simultaneously leak into the middle site and split as they interact. Qualitatively, the correspondence of the simulated excited states is not very good, as in the experiment the QDs have different lever arms. The simulated data also does not consider the strong proximitization in all the QDs.

5.5.3 Non-Local Measurement of Excited States

In a measurement setup with two normal leads and a grounded superconductor, the non-local conductance indicates the charge of the probed excitation [53]. While this relationship is not so clear in our four-terminal measurement setup, we can still compare the non-local conductances to the theory given by the effective 3-site model. We show the simulated conductance and the measured conductance during the QDM detuning, the same experiment shown previously in Figure 5.17.

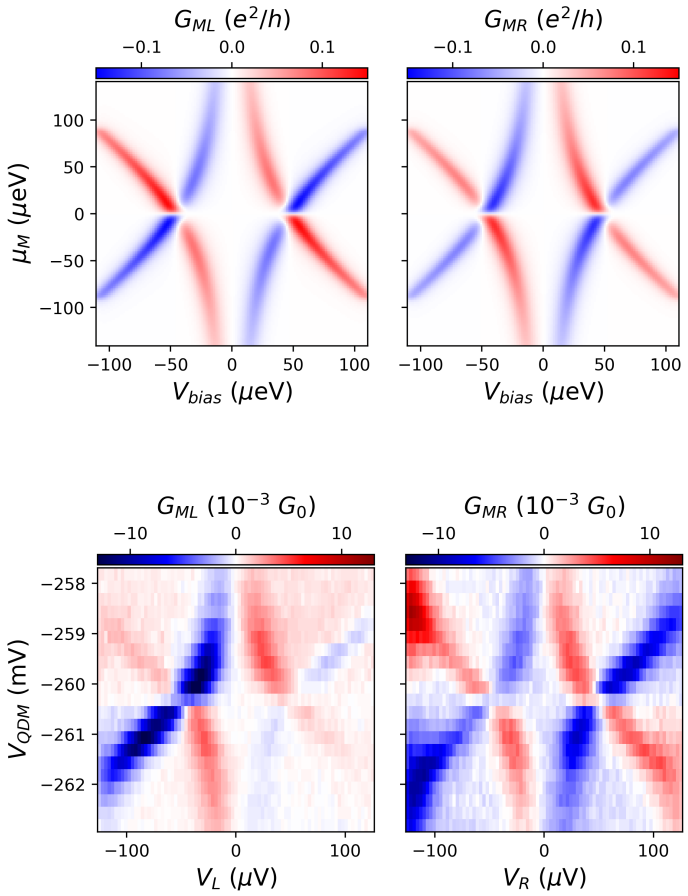

Figure 5.19: Simulated and experimental non-local conductance during spectroscopy on the middle QD.

The signs and behavior of the excited states, as well as the absence of a zero bias signal, are the same in both theory and experiment. However, some transport occurs that is not captured by the effective model - for example, the theory predicts no signal at all for G_{LM} or G_{LR}, however in the experiment we observe conductance values on the same order of magnitude as the non-local conductance which was predicted in Figure 5.19.

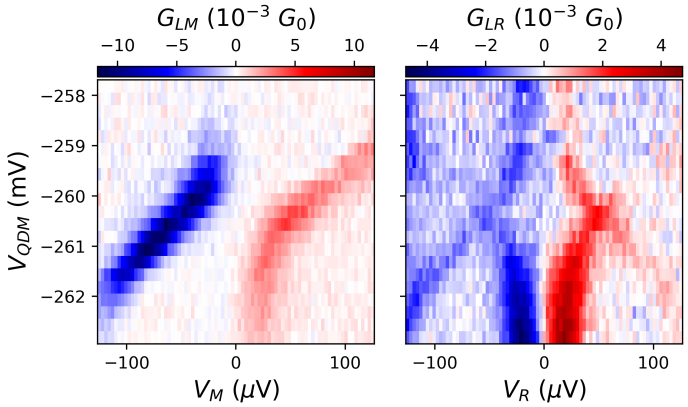

Figure 5.20: Experimental non-local conductance measured from the left as a response to the middle (**left**) and the right (**right**) bias. The effective 3-site model predicts no signal at all.

A full QD-ABS-QD-ABS-QD simulation does capture these conductances, indicating that they are consequences of the strong hybridization of the QDs with the ABSs in the system.

5.6 Conclusion and Outlook

In this chapter, we have demonstrated phase control through a flux loop in a 3-site QD based Kitaev chain, and have shown how it allows the observation of a gap in the bulk of the chain. These are important steps towards the usage of longer chains for MZMs in quantum information experiments.

For example, according to estimates in a 3-site nanowire device, a parity qubit encoded in 2-site chains has an expected dephasing time T_2^* of about 15 nanoseconds. A parity qubit with 3-site chains is expected to have a T_2^* of around 800 nanoseconds, a significant improvement [56]. Further scaling of more than an order of magnitude per dot is expected. Although these numbers strongly depend on the lever arms of the chemical potentials and on the inter-QD couplings, they illustrate the order of magnitude of improvements in quantum information experiments that a longer chain offers.

Some questions on the phase control are still open. For example, whether there is a phase shift at exactly 0 phase difference between the superconductors or whether the π-shift expected as described in subsection 5.4.3 is exactly π, unlike suggested in our initial measurements. Perhaps smaller loops, such as those used in nanowire devices with flux periods orders of magnitude larger than in the device presented here, can answer these questions. A voltage correction for four terminals may also be interesting, which would allow us to analyze the value of the excitation gap in the 3-site system more conclusively than subsection 5.4.2. It would also be interesting to explore if large gap sweet spots can be found consistently without the magnitude of the inter-QD couplings having phase dependence.

Lastly, more measurements on the 3-site chain protection are possible. Specifically comparing the stability of the ZBPs measured at 0-phase and π-phase is of interest. The stability of the

ZBPs against t and Δ perturbations, such as shown in [56], can also be interesting to investigate considering that the behavior on the central dot can also be measured in this device. A phase diagram measurement, where all μ values are varied against all t values for fixed Δ is realizable by varying all plunger gates versus ABS gates at zero bias while taking into account the relative lever arms.

Chapter 6

Conclusion

The main conclusions and outlook for the 2- and 3-site chains have already been stated in their respective chapters. We quickly summarize them here.

Phase control over the Andreev bound state in a 2-site Kitaev chain allows for tuning through flux. The flexibility this offers, as well as the potentially greater excitation gap it could offer, are promising for future PMM-based experiments. Phase control in the 3-site chain gives control over the excitation gap of the Majorana bound states at the sweet spot, and the Majorana protection these modes theoretically have has been confirmed. This represents a step towards longer chains that feature near-topological protection.

In the final chapter, we briefly summarize using ML techniques to tune a 2-site Kitaev chain, which has the potential to greatly simplify the experimental process when working with Kitaev chains and represents an interesting proof-of-concept for scaling them in large-scale systems.

Chapter 7

Outlook : Machine-Learning Assisted Tuning

TUNING the parameters μ, Δ and t in a Kitaev chain device is a significant part of the measurement process. In even the simplest qubit and braiding proposals, at least two Majorana sweet spots need to be tuned [1]. Not only is the initial tuning a time-intensive process, but charge jumps which can periodically occur require periodic retuning of the system. This delays experimental results and hampers potential scalability. Furthermore, tuning t and Δ while staying at $\mu = 0$ is well understood and can be done entirely through charge stability diagrams as shown in Theory section 2.4. This motivates the idea of using Machine Learning (ML) techniques to assist with Kitaev chain tuning, similar to how ML techniques can be used to allow for automated tuning of spin qubits [64]. For example, a Convolutional Neural Network (CNN) may be trained to recognize ECT-dominated, CAR-dominated, and sweet spot regimes [65].

In this section, we briefly describe how a CNN described in Ref. [65] was used to demonstrate the potential usefulness of ML in Kitaev chains. These measurements were performed in a nanowire 2-site Kitaev device, in the same as in Ref. [54] in a spin degenerate system. Given two QD orbitals left and right of a hybrid region, the ABS plunger gate V_{ABS} is varied. For a given V_{ABS} a CSD measurement is in both G_{RR} and G_{LL} taken, and a CNN receives their normalized product as an input before giving an estimate of :

$$f(V_{ABS}) = \frac{|t - \Delta|}{t + \Delta} \tag{7.1}$$

A simple 1D gradient descent algorithm is then used, which works as follows. A finite difference gradient is computed :

$$g_i = \frac{f(V_{ABS}^i) - f(V_{ABS}^{i-1})}{V_{ABS}^i - V_{ABS}^{i-1}} \tag{7.2}$$

To smoothen out noise, the gradient of the past 5 steps is averaged to give the gradient $\langle g \rangle$ used in the next step :

$$v^{n+1} = kv^n + (1-k)\langle g \rangle \tag{7.3}$$
$$V_{ABS}^{n+1} = V_{ABS}^n - \eta v^{n+1} \tag{7.4}$$

Where v is a velocity term used to keep track of previous tuning steps, η is a learning rate adapted to the energy scale of our device which can be optimally determined from the lever arm and the coupling of the QDs to the ABS, and $k \in [0, 1]$ is a momentum term that is used to tune how strongly the velocity from previous steps is conserved [66]. This gives the next plunger gate value V_{ABS}^{n+1}. Once the next gate value is chosen and that $f(V_{ABS})$ is not within a specific tolerance, a next CSD measurement is done, etc.

Initial implementations of this ML tuning suffered from the CNN recognizing very low interaction, i.e. small t and Δ, as sending $t - \Delta$ to 0 and hence being a satisfying sweet spot to tune to. To address this, we counted how many individual pixels in the measurement had an above-average conductance, and added a regularization term to the objective function :

$$f(V_{ABS}) = \frac{|t-\Delta|}{t+\Delta} + \left(\frac{N}{2N_<}\right)^3 \tag{7.5}$$

Where N is the total number of pixels and $N_<$ is how many had above-average conductance. This regularization term was tested through trial and error. The intuition is that as the system approaches weak interaction, $N_<$ becomes very small and the regularization term becomes large, causing the objective function to become too large to converge at undesirable weak interaction sweet spots.

This regularization in real measurements is shown in Figure 7.1 below. The iterations shown on the left used the unregularized objective function. All runs recognized that their initialization points were far away from the sweet spot, which is encouraging. Yet some got stuck in the V_{ABS} region which showed low interaction around 0.14 V (as indicated by the much noisier estimates in that region). This is fixed by the regularization procedure, which is shown in red in the right scatter plot.

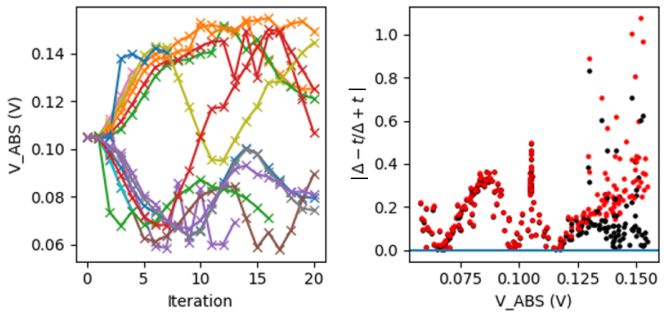

Figure 7.1: Left. Progression of V_{ABS} during iterations across several different runs. **Right.** The objective functions, with (red) and without (black) the regularizing term, as a function of V_{ABS}.

Using the regularizer therefore reduced the number of false positives that the gradient descent algorithm converged to. In the following figures we show an example of a series of remarkably successful test runs.

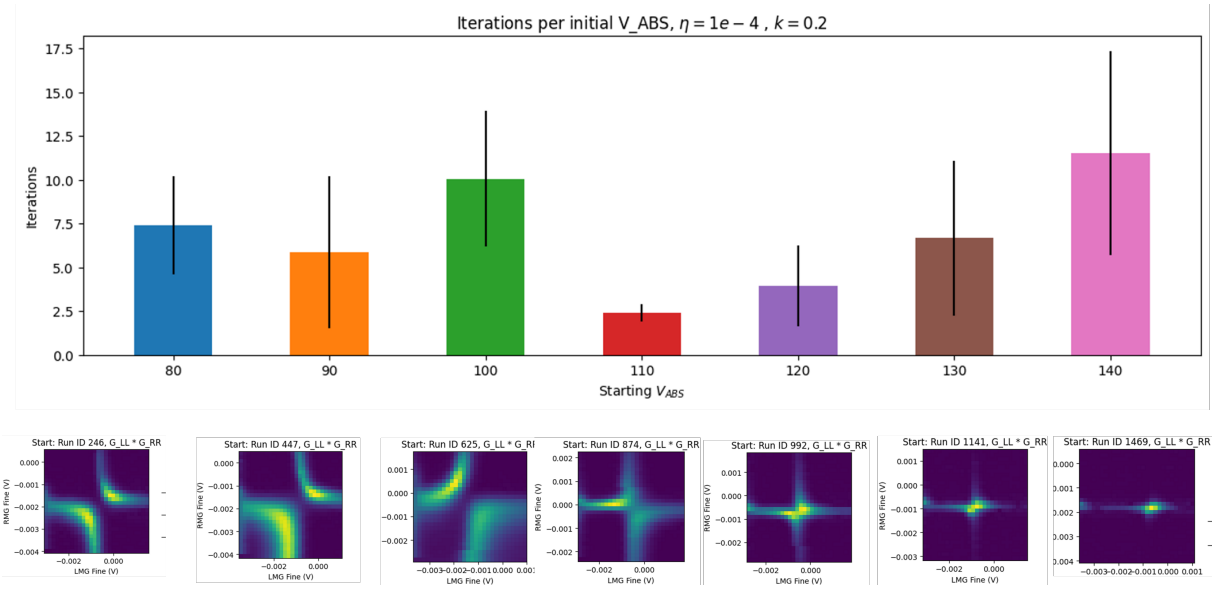

Figure 7.2: Top. The average number of iterations until convergence and standard deviation for seven different initialization points across the V_{ABS} range shown in Figure 7.1. **Bottom.** CSDs plotted in $G_{RR} \cdot G_{LL}$ at each of the initialization points.

Figure 7.2 shows how many iterations were needed on average to find a sweet spot - the average total time of these iterations was 45 minutes each. Unsurprisingly, the closer one starts to a sweet spot the fewer iterations are necessary. Note how the starting points at 130 mV and 140 mV show very little interaction. Figure 7.3 shows the final values of the sweet spot finding algorithm, with a convergence rate of 96.1 % within 15 iterations. The CSDs at the found V_{ABS} sweet spots are underneath the histogram.

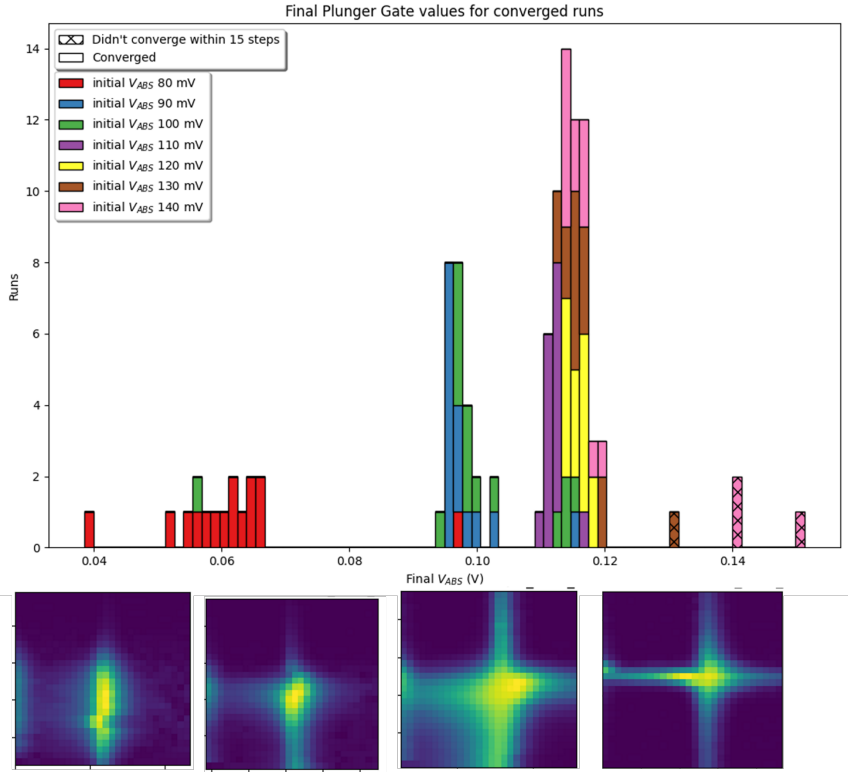

Figure 7.3: Top. V_{ABS} values labeled as estimated sweet spots. Unconverged runs after 15 iterations are labeled. **Bottom.** CSDs plotted in $G_{RR} \cdot G_{LL}$ at 40 mV, 60 mV, 100 mV and 115 mV which correspond to the found sweet spots.

The values to which the tuning algorithm converges indeed correspond to sweet spots. The two on the left are of lower quality due to the ABS coming down in energy at those values. Given a few iterations of this algorithm at different starting points, it could converge to several different results and allow an experimentalist to quickly select the most promising parameters. Hence although at its current stage the algorithm is not yet ready for fully automated tuning, it can already be used in experiments and save a significant amount of time. Furthermore, similar to how the tuning of double quantum dots has been done for spin qubits [64] this is a promising first proof of concept for the automated tuning of Kitaev chains.

Appendix A

Non-local Conductance in the Middle Lead in the 2-site Kitaev Chain

In measurements with two normal leads and one grounded superconducting lead, the non-local conductance gives an indication of the BCS charge that is being excited, which is worked out in detail in [53]. In particular, for two leads L and R the signal at zero bias $G_{RL} = G_{LR}$ is directly proportional to $q_L q_R$, up to some prefactors depending on temperature and tunneling rates, where $q_{L,R}$ are the BCS charges of the excitations to which the leads couple. For a Majorana zero mode, the condition $\gamma = \gamma^\dagger$ implies that it must have a BCS charge of 0, hence in a setup with two normal leads non-local conductance will always vanish at the Majorana sweet spot.

We are unaware of any similar analytic results for the non-local response in a system with three normal leads and one grounded superconducting lead such as in ours. Since the working out in [53] relies on the conservation of probability current which is broken once a third lead to which electrons or holes can drain is introduced, we cannot directly apply their conclusions to our system.

Despite these caveats, our measurements did show that non-local conductance, even in this more complicated setup, vanishes at the sweet spot. Figures A.1 and A.2 show examples.

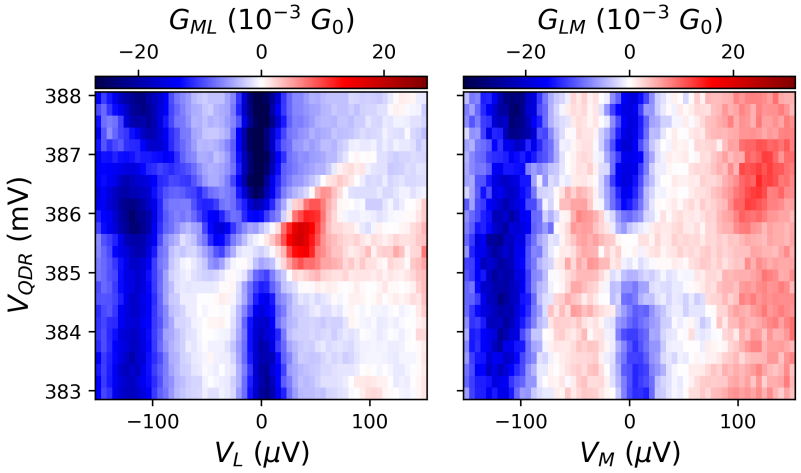

Figure A.1: G_{ML} and G_{LM} measured when detuning the right dot.

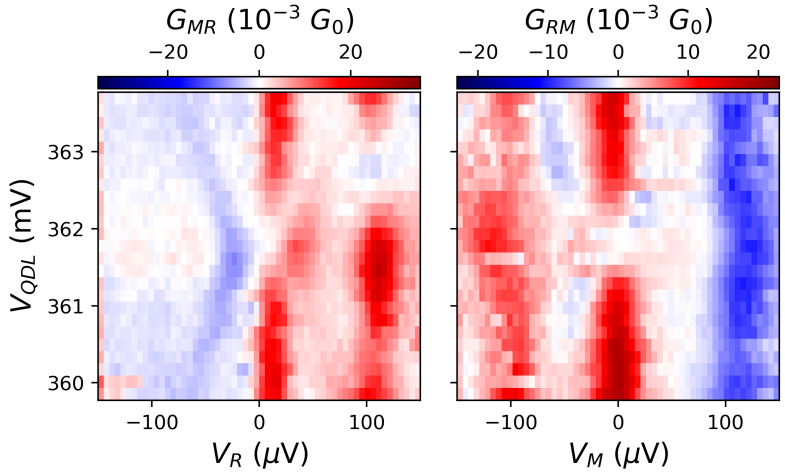

Figure A.2: G_{MR} and G_{RM} measured when detuning the left dot.

These measurements have a worse signal-to-noise ratio than the local measurements since the nonlocal response is often on the order of 10 mG_0. Note that in the data in these figures a global background conductance was subtracted - in the raw measured data a background signal was observed likely due to the tunnel barrier on the middle lead not being pinched off enough to fully be in the tunneling regime.

Acknowledgements

Firstly, I want to thank **Srijit** for allowing me to carry out a Master's project in your lab and for creating an environment which is both fun to work in and also highly productive. Thank you **Bas** and **Ivan** for your guidance ! It was a lot of work for you to take on two students at the same time, but you remained patient and helpful throughout. A special thanks also to **David**, you were a lot of fun to work with on the ML project.

I want to deeply thank the entire **2D topo group** for being both welcoming and an interesting group of people. I'm equally grateful to the wider **Kitaev team** for the same reason, and I'm looking forward to coming back and being part of your research efforts as a PhD student.

A special thanks to my fellow QuRe master students (**Tijl, Eoin, Praveen,Thomas, Florian**). There is a special bond that is formed when a group of students goes through the same collective impostor syndrome, and it was a pleasure to experience it with you.

Last but not least, *merci* to my parents and grandparents for their support during my studies.

Bibliography

[1] Athanasios Tsintzis et al. *Roadmap towards Majorana qubits and nonabelian physics in quantum dot-based minimal Kitaev chains*. June 28, 2023. arXiv: 2306.16289[cond-mat]. URL: http://arxiv.org/abs/2306.16289 (visited on 03/03/2024).

[2] D. Michel Pino, Rubén Seoane Souto, and Ramón Aguado. *Minimal Kitaev-transmon qubit based on double quantum dots*. 2023. arXiv: 2309.12313 [cond-mat.mes-hall].

[3] Ville Lahtinen and Jiannis K. Pachos. "A Short Introduction to Topological Quantum Computation". In: *SciPost Physics* 3.3 (Sept. 9, 2017), p. 021. ISSN: 2542-4653. DOI: 10.21468/SciPostPhys.3.3.021. arXiv: 1705.04103[cond-mat,physics:quant-ph]. URL: http://arxiv.org/abs/1705.04103 (visited on 11/27/2023).

[4] David Aasen et al. "Milestones Toward Majorana-Based Quantum Computing". In: *Physical Review X* 6.3 (Aug. 2016). ISSN: 2160-3308. DOI: 10.1103/physrevx.6.031016. URL: http://dx.doi.org/10.1103/PhysRevX.6.031016.

[5] A.Yu. Kitaev. "Fault-tolerant quantum computation by anyons". In: *Annals of Physics* 303.1 (Jan. 2003), pp. 2–30. ISSN: 0003-4916. DOI: 10.1016/s0003-4916(02)00018-0. URL: http://dx.doi.org/10.1016/S0003-4916(02)00018-0.

[6] Chetan Nayak et al. "Non-Abelian Anyons and Topological Quantum Computation". In: *Reviews of Modern Physics* 80.3 (Sept. 12, 2008), pp. 1083–1159. ISSN: 0034-6861, 1539-0756. DOI: 10.1103/RevModPhys.80.1083. arXiv: 0707.1889[cond-mat]. URL: http://arxiv.org/abs/0707.1889 (visited on 11/27/2023).

[7] Sumathi Rao. *Introduction to abelian and non-abelian anyons*. 2016. arXiv: 1610.09260 [cond-mat.mes-hall].

[8] Ali Yazdani et al. "Hunting for Majoranas". In: *Science* 380.6651 (June 2023). ISSN: 1095-9203. DOI: 10.1126/science.ade0850. URL: http://dx.doi.org/10.1126/science.ade0850.

[9] Alexei Kitaev. "Unpaired Majorana fermions in quantum wires". In: *Physics-Uspekhi* 44.10 (Oct. 1, 2001), pp. 131–136. ISSN: 1468-4780. DOI: 10.1070/1063-7869/44/10S/S29. arXiv: cond-mat/0010440. URL: http://arxiv.org/abs/cond-mat/0010440 (visited on 10/23/2023).

[10] Yuval Oreg, Gil Refael, and Felix von Oppen. "Helical Liquids and Majorana Bound States in Quantum Wires". In: *Phys. Rev. Lett.* 105 (17 Oct. 2010), p. 177002. DOI: 10.1103/PhysRevLett.105.177002. URL: https://link.aps.org/doi/10.1103/PhysRevLett.105.177002.

[11] R. M. Lutchyn et al. "Majorana zero modes in superconductor–semiconductor heterostructures". In: *Nature Reviews Materials* 3.5 (May 2018), pp. 52–68. ISSN: 2058-8437. DOI: 10.1038/s41578-018-0003-1. URL: http://dx.doi.org/10.1038/s41578-018-0003-1.

[12] Pasquale Marra. "Majorana nanowires for topological quantum computation". In: *Journal of Applied Physics* 132.23 (Dec. 2022). ISSN: 1089-7550. DOI: 10.1063/5.0102999. URL: http://dx.doi.org/10.1063/5.0102999.

[13] Nick van Loo. "Shadow-wall lithography as a novel approach to Majorana devices". PhD thesis. 2023.

[14] V. Mourik et al. "Signatures of Majorana Fermions in Hybrid Superconductor-Semiconductor Nanowire Devices". In: *Science* 336.6084 (2012), pp. 1003–1007. DOI: 10.1126/science.1222360. eprint: https://www.science.org/doi/pdf/10.1126/science.1222360. URL: https://www.science.org/doi/abs/10.1126/science.1222360.

[15] Hao Zhang et al. "Next steps of quantum transport in Majorana nanowire devices". In: *Nature Communications* 10.1 (Nov. 2019). ISSN: 2041-1723. DOI: 10.1038/s41467-019-13133-1. URL: http://dx.doi.org/10.1038/s41467-019-13133-1.

[16] Eduardo J. H. Lee et al. "Spin-resolved Andreev levels and parity crossings in hybrid superconductor–semiconductor nanostructures". In: *Nature Nanotechnology* 9.1 (Dec. 2013), pp. 79–84. ISSN: 1748-3395. DOI: 10.1038/nnano.2013.267. URL: http://dx.doi.org/10.1038/nnano.2013.267.

[17] J. Chen et al. "Ubiquitous Non-Majorana Zero-Bias Conductance Peaks in Nanowire Devices". In: *Physical Review Letters* 123.10 (Sept. 2019). ISSN: 1079-7114. DOI: 10.1103/physrevlett.123.107703. URL: http://dx.doi.org/10.1103/PhysRevLett.123.107703.

[18] Haining Pan and S. Das Sarma. "Physical mechanisms for zero-bias conductance peaks in Majorana nanowires". In: *Physical Review Research* 2.1 (Mar. 2020). ISSN: 2643-1564. DOI: 10.1103/physrevresearch.2.013377. URL: http://dx.doi.org/10.1103/PhysRevResearch.2.013377.

[19] Hao Zhang et al. "Large zero-bias peaks in InSb-Al hybrid semiconductor-superconductor nanowire devices". In: (2021). arXiv: 2101.11456 [cond-mat.mes-hall].

[20] Martin Leijnse and Karsten Flensberg. "Parity qubits and poor man's Majorana bound states in double quantum dots". In: *Physical Review B* 86.13 (Oct. 23, 2012), p. 134528. ISSN: 1098-0121, 1550-235X. DOI: 10.1103/PhysRevB.86.134528. arXiv: 1207.4299[cond-mat,physics:quant-ph]. URL: http://arxiv.org/abs/1207.4299.

[21] Jay D. Sau and S. Das Sarma. "Realizing a robust practical Majorana chain in a quantum-dot-superconductor linear array". In: *Nature Communications* 3.1 (July 17, 2012), p. 964. ISSN: 2041-1723. DOI: 10.1038/ncomms1966. URL: https://www.nature.com/articles/ncomms1966.

[22] Haining Pan and S. Das Sarma. "Disorder effects on Majorana zero modes: Kitaev chain versus semiconductor nanowire". In: *Physical Review B* 103.22 (June 2021). ISSN: 2469-9969. DOI: 10.1103/physrevb.103.224505. URL: http://dx.doi.org/10.1103/PhysRevB.103.224505.

[23] Alberto Bordin et al. "Tunable Crossed Andreev Reflection and Elastic Cotunneling in Hybrid Nanowires". In: *Physical Review X* 13.3 (Sept. 15, 2023), p. 031031. ISSN: 2160-3308. DOI: 10.1103/PhysRevX.13.031031. URL: https://link.aps.org/doi/10.1103/PhysRevX.13.031031 (visited on 04/16/2024).

[24] Guanzhong Wang et al. "Singlet and triplet Cooper pair splitting in hybrid superconducting nanowires". In: *Nature* 612.7940 (Dec. 15, 2022), pp. 448–453. ISSN: 0028-0836, 1476-4687. DOI: 10.1038/s41586-022-05352-2. URL: https://www.nature.com/articles/s41586-022-05352-2 (visited on 04/23/2024).

[25] Qingzhen Wang et al. "Triplet correlations in Cooper pair splitters realized in a two-dimensional electron gas". In: *Nature Communications* 14.1 (Aug. 12, 2023), p. 4876. ISSN: 2041-1723. DOI: 10.1038/s41467-023-40551-z. URL: https://www.nature.com/articles/s41467-023-40551-z (visited on 10/23/2023).

[26] Tom Dvir et al. "Realization of a minimal Kitaev chain in coupled quantum dots". In: *Nature* 614.7948 (Feb. 16, 2023), pp. 445–450. ISSN: 0028-0836, 1476-4687. DOI: 10.1038/s41586-022-05585-1. URL: https://www.nature.com/articles/s41586-022-05585-1.

[27] Sebastiaan L. D. ten Haaf et al. *Engineering Majorana bound states in coupled quantum dots in a two-dimensional electron gas*. Nov. 7, 2023. arXiv: 2311.03208[cond-mat]. URL: http://arxiv.org/abs/2311.03208 (visited on 12/04/2023).

[28] Ettore Majorana. "Teoria simmetrica dell'elettrone e del positrone". In: *Il Nuovo Cimento (1924-1942)* 14 (1937), pp. 171–184. URL: https://api.semanticscholar.org/CorpusID:18973190.

[29] Steven R. Elliott and Marcel Franz. "Colloquium: Majorana fermions in nuclear, particle, and solid-state physics". In: *Rev. Mod. Phys.* 87 (1 Feb. 2015), pp. 137–163. DOI: 10.1103/RevModPhys.87.137. URL: https://link.aps.org/doi/10.1103/RevModPhys.87.137.

[30] Guanzhong Wang. "Quantum Dots Coupled to Superconductors". PhD thesis. 2023.

[31] F. Zatelli. "Effects of spin-orbit interaction on elastic co-tunneling and crossed Andreev reflection". MA thesis. Delft, Netherlands: TU Delft, 2022.

[32] S.L.D. ten Haaf. "Delocalized Andreev bound states in coupled quantum dots". MA thesis. Leiden, Netherlands: Leiden University.

[33] Steven G Louie and Marvin L Cohen. "Fundamentals of Condensed Matter Physics". In: ().

[34] L P Kouwenhoven, D G Austing, and S Tarucha. "Few-electron quantum dots". In: *Reports on Progress in Physics* 64.6 (June 1, 2001), pp. 701–736. ISSN: 0034-4885, 1361-6633. DOI: 10.1088/0034-4885/64/6/201. URL: https://iopscience.iop.org/article/10.1088/0034-4885/64/6/201 (visited on 11/27/2023).

[35] R. Hanson et al. "Spins in few-electron quantum dots". In: *Reviews of Modern Physics* 79.4 (Oct. 1, 2007), pp. 1217–1265. ISSN: 0034-6861, 1539-0756. DOI: 10.1103/RevModPhys.79.1217. arXiv: cond-mat/0610433. URL: http://arxiv.org/abs/cond-mat/0610433 (visited on 11/27/2023).

[36] S. Roelofs. "Flux Tunable Elastic Cotunnelling and Crossed Andreev reflection". MA thesis. Delft, Netherlands: TU Delft, 2023.

[37] Joseph Thijssen and H. Zant. "Charge Transport and Single-Electron Effects in Nanoscale Systems". In: *physica status solidi (b)* 245 (Aug. 2008), pp. 1455–1470. DOI: 10.1002/pssb.200743470.

[38] B. Roovers. "Charge sensing Andreev bound states in semiconductor-superconductor hybrid structures". MA thesis. Delft, Netherlands: TU Delft, 2023.

[39] Florian Bennebroek Evertsz. "Supercurrent modulation by Andreev bound states in a quantum dot Josephson junction". MA thesis.

[40] Michael Tinkham. *Introduction to Superconductivity*. 1975. URL: https://api.semanticscholar.org/CorpusID:120168412.

[41] J. A. Sauls. "Andreev bound states and their signatures". In: *Philosophical Transactions of the Royal Society A: Mathematical, Physical and Engineering Sciences* 376.2125 (2018), p. 20180140. DOI: 10.1098/rsta.2018.0140. eprint: https://royalsocietypublishing.org/doi/pdf/10.1098/rsta.2018.0140. URL: https://royalsocietypublishing.org/doi/abs/10.1098/rsta.2018.0140.

[42] S. Guéron et al. "Superconducting Proximity Effect Probed on a Mesoscopic Length Scale". In: *Phys. Rev. Lett.* 77 (14 Sept. 1996), pp. 3025–3028. DOI: 10.1103/PhysRevLett.77.3025. URL: https://link.aps.org/doi/10.1103/PhysRevLett.77.3025.

[43] T. M. Klapwijk. "Proximity Effect From an Andreev Perspective". In: *Journal of Superconductivity* 17.5 (Oct. 2004), pp. 593–611. ISSN: 0896-1107, 1572-9605. DOI: 10.1007/s10948-004-0773-0. URL: http://link.springer.com/10.1007/s10948-004-0773-0 (visited on 04/19/2024).

[44] Nick Van Loo et al. "Electrostatic control of the proximity effect in the bulk of semiconductor-superconductor hybrids". In: *Nature Communications* 14.1 (June 7, 2023), p. 3325. ISSN: 2041-1723. DOI: 10.1038/s41467-023-39044-w. URL: https://www.nature.com/articles/s41467-023-39044-w.

[45] Aleksandr F. Andreev. "THERMAL CONDUCTIVITY OF THE INTERMEDIATE STATE OF SUPERCONDUCTORS. PART II". In: (1964). URL: https://api.semanticscholar.org/CorpusID:116976966.

[46] Jaap Joachim Wesdorp. "Spinful Andreev States in Superconducting Circuits". PhD thesis. 2024.

[47] Landry Bretheau. "Localized Excitations in Superconducting Atomic Contacts: Probing the Andreev Doublet". PhD thesis. 2013.

[48] Juan Daniel Torres Luna et al. *Flux-tunable Kitaev chain in a quantum dot array*. Feb. 12, 2024. arXiv: 2402.07575[cond-mat]. URL: http://arxiv.org/abs/2402.07575 (visited on 03/19/2024).

[49] Chun-Xiao Liu et al. *Enhancing the excitation gap of a quantum-dot-based Kitaev chain*. Oct. 13, 2023. arXiv: 2310.09106[cond-mat]. URL: http://arxiv.org/abs/2310.09106.

[50] Francesco Zatelli et al. *Robust poor man's Majorana zero modes using Yu-Shiba-Rusinov states*. Nov. 6, 2023. arXiv: 2311.03193[cond-mat,physics:quant-ph]. URL: http://arxiv.org/abs/2311.03193.

[51] Chun-Xiao Liu et al. "Tunable superconducting coupling of quantum dots via Andreev bound states in semiconductor-superconductor nanowires". In: *Physical Review Letters* 129.26 (Dec. 20, 2022), p. 267701. ISSN: 0031-9007, 1079-7114. DOI: 10.1103/PhysRevLett.129.267701. arXiv: 2203.00107[cond-mat]. URL: http://arxiv.org/abs/2203.00107 (visited on 10/23/2023).

[52] Esteban A. Martinez et al. *Measurement circuit effects in three-terminal electrical transport measurements*. Apr. 6, 2021. arXiv: 2104.02671[cond-mat]. URL: http://arxiv.org/abs/2104.02671 (visited on 10/23/2023).

[53] Jeroen Danon et al. "Nonlocal conductance spectroscopy of Andreev bound states: Symmetry relations and BCS charges". In: *Physical Review Letters* 124.3 (Jan. 22, 2020), p. 036801. ISSN: 0031-9007, 1079-7114. DOI: 10.1103/PhysRevLett.124.036801. arXiv: 1905.05438[cond-mat]. URL: http://arxiv.org/abs/1905.05438 (visited on 03/31/2024).

[54] David van Driel et al. *Charge sensing the parity of an Andreev molecule*. Nov. 3, 2023. arXiv: 2311.02001[cond-mat]. URL: http://arxiv.org/abs/2311.02001.

[55] Florian Vigneau et al. "Probing quantum devices with radio-frequency reflectometry". In: *Applied Physics Reviews* 10.2 (June 1, 2023), p. 021305. ISSN: 1931-9401. DOI: 10.1063/5.0088229. URL: https://pubs.aip.org/apr/article/10/2/021305/2885320/Probing-quantum-devices-with-radio-frequency.

[56] Alberto Bordin et al. *Signatures of Majorana protection in a three-site Kitaev chain*. Feb. 29, 2024. arXiv: 2402.19382[cond-mat]. URL: http://arxiv.org/abs/2402.19382 (visited on 03/12/2024).

[57] Christian M. Moehle et al. "Controlling Andreev Bound States with the Magnetic Vector Potential". In: *Nano Letters* 22.21 (Nov. 9, 2022), pp. 8601–8607. ISSN: 1530-6984, 1530-6992. DOI: 10.1021/acs.nanolett.2c03130. URL: https://pubs.acs.org/doi/10.1021/acs.nanolett.2c03130.

[58] Christian G. Prosko et al. *Flux-Tunable Hybridization in a Double Quantum Dot Interferometer*. May 18, 2023. arXiv: 2303.04144[cond-mat,physics:quant-ph]. URL: http://arxiv.org/abs/2303.04144 (visited on 03/19/2024).

[59] David Van Driel et al. "Spin-filtered measurements of Andreev bound states in semiconductor-superconductor nanowire devices". In: *Nature Communications* 14.1 (Oct. 28, 2023), p. 6880. ISSN: 2041-1723. DOI: 10.1038/s41467-023-42026-7. URL: https://www.nature.com/articles/s41467-023-42026-7 (visited on 12/18/2023).

[60] Christian Mario Möhle. "Induced superconductivity in antimony-based two-dimensional electron gases". PhD thesis. Delft, Netherlands: TU Delft, 2023.

[61] Athanasios Tsintzis, Ruben Seoane Souto, and Martin Leijnse. "Supplemental Information to "Creating and detecting poor mans Majorana bound states in interacting quantum dots"". In: ().

[62] Martin Leijnse and Karsten Flensberg. "Coupling Spin Qubits via Superconductors". In: *Phys. Rev. Lett.* 111 (6 Aug. 2013), p. 060501. DOI: 10.1103/PhysRevLett.111.060501. URL: https://link.aps.org/doi/10.1103/PhysRevLett.111.060501.

[63] Mátyás Kocsis et al. *Strong nonlocal tuning of the current-phase relation of a quantum dot based Andreev molecule*. 2024. arXiv: 2303.14842 [cond-mat.mes-hall].

[64] Jonas Schuff et al. *Fully autonomous tuning of a spin qubit*. 2024. arXiv: 2402.03931 [cond-mat.mes-hall].

[65] Rouven Koch et al. "Adversarial Hamiltonian learning of quantum dots in a minimal Kitaev chain". In: *Phys. Rev. Appl.* 20 (4 Oct. 2023), p. 044081. DOI: 10.1103/PhysRevApplied.20.044081. URL: https://link.aps.org/doi/10.1103/PhysRevApplied.20.044081.

[66] Yanli Liu, Yuan Gao, and Wotao Yin. *An Improved Analysis of Stochastic Gradient Descent with Momentum*. 2020. arXiv: 2007.07989 [math.OC].